



# Selective Excitation MR Imaging with Parallel Transmission (pTx)

DISSERTATION

Zur Erlangung des akademischen Grades  
Doktoringenieur (Dr.-Ing.)

vorgelegt der Fakultät für Informatik und Automatisierung  
der Technischen Universität Ilmenau

von M.Sc. Rainer Schneider  
geboren am 01. März 1986 in Hermannstadt

Tag der Einreichung: 24. September 2014  
Tag der wissenschaftlichen Aussprache: 07. Januar 2015

Gutachter: 1. Prof. Dr.-Ing. habil. Jens Haueisen  
2. Prof. Dr. rer. nat. med. habil. Jürgen R. Reichenbach  
3. Dr. rer. nat. Josef Pfeuffer

urn:nbn:de:gbv:ilm1-2015000033



---

## Abstract

The focus of this thesis is on the development of radio-frequency (RF) pulses for dedicated applications in magnetic resonance imaging (MRI) utilizing the parallel transmission (pTx) technology. The contributions include their algorithmic design and implementation as well as simulations and human in-vivo experiments on a commercially available clinical pTx MRI scanner platform at 3 T.

The role of RF pulses in MRI is essential for both the signal generation and suppression of undesired signal sources. Basically, an RF pulse excites nuclear spins within a subject that are measured by resonant coils and subsequently reconstructed into images. Besides the need for accuracy, the RF pulses require to be as short and as energy efficient as possible due to main field inhomogeneity, spin relaxation and patient tissue heating limitations. Recently, the introduction of the pTx technology facilitated new spatial degrees of freedom to satisfy these requirements. Many studies based on custom-built pTx platforms have proven great benefits, but also showed potential pitfalls coming along with the increased degrees of freedom. The robust design and transfer of pTx RF pulses to a clinical setup and applications is still on-going research and topic of this thesis.

The contributed work can be divided into three application fields. First, the performance of 2-D spatially selective RF pulses (2DRFs) is improved for inner-volume imaging. Here, RF excitation is limited to a region of interest (ROI) to allow for less distorted images with higher resolution. New k-space trajectory designs are proposed for 2DRF pulses, which show up to 43% better accuracy with 79% improved RF power efficiency or substantially shortened pulse durations by more than a factor of two. Resulting diffusion weighted images show an signal-to-noise ratio (SNR) increase up to 40% compared to conventional designs.

Then, the additional RF transmit channel is used to pre-compensate signal losses induced by patient-specific main field perturbations in gradient recalled echo (GRE) images. A fast, robust and fully automatized method is proposed to reduce these signal voids on a slice-to-slice basis. Tailored RF pulses are designed using the measured main field inhomogeneity and RF transmit coil sensitivity profiles. Signal dropouts in multi-slice images can be recovered on average by 47%.

Finally, an inherent RF power efficient 2-D spiral trajectory design is employed to realize anatomically shaped saturation pulses. The pulses aim to accurately suppress undesired signal sources, like moving inner organs, to avoid motion artifacts. The proposed 2DRF spiral design proves to show the optimal balance of RF power efficiency and spatial fidelity in various anatomical locations and clearly outperforms other common design strategies. The approach is further extended to multiple frequencies, so that the shaped pulses can also selectively saturate other tissue types such as fat.





---

## Zusammenfassung

Der Schwerpunkt dieser Dissertation liegt in der Entwicklung von Hochfrequenz (HF)-Pulsen für dedizierte Anwendungen in der Magnetresonanztomographie (MRT) unter Verwendung der parallelen Sendetechnik (pTx). Die wissenschaftlichen Beiträge dieser Arbeit umfassen dabei den Entwurf und die Implementierung neuer Algorithmen, welche mit Hilfe von Simulationen und in-vivo Human-Experimenten auf einer kommerziell verfügbaren 3 T pTx MRT Scanner-Plattform validiert wurden.

In der MRT sind HF-Pulse essentiell für die Signalgenerierung als auch für die Unterdrückung von unerwünschten Signalquellen. Bei ihrer Anwendung werden Atomkerne im untersuchten Probanden angeregt, welche daraufhin ein messbares Signal abgeben. Das hochfrequente Messsignal wird von Empfangsspulen erfasst und schließlich in Bilder rekonstruiert. Aufgrund von limitierenden physikalischen Effekten wie Magnetfeld-Inhomogenitäten, Kernspin-Relaxationsprozessen und der auftretenden Erwärmung von Patientengewebe, müssen die HF-Pulse idealerweise so genau, so kurz und so energieeffizient wie möglich sein. Die pTx-Technologie versucht diesen Anforderungen durch die Bereitstellung von neuen räumlichen Freiheitsgraden entgegenzutreten. Viele Studien wurden auf Basis von einzel-angefertigten pTx-Plattformen durchgeführt und haben die vielen Vorteile und Möglichkeiten, aber auch potentielle Gefahren der vermehrten Freiheitsgrade aufgezeigt. Das robuste Design und die Überführung von pTx HF-Pulsen in das klinische Umfeld sind stets Gegenstand der aktuellen Forschung und Ziel dieser Arbeit.

Die entstandenen wissenschaftlichen Beiträge können zu drei verschiedenen Applikationsfeldern zugeordnet werden. Zuerst wird die Performanz von 2-D räumlich-selektiven HF-Pulsen (2DHF) für die Inner-Volume-Bildgebung verbessert. Hier wird die HF-Anregung auf einen bestimmten Bildbereich (ROI) eingeschränkt, um Bilder mit verringerten geometrischen Verzerrungen und höherer Auflösung zu ermöglichen. Neue k-Raum Trajektorien-Designs werden für 2DHF-Pulse vorgeschlagen, welche um 43% genauer und gleichzeitig um 79% energieeffizienter sind oder deutlich verkürzte Pulszeiten um Faktor größer zwei aufzeigen. Die darauf basierenden diffusions-gewichteten Bilder zeigen einen bis zu 40% Signal-zu-Rausch (SNR)-Gewinn gegenüber zu konventionellen Designs.

In zweiten Anwendungsfeld wird der zusätzliche HF-Anregungskanal zur Kompensation von Signalverlusten in Gradienten-Echo (GRE)-Bildern verwendet. Die Signalverluste werden dabei durch patienten-spezifische Magnetfeld-Verzeichnungen ausgelöst. Ein schnelles, robustes und voll automatisiertes Verfahren wird vorgeschlagen, um diesen Signalverlusten schicht-spezifisch entgegenzuwirken. Maßgeschneiderte HF-Pulse werden unter Einbezug der gemessenen Hauptmagnetfeld-Inhomogenitäten und HF-Sendespulensensitivitätsprofilen

berechnet. Im Durchschnitt können 47% der Signalausfälle in Multi-Schicht-Aufnahmen wiederhergestellt werden.

Schließlich wird ein 2-D Spiral-Trajektorien-Design für die Verwirklichung von anatomisch geformten Sättigungspulsen ausgearbeitet, welches eine inhärente Energieeffizienz bietet. Die Pulse streben eine möglichst genaue Unterdrückung von unerwünschten Signalquellen, wie z.B. sich bewegenden inneren Organen an, um damit Bewegungsartefakte in den resultierenden Bildern auszuschließen. Das vorgeschlagene 2DHF-Spiral-Design zeigt in verschiedenen anatomischen Regionen eine optimale Ausgewogenheit zwischen HF-Energieeffizienz und räumlicher Abbildungsgüte und übertrifft andere bekannte Ansätze. Das Verfahren wurde hinsichtlich mehrerer Anregungs-Frequenzen erweitert. Damit können die räumlich geformten Pulse auch andere Gewebetypen wie Fett selektiv unterdrücken.

---

## Acknowledgements

I would like to express my deepest gratitude and appreciation to all individuals who made this work possible.

First, I would like to thank my advisors Prof. Jens Haueisen and Dr. Josef Pfeuffer. I was blessed to have Josef as my mentor, who has been instrumental to this thesis. I am very grateful for his support, inspiration and guidance on MRI research, but also on my general work attitude. I would be happy to work with him again in future projects. I am fortunate about Prof. Jens Haueisen being my advisor throughout all my scientific endeavors since my Bachelor's degree. I admire his continuous support, valuable comments and expertise in so many research domains. In addition, I would like to thank them both for proofreading my manuscripts including this thesis.

I also thank Prof. Jürgen Reichenbach for his valuable time and insightful comments on my dissertation.

It has been a real pleasure interacting and working with all colleagues at Siemens. In particular, I am sincerely grateful to Dr. Heiko Meyer for his endless support of my work and career. I thank my colleague and friend Dr. Thomas Beck for answering my annoying questions, his general advice and the great time in the lab, but also for some exciting “eye-catching” moments after hours. I would also like to thank Dr. Dieter Ritter for our fruitful discussions on RF pulse design and beyond the scope of MRI. I am thankful to all my other colleagues of the Neuro application development team: Stefan Huwer, Martin Harder, Dr. Thorsten Feiweier and Dr. Bjoern Jakoby - you guys have been great! I also appreciate the tremendous help given by Dr. Michael Koehler and Matthias Gebhardt from the MR physics department.

It has been a privilege visiting NYU Langone Medical Center, New York City, during my PhD project. I thank Prof. Fernando Boada, Dr. Christian Geppert, Dr. Christopher Gliemli and the rest of the NYU lab for the great time and experience.

Finally, and most importantly, I would like to thank: my parents, Kurt and Maria, and my brother Arnold for their unconditional love and support. My wonderful girlfriend Sabine, who encouraged and loved me throughout all these years in happy and stressful times - I owe her so much. Without all of you none of this would have been possible.

*Rainer Schneider  
Erlangen, Germany  
September 2014*



---

## Nomenclature

### List of Abbreviations

2DRF	2-D spatially selective RF pulse
AAM	additive angle method
AF	asymmetry factor
BOLD	blood oxygenation level dependent
CGLS	conjugate gradient least-squares
CLS	complex least-squares
CP	circular polarized
CT	computed tomography
DoF	degrees of freedom
ED	equal-density
EP	echo-planar
EP-2DRF	2-D spatially selective RF pulses based on a echo-planar trajectory
EPI	echo-planar imaging
FA	flip angle
FLASH	fast low angle shot
fMRI	functional MRI
FOE	field of excitation
FOV	field of view
FT	Fourier transform
GRE	gradient recalled echo
HRF	hemodynamic response function
LCLTA	linear class of large tip-angle

LSQR	least-squares QR decomposition
MF-2DRF	multi-frequency 2-D spatially selective RF pulse
MLS	magnitude least-squares
MRI	magnetic resonance imaging
NMR	nuclear magnetic resonance
PET	positron emission tomography
PTA	perturbation analysis
pTx	parallel transmission
RF	radio-frequency
rFOV	reduced field of view
RMSE	root mean square error
ROI	region of interest
SAR	specific absorption rate
SE	spin-echo
SENSE	sensitivity encoding
SNR	signal-to-noise ratio
SPINS	spiral non-selective
SSD	sum of squared differences
STA	small tip-angle approximation
STD	standard deviation
SVD	singular value decomposition
SWI	susceptibility weighted imaging
TD	target pattern driven
TE	echo time
TR	repetition time
TSE	turbo spin-echo
TX	transmit
VD	variable-density
VERSE	variable-rate selective excitation
VOP	virtual observer point

## Mathematical Notation

$A, a$	scalar
$\mathbf{a}$	vector
$\mathbf{A}$	matrix
$\hat{x}$	estimate of $x$
$\bar{x}$	overall mean value of $x$
$\text{real}(x)$	real value of $x$
$\text{imag}(x)$	imaginary value of $x$
$\text{diag}\{x\}$	matrix with diagonal elements $x$
$ \cdot $	absolute value
$[\dots]^T$	transposed
$\ \cdot\ _p$	$p$ -norm of matrix or vector
$\ \cdot\ $	euclidean-norm ( $p = 2$ ) of matrix or vector
$\lfloor \cdot \rfloor$	floor
$\lceil \cdot \rceil$	ceil
$\times$	product of scalars, cross product/vector product
$\otimes$	convolution
$a \bmod n$	$a$ modulo $n$





---

## Contents

<b>Nomenclature</b> .....	vii
List of Abbreviations .....	vii
Mathematical Notation .....	ix
<b>List of Figures</b> .....	xiv
<b>List of Tables</b> .....	xv
<b>1 Motivation</b> .....	1
1.1 Introduction .....	1
1.2 Aims of the Thesis .....	2
1.3 Structure of the Thesis .....	3
<b>2 Background</b> .....	5
2.1 Magnetic Resonance Imaging .....	5
2.2 RF Pulse Design .....	7
2.2.1 Bloch Equation .....	7
2.2.2 Single-Channel Transmission .....	8
Small Tip-Angle Approximation .....	8
Non-Iterative Fourier Approach .....	9
Iterative Optimization Approach .....	10
2.2.3 Parallel Transmission .....	11
Introduction .....	11
Spatial Domain Design Approach .....	11
Simultaneous Gradient and RF Optimization .....	13
SAR Optimization .....	14
Large Tip-Angle Design .....	14
TX k-Space Trajectories .....	15
Practical Framework and Considerations .....	17
2.3 Off-Resonance .....	20
2.3.1 Sources .....	20
2.3.2 Effects .....	23
<b>3 2DRF Pulse Design for Reduced FOV Imaging with pTx</b> .....	27
3.1 Enhanced Correction of Off-Resonance Effects in 2DRF-Pulse Design .....	27
3.1.1 Introduction .....	27

3.1.2	Theory . . . . .	29
3.1.3	Methods . . . . .	31
3.1.4	Results . . . . .	34
3.1.5	Discussion . . . . .	42
3.2	Asymmetric 2DRF-Pulse Design . . . . .	45
3.2.1	Introduction . . . . .	45
3.2.2	Methods . . . . .	45
3.2.3	Results . . . . .	47
3.2.4	Discussion . . . . .	47
4	<b>pTx z-Shim for Local Signal Recovery</b> . . . . .	49
4.1	Introduction . . . . .	49
4.2	Theory . . . . .	50
4.3	Methods . . . . .	54
4.4	Results . . . . .	55
4.5	Discussion . . . . .	61
5	<b>Shaped Saturation with pTx</b> . . . . .	67
5.1	Shaped Saturation with Inherent RF-Power-Efficient Trajectory Design . . . . .	67
5.1.1	Introduction . . . . .	67
5.1.2	Theory . . . . .	69
5.1.3	Methods . . . . .	72
5.1.4	Results . . . . .	76
5.1.5	Discussion . . . . .	81
5.2	Shaped Fat-Saturation with Multi-Frequency Design . . . . .	85
5.2.1	Introduction . . . . .	85
5.2.2	Methods . . . . .	86
5.2.3	Results . . . . .	86
5.2.4	Discussion . . . . .	87
6	<b>Summary and Outlook</b> . . . . .	89
	<b>References</b> . . . . .	93

---

## List of Figures

1.1	MR market of clinical 1.5 T and 3 T systems .....	3
2.1	Principles of spatial encoding in MRI .....	7
2.2	Illustration of TX SENSE .....	12
2.3	Selection of TX k-space trajectories .....	16
2.4	Overview of pTx RF pulse design framework .....	17
2.5	Computation complexity of pTx RF pulse design .....	20
2.6	Off-resonance effects in TSE, GRE and EPI .....	24
2.7	Off-resonance effects in RF excitation .....	25
3.1	Schematic of $B_0$ driven variable density trajectory design .....	32
3.2	Target pattern adapted to physical properties of k-space trajectory .....	35
3.3	Overview of $B_0/B_1$ maps and EP-2DRF k-space trajectory .....	36
3.4	Comparison of EP-2DRF k-space density functions and positions .....	36
3.5	Detailed analysis of VD sampling scheme .....	38
3.6	Performance analysis of EP-2DRF designs at different off-resonance levels ...	39
3.7	Detailed Bloch simulations of EP-2DRF designs at different off-resonance levels	40
3.8	Performance analysis of EP-2DRF designs at different TX acceleration levels.	41
3.9	Human in-vivo experiments of EP-2DRF designs .....	42
3.10	Exemplary illustration of asymmetric EP-2DRF design .....	46
3.11	Analysis of EP-2DRF pulse profiles at different asymmetry factors .....	47
3.12	Human in-vivo rFOV diffusion experiments with asymmetric EP-2DRF design	48
4.1	Schematic of automatic time delay determination .....	53
4.2	Image artifacts with time-delayed excitation .....	56
4.3	Multi-slice FLASH experiments with pTx z-shim .....	57
4.4	Detailed computation of time-delays in two FLASH images .....	59
4.5	Detailed image quality analysis of two FLASH images .....	60
4.6	BOLD fMRI breath-hold experiments with pTx z-shim .....	62
5.1	Schematic of TD 2-D spiral design .....	73
5.2	Anatomical positions and target patterns of simulations study .....	75
5.3	Overview of different 2-D spiral trajectory designs .....	77
5.4	Performance of different TD 2-D spiral trajectory designs .....	78
5.5	Performance of ED, VD and TD 2-D spiral trajectory designs .....	79

5.6	Detailed Bloch simulations of ED, VD and TD 2-D spiral trajectory based RF pulse designs .....	80
5.7	Effect of suboptimal weighting window width on TD RF pulse performance ..	81
5.8	Human in-vivo shaped saturation experiments in head, abdomen and spine ..	82
5.9	Phantom experiments with different fat saturation techniques .....	87
5.10	Human in-vivo experiments with different fat saturation techniques .....	88

---

## List of Tables

4.1	pTx z-shim performance analysis of multi-slice FLASH images . . . . .	61
4.2	pTx z-shim performance analysis in breath-hold fMRI BOLD experiment . . . .	63



## Motivation

### 1.1 Introduction

Magnetic resonance imaging (MRI) is an essential part of today's clinical routine and research. The non-invasive image modality is commonly known for its superior soft-tissue contrast in anatomical imaging. But it is also capable to visualize structure and to assess functional properties of the human body in high resolution. MRI is based on the effect of nuclear magnetic resonance (NMR) and can be principally divided into two iterating operative stages, i.e. the creation and the measurement of the NMR-signal. The first stage involves the application of a radio-frequency (RF) pulse to nuclei with a nuclear spin<sup>1</sup> placed in a strong static magnetic field and is denoted as the excitation phase. The second stage, i.e. the acquisition phase, deals with the collection and manipulation of the generated signal. Since there is no exposure to harmful ionizing radiation like in other medical imaging techniques as computed tomography (CT) or positron emission tomography (PET), MRI has been developed to a preferred method in diagnosis and in neurological research.

In the past years, a lot of efforts were made towards higher static magnetic fields strengths to improve the signal-to-noise ratio (SNR), image contrast and resolution. In research, ultra-high-field strengths are perpetually pushed to the technical limits and achieved 10.5 T and more for human applications [1]. In contrast, the clinical setting still concentrates on magnetic field strengths of 1.5 T, but showed a progressively rising interest in high-field MRI systems with 3 T over the last decade. This emerging clinical movement towards high-field is also reflected by the global MRI market development: The market share of 3 T systems showed a substantially increase during the past years, whereas MRI systems below 1.5 T became clearly less important (*Figure 1.1*). The market of conventional 1.5 T MRI still remains the biggest, but its development shows a relatively moderate growth.

There are reasons why there is only a reluctant commitment and clinical transition to 3 T MRI systems and advantages of high-field imaging. Besides the higher initial costs, there are some major problems rising with higher field strengths in MRI:

**Inhomogeneous excitation profiles:** Referring to the proton Larmor frequency, the RF wavelength<sup>2</sup> becomes comparable to imaged human body parts at  $\geq 3$  T. As a consequence

---

<sup>1</sup> Due to the abundance of water in living organism, the proton  $^1H$  is the major target for clinical MRI

<sup>2</sup> The RF wavelength is 28 cm at 3 T and 12 cm at 7 T

the transmitted RF field can interfere to constructive or destructive standing-wave effects and results in either regional contrast increase or loss across the image. At 3 T such areas of shading and losses of signal typically occur when imaging the abdomen or thighs.

**Specific absorption rate (SAR):** RF deposition in the patient generally leads to tissue heating and can lead to damage, if the local RF power is not properly controlled. The SAR metric has been established to approximate the degree of tissue heating by assessing the absorption of electro-magnetic waves in biological tissue. With increasing static magnetic field strength, the SAR scales quadratically due to the higher Larmor frequency and RF power that is required to excite spins. In other words, the SAR is approximately quadrupled going from 1.5 T to 3 T. Therefore, the SAR deposition must be well regulated by the adjustment of imaging speed to prevent from severe patient heating at higher field strengths. Regulatory limits have been established to define the adequate level of patient heating, which can substantially elongate the total image acquisition time.

**Off-resonance related artifacts:** MRI relies on the fact that water nuclei have a distinct Larmor frequency in a constant static magnetic field. In practice, so-called off-resonance effects violate this assumption. Off-resonance effects denote all signals from atomic nuclei, which have a different precessing frequency from the expected Larmor frequency within an ideal system. Reasons for the deviation of the resonance frequency are manifold and include amongst others technical imperfections of the magnetic field, chemical shift and magnetic susceptibility variation. Especially the latter two can substantially compromise the image quality in terms of geometric distortions and prominent signal loss. The magnitude of both chemical shift and susceptibility artifacts is patient-specific and linearly scales with the main field strength. Thus, off-resonance induced artifacts are more of a concern at 3 T and beyond.

Parallel transmission (pTx) has been shown to be one of the most promising solutions to mitigate the aforementioned shortcomings of (ultra-)high-field MRI [2–14]. The pTx technology comprises the utilization of multiple (localized) independent RF transmit (TX) coils with spatially encoded RF deposition and was originally proposed by *Katscher et al.* [2] and *Zhu* [3]. The newly available spatial degrees of freedom enable optimized RF pulses, which can directly reduce SAR and inhomogeneous excitation as both relate to the excitation phase of MRI. Off-resonance related artifacts can be also tackled by the application of custom-designed RF pulses, which became suitable with pTx: The excitation of nuclei can be specified to a region of interest (ROI) with multi-dimensional spatially selective RF pulses to limit the off-resonance artifact impact. Alternatively, tailored RF pulses can be designed to pre-compensate off-resonance related effects occurring during the acquisition phase. However, to date the majority of the research done in this field is based on custom-built hardware and often conducted on ultra-high-field systems, which differ substantially from clinical systems and clinical routine.

## 1.2 Aims of the Thesis

This thesis focuses on the development of pTx RF pulse design methods based on a clinical setting. In particular, all in-vivo studies are conducted on clinical and commercially available 3 T scanner systems. In contrast to the majority of the research sites equipped with local eight channel RF TX arrays [4, 5, 12, 14–18], all commercially available MRI scanners with pTx functionality consist only of two whole-body RF TX channels [19–21], i.e. less degrees of



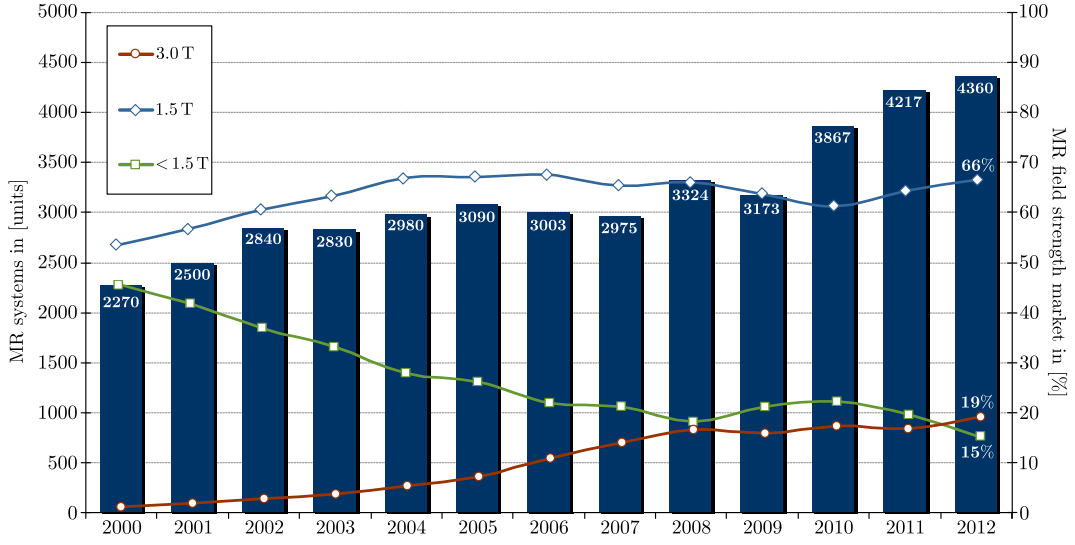


**Fig. 1.1:** MRI scanner market development in OECD<sup>3</sup> states. Statistics are taken from [22].

freedom for optimization. Besides, the clinical setting demands further conceptual qualities: Safety regulations require a SAR-controlled RF pulse design, which becomes complicated with multiple RF channels due to spatially varying electric field components. Hardware limitations have to be considered to not damage the MRI scanner system. Finally, clinical routine asks for adequate computation speed, so that the numerical complexity of the algorithms has to be kept to a minimum. At present, most of the proposed pTx related methods still struggle to find their way into clinical practice due to not completely satisfying stated requirements.

The main objective of the thesis is the efficient and robust design of multi-dimensional spatially selective and tailored RF pulses fulfilling all criteria mentioned above. The developed algorithms of this thesis aim to be explicitly compatible and suited for clinical routine applications amongst others for the correction of off-resonance related artifacts.

### 1.3 Structure of the Thesis

In the following chapter, the fundamentals of MRI and current RF pulse design approaches for pTx are briefly introduced (*Chapter 2*). This chapter also includes a brief description of off-resonance artifacts and their sources being present in clinical high-field MRI. The subsequent *Chapter 3* introduces strategies for the improvement of a specific two-dimensional spatially selective RF excitation pulse type [23–27], which is already widely used in echo-planar imaging techniques. The proposed approaches cover the shortening of the RF pulse duration and the increased robustness regarding off-resonance effects to enhance significantly both, the excitation and image quality. In *Chapter 4*, a fully automated method is presented to correct for off-resonance induced signal loss in commonly used gradient-echo based imaging sequences [28, 29]. The method takes advantage of the two available RF transmitters to pre-compensate signal de-phasing effects during the acquisition phase. Ultimately, an RF

<sup>3</sup> Organisation for Economic Co-operation and Development.

power efficient RF pulse design is proposed in *Chapter 5*, which enables the reliable design of anatomically shaped RF saturation pulses [30–33]. Those pulses can help to suppress locally undesired signal sources that potentially interfere with the ROI, e.g. the accurate suppression of moving inner organs in lumbar spine imaging. Finally, *Chapter 6* summarizes the novel scientific contributions of this thesis and provides recommendations for future developments.

## Background

### 2.1 Magnetic Resonance Imaging

This section provides a brief and fundamental background of MRI. In the following, MRI basics are motivated from the technical point of view, i.e. how the physical phenomenon of nuclear magnetic resonance (NMR) is practically utilized to generate an MR image. The interested reader may refer to [34–38] for a more profound theory on NMR to MRI.

The MRI scanner can be regarded as a technical instrumentation of the Fourier transform (FT). The measured signal of an MR image corresponds to its 2D/3D Fourier transform and is acquired in the frequency domain. In MRI physics, the frequency domain, where complex values are sampled during an MR experiment is also denoted as *k-space*. The source of the detected signal is based on nuclei that possess a nuclear spin angular momentum that is further associated with a magnetic moment. This spin behavior is disclosed by all atoms with an odd number of protons or neutrons. Within organic tissues, it can be mostly found in relation with hydrogen nuclei ( $^1H$ ) in the form of water ( $H_2O$ ). The MR experiment intends to generate and acquire the signals from those nuclei in *k-space*. In this process, a Fourier encoding scheme further helps to spatially assign the signal from the nuclear conglomeration of hydrogen. In current MR scanner systems, three magnetic field components have been employed to technically realize this two-stage MR image generation:

- **Static magnetic field  $B_0$ :** The magnetic moments of the hydrogen nuclei within in the human body are randomly oriented if no external magnetic field is applied. In presence of a strong static magnetic field  $B_0$ , the magnetic moments of the hydrogen nuclei align anti-parallel or parallel along the axis of  $B_0$ . The two different states of alignment correspond to the discrete energy eigenstates of the protons, i.e. the lower energy state  $E_{m=-1/2}$  (co-aligned with the magnetic field) and the higher energy state  $E_{m=+1/2}$  (anti-aligned state). A transition between those states is possible by interaction with a photon of energy  $\gamma B_0 \hbar$  or rather of frequency:

$$\omega = \frac{E_{m=-1/2} - E_{m=+1/2}}{\hbar} = \gamma B_0, \quad (2.1)$$

where  $\hbar$  is Planck's constant divided by  $2\pi$  and  $\gamma$  the gyromagnetic ratio for protons ( $\gamma/2\pi = 42.576$  MHz/T). The frequency  $\omega$  is commonly referred as the proton Larmor frequency.

In the thermal equilibrium of in-vivo human tissue, the distribution of spins according to the two energy states follows the Boltzmann statistics: At  $B_0 = 3\text{ T}$  and a temperature of  $310\text{ K}$  only 20 ppm more spins occupy the lower energy state being aligned with the orientation of  $B_0$ . Despite of this small yield of co-aligned spins, the huge number of nuclei participating in a MR experiment result in a measurable macroscopic net magnetization  $M_0$ . The net magnetization  $M_0$  increases linearly with the static magnetic field strength and can be approximately transferred to a linear gain in SNR [39].

In MRI, the constant magnetic field  $B_0$  is always present and is generally oriented in the positive z-direction from the feet to the head.

- **Radio-frequency field  $B_1$ :** In the excitation phase, the equilibrium state can be perturbed by the application of an RF magnetic pulse  $B_1$  using a single or multiple RF TX coils. The RF pulse field is oriented perpendicular to  $B_0$ , i.e. in the transverse x-y plane, and is tuned to the resonance frequency  $\omega$ . The additional transverse field creates a torque rotating the magnetic moments away from the co-aligned minimum energy state. Precisely, the main orientation of the magnetization is effectively tilted from longitudinal towards the transverse plane inducing a spin precession at Larmor frequency. The complete magnetization dynamics depending on the overall and time-varying external magnetic field vector is described by the Bloch equation and is discussed more thoroughly in *Section 2.2*. When the  $B_1$  field is switched off at the end of the excitation phase, the magnetization continues to precess with  $\omega$  until it realigns with the direction of  $B_0$ . During this time, i.e. the acquisition phase, solely the transverse component of the precessing magnetization vector can be measured with RF receiver coils. According to Faraday's law of induction an electromotive force is induced in the RF coils due to the time-varying magnetic field of the magnetization vector, which finally contributes to the detected MR signal.
- **Gradient fields  $G$ :** The gradient field is essential for the spatial encoding in the MRI experiment. It is made up by three independent z-oriented magnetic field components, which impose a linearly varying magnetic field strength along x, y and z-direction, respectively. Thus, the gradient field can be used to spatially alter the z-directed  $B_0$  field and to become the Larmor frequency as a function of space and time:

$$\omega(x, y, z, t) = \gamma(B_0 + G_x(t) \cdot x + G_y(t) \cdot y + G_z(t) \cdot z), \quad (2.2)$$

where  $G_x(t)$ ,  $G_y(t)$  and  $G_z(t)$  are the corresponding time-courses of the x-, y- and z-gradient fields. During the excitation phase, the gradient field is used to localize the effect of the RF field on the magnetic moments to a particular ROI: As the RF field is tuned to the central resonance frequency with a certain bandwidth, only the spatial subset of spins will be excited, whose Larmor frequency matches the RF frequency. On the other hand, the gradient fields are also used to distinguish between signals originating from different spatial locations. Given that the excited spins continue precessing after excitation, the gradient fields can be applied to disperse the precessing frequencies for a spatially assigned detection of the signals. This is typically done in Fourier based encoding techniques, i.e. the excited magnetic moments are transferred into different frequency and phase states to resolve the 2D/3D k-space. A simplified 1D illustration of selective excitation and signal acquisition can be found in *Figure 2.1*. In both phases of the MRI experiment, the gradient field effectively encodes the path through k-space, where the signal is either generated (excitation) or measured (acquisition). For the exact relationship during excitation, please refer to the subsequent section.

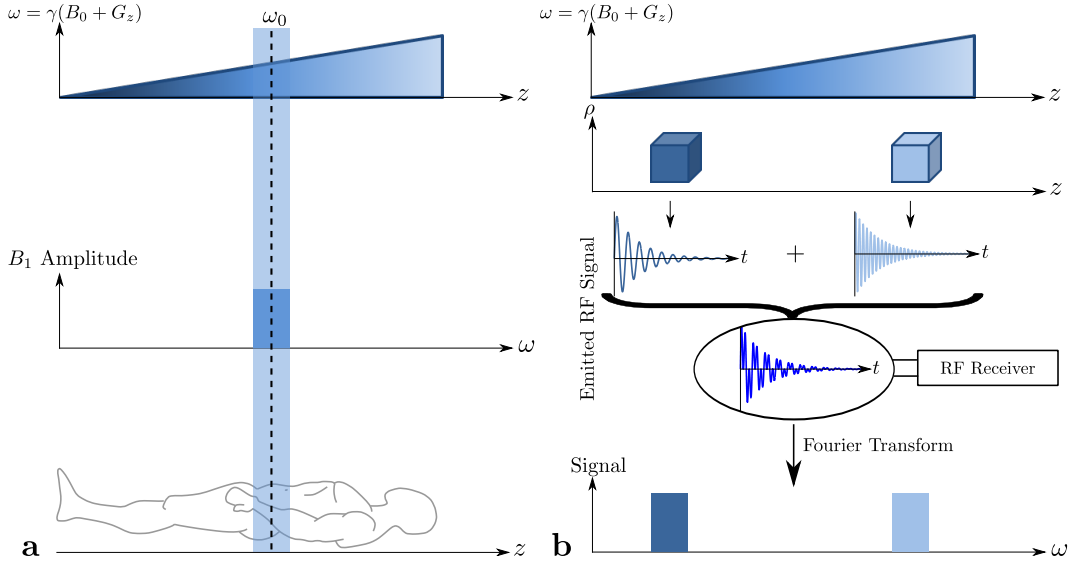


**Fig. 2.1:** Principles of spatial encoding in MRI. **a** Spatial selective excitation. The applied gradient results in a spatial variation of the Larmor frequency. The RF pulse is tuned to the frequency  $\omega_0$  with a finite bandwidth. The RF pulse excites nuclei with Larmor frequencies fulfilling the resonance condition. **b** Frequency encoding in acquisition phase. The Larmor frequencies of the objects having different position in space differ due to the applied gradient. The detected signal is made up by the superposition of the two oscillations. The Fourier projection aligns with the original objects and their positions.

## 2.2 RF Pulse Design

### 2.2.1 Bloch Equation

This section further concentrates on the excitation phase of the MRI experiment. Starting from the fundamental Bloch equation, a range of RF pulse design theory and methods are outlined with regard to multi-channel RF transmission.

The Bloch equation [40, 41] describes the magnetic behavior of a spin ensemble in presence of external fields. The precession of magnetic moments  $\mathbf{M}$  about a time-varying magnetic field  $\mathbf{B}$  in a frame rotating at Larmor frequency is given by:

$$\frac{\partial \mathbf{M}}{\partial t} = \gamma \mathbf{M} \times \mathbf{B} - \mathbf{e}_x \frac{M_x}{T_2} - \mathbf{e}_y \frac{M_y}{T_2} - \mathbf{e}_z \frac{M_z - M_0}{T_1}, \quad (2.3)$$

where  $M_z$  is the longitudinal magnetization,  $M_x$  and  $M_y$  the transverse magnetization components,  $T_1$  the longitudinal and  $T_2$  the transverse relaxation time constant, respectively. The relaxation time constants characterize the influence of proton interaction with neighboring atoms on the net magnetization and are tissue specific. The longitudinal time constant  $T_1$  is also known as the spin-lattice relaxation time constant as it relates to the time required for the tilted longitudinal magnetization  $M_z$  to recover in its thermal equilibrium state  $M_0$ :

$$M_z(t) = M_0 (1 - e^{-t/T_1}) , \quad (2.4)$$

which is the solution of *Equation 2.3* when considering the longitudinal component at  $t = 0$  after tilting the net magnetization into the x-y plane. During this process the time constant  $T_1$  is an inverse measure of the energy transfer efficiency between spins and other nuclei in the lattice.

The transverse time constant  $T_2$  is also called spin-spin relaxation time and denotes the dipole-dipole interaction within single nuclei leading to variations of its precessing frequency. As a consequence, protons following an excitation pulse lose phase coherence of the magnetic moments resulting in a gradually loss of the net transverse magnetization  $M_{xy}$ , i.e. signal dephasing. The loss of the transverse magnetization depends on intrinsic factors, e.g. molecule size and tissue type, and follows an exponential decay after excitation:

$$M_{xy}(t) = M_{xy}(t = 0) e^{-t/T_2} , \quad (2.5)$$

which is again the solution of a simplified model of *Equation 2.3* regarding solely the transverse component with  $M_{xy} = M_x + iM_y$  and its initial magnetization value  $M_{xy}(t = 0)$  after RF excitation. However, in practice the effective transverse relaxation time is shorter due to emerging main field inhomogeneities (see *Section 2.3*). The variations in  $B_0$  superimpose to the intrinsic relaxation effects and accelerate the process of dephasing. The effective time constant  $T_2^*$  describing the actual decay of the transverse magnetization follows the relation:

$$\frac{1}{T_2^*} = \frac{1}{T_2} + \frac{1}{T_2'} , \quad (2.6)$$

with  $T_2'$  being the contribution of the relaxation effects induced by spatial static field inhomogeneities. Both  $T_1$  and  $T_2$  relaxation processes occur simultaneously, where  $T_2$  is always less or equal  $T_1$ .

In the context of MR excitation, the discussed relaxation effects in the Bloch equation can be ignored due to the rather short durations of the RF excitation pulses. Furthermore, the time-varying external magnetic field  $\mathbf{B}$  at spatial position  $\mathbf{r}$  can be decomposed into the gradient  $\mathbf{G}(t)$  and RF  $\mathbf{B}_1(t)$  magnetic field components manipulating the longitudinal and transverse field components, respectively. In the assumption of spatially uniform RF fields, the Bloch equation (*Equation 2.3*) becomes to:

$$\frac{\partial}{\partial t} \begin{pmatrix} M_x(\mathbf{r}, t) \\ M_y(\mathbf{r}, t) \\ M_z(\mathbf{r}, t) \end{pmatrix} = \gamma \begin{pmatrix} 0 & \mathbf{G}(t) \cdot \mathbf{r} & -B_{1,y}(t) \\ -\mathbf{G}(t) \cdot \mathbf{r} & 0 & B_{1,x}(t) \\ B_{1,y}(t) & -B_{1,x}(t) & 0 \end{pmatrix} \begin{pmatrix} M_x(\mathbf{r}, t) \\ M_y(\mathbf{r}, t) \\ M_z(\mathbf{r}, t) \end{pmatrix} . \quad (2.7)$$

### 2.2.2 Single-Channel Transmission

#### Small Tip-Angle Approximation

Due to the non-linear character and complexity of the Bloch equation, its application for practical RF pulse design is limited. A more practical and intuitive approximation was proposed by *Pauly et al.* [42], which allows a straight-forward determination of RF pulse

envelopes for arbitrary shaped excitations. The proposed theory is commonly known as the small tip-angle approximation (STA) and builds the basis of many RF pulse design methods. Basically, the theory assumes that the longitudinal magnetization component remains approximately constant during RF excitation ( $M_z(t) \approx M_0 = \text{const}$ ). This is valid for small flip angles (FAs)  $\alpha$ , where the transverse magnetization follows  $M_{xy} \propto \sin(\alpha) \approx \alpha$ . When imposing this assumption, the longitudinal magnetization component can be decoupled from Equation 2.7 to be linearized. If the equation is further transferred in a complex notation with the applied RF pulse waveform  $B_1(t) = B_{1,x}(t) + iB_{1,y}(t)$ , the following linear solution is obtained for describing the transverse magnetization:

$$M_{xy}(\mathbf{r}) = i\gamma M_0 \int_0^{T_{pulse}} B_1(t) e^{i\mathbf{r}\mathbf{k}(t)} dt \quad (2.8)$$

with  $T_{pulse}$  being the total RF pulse duration and the TX k-space trajectory  $\mathbf{k}$  defined as

$$\mathbf{k}(t) = -\gamma \int_t^{T_{pulse}} \mathbf{G}(s) ds. \quad (2.9)$$

In Equation 2.8, the Bloch equation is reduced to a simple 3-D FT with a multiplicative constant, which reveals a direct and intuitive interpretation how the transverse magnetization is controlled at arbitrary spatial locations by the RF and gradient fields. Precisely, the gradient fields define the path traversing through the TX k-space (Fourier space). Note that the actual k-space position of the k-space trajectory at time-point  $t$  is determined by the remaining negated time integral of  $\mathbf{G}(t)$  from  $t$  to  $T_{pulse}$ . On the other hand, the RF pulse waveform  $B_1(t)$  weights the different positions in k-space along this trajectory via the deposition of RF energy.

In the following, two different approaches are presented to determine the discrete RF pulse values to achieve a desired spatial magnetization pattern. Both methods rely on a pre-defined k-space trajectory, but differ in their numerical ansatz.

### Non-Iterative Fourier Approach

The first technique to calculate the RF waveform exploits the similarity of Equation 2.8 to the FT [42–44]. It employs a direct relationship between the FT of the desired magnetization pattern  $M_{des}$  and the RF pulse waveform  $B_1(t)$ :

$$B_1(t) = -\frac{|\mathbf{G}(t)|}{\rho(\mathbf{k}(t))} \int_{-\infty}^{\infty} \int_{-\infty}^{\infty} M_{des}(\mathbf{r}) e^{i\mathbf{k}(t)\mathbf{r}} dx dy, \quad (2.10)$$

where  $|\mathbf{G}(t)|$  represents the current gradient strength being proportional to the current k-space velocity and  $\rho(\mathbf{k}(t))$  being a density compensation term. The latter term cares for the discrete sampling structure of  $\mathbf{k}(t)$ , i.e. corrects for non-uniform sampling of k-space. Generally, the connection between the one-dimensional time integral of the k-space trajectory and the multi-dimensional Fourier space only holds true, if a bijective transformation between the time-domain and k-space exists, i.e. for non-crossing trajectories. In practice, discretization effects, sufficient encoding of TX k-space (Nyquist theorem) and application specific requirements have to be considered to avoid aliasing and other undesired effects. For

good examples of practical realizations, please refer to [45–47].

However, the direct calculation of the RF samples via the Fourier relationship lacks control of RF power and peak voltages. This can become critical in the matter of RF hardware and SAR constraints. Furthermore, the approach neglects any deviation from the static magnetic field, i.e.  $B_0$  inhomogeneities or off-resonance effects (see *Section 2.3*), which can severely deteriorate the excitation quality.

### Iterative Optimization Approach

To overcome the disadvantages of the Fourier approach, *Yip et al.* [48] formulated the design of multi-dimensional RF pulses as a quadratic optimization problem. The approach includes the compensation for main field inhomogeneities  $\Delta B_0$  induced off-resonance effects and the option to regularize the RF magnitude. Further, the method was shown to be more robust if k-space is undersampled.

The STA (*Equation 2.8*) is again taken as basis for RF pulse design, but is extended by a phase re-winding term to compensate the accrued off-resonance effects during the excitation:

$$M_{xy}(\mathbf{r}) = i\gamma M_0 \int_0^{T_{pulse}} B_1(t) e^{i(\mathbf{r}\mathbf{k}(t) + \gamma \Delta B_0(\mathbf{r})(T_{pulse} - t))} dt. \quad (2.11)$$

The next essential step involves the discretization of the equation in time and space with  $N_t$  and  $N_s$  samples, respectively, and yields a discrete matrix-vector equation:

$$\mathbf{m} \approx \mathbf{A}\mathbf{b}, \quad (2.12)$$

where  $\mathbf{m} = [M_{xy}(\mathbf{r}_1), \dots, M_{xy}(\mathbf{r}_{N_s})]^T$  is the discretized magnetization pattern,  $\mathbf{A}$  the system matrix and  $\mathbf{b} = [B_1(t_1), \dots, B_1(t_{N_t})]^T$  the complex-valued samples of the RF waveform. Essentially, the elements  $a_{ij}$  of the  $N_s \times N_t$  system matrix describe the prevailing physical properties during the excitation, i.e. the chosen k-space trajectory, the temporal and spatial properties and spatial distribution of off-resonance effects:

$$a_{ij} = i\gamma M_0 \Delta t e^{i(\mathbf{r}_i \mathbf{k}(t_j) + \gamma \Delta B_0(\mathbf{r}_i)(t_j - T_{pulse}))}, \quad (2.13)$$

where  $a_{ij}$  is the matrix element at  $i$ th row and  $j$ th column associated with the  $i$ th spatial and  $j$ th temporal sample with a sampling time period of  $\Delta t$ .

The equation builds a system of complex linear equations and states an inverse problem, that can be solved by defining a quadratic optimization problem with the cost function:

$$\hat{\mathbf{b}} = \arg \min_{\mathbf{b}} \{ \|\mathbf{A}\mathbf{b} - \mathbf{m}_{des}\|_{\mathbf{W}}^2 + R(\mathbf{b}) \}, \quad (2.14)$$

where  $\mathbf{m}_{des}$  is the discretized vector of the desired magnetization pattern,  $\mathbf{W}$  a  $N_s \times N_s$  spatial weighting matrix to specify a ROI and  $R(\mathbf{b})$  a regularization term. The regularization term can be used to e.g. dampen undesired high RF magnitudes in  $\mathbf{b}$  by penalizing its total power with  $R(\mathbf{b}) = \beta \|\mathbf{b}\|^2$ . The latter is also known as Tikhonov regularization with regularization parameter  $\beta$ , which balances the excitation error, i.e. the distance to the desired magnetization pattern, and integrated RF power. Overall, the iterative method



provides a numerically optimized RF waveform  $\mathbf{b}$ , which implicitly considers potential variable-density k-space sampling schemes by the k-space trajectory, don't-care regions via spatial masking and a variety of regularization terms. Clearly, the flexibility in adopting to various factors is hard to achieve with non-iterative methods.

This fundamental work is also the basis of the most commonly used RF design approach in parallel transmission. Therefore, details regarding algorithms to solve the stated minimization problem and the influence of the Tikhonov regularization term are covered in the subsequent section.

### 2.2.3 Parallel Transmission

#### Introduction

Although, the STA offers a wide range of opportunities for arbitrary dimensional spatially selective RF pulses, their potential applications are mainly encumbered with the resulting long pulse durations. Especially, 2-D or 3-D selective excitations require k-space trajectories sufficiently covering the spatial-spectral range of TX k-space according to the Nyquist sampling theorem. As the k-space traversing trajectory is further encoded by the gradient fields, its design has to obey the given gradient system hardware amplitude and slew-rate limitations. Based on conventional gradient hardware with maximal gradient strength of 45 mT/m and maximal slew-rate of 200 T/m/s, minimal pulse durations are constrained to the order of 10 – 20 ms for 2-D [45–48] and beyond 30 ms for 3-D spatially selective RF pulses [44, 49], respectively. These unacceptably long pulse durations may be problematic due to numerous reasons. Next to the afore-mentioned off-resonance effects, magnetization transfer and relaxation effects during the excitation phase do further compromise image quality. Although, RF pulse design methods are able to compensate for such effects, they rely on proper estimations of e.g.  $B_0$  maps, which is non-trivial in human in-vivo experiments. Secondary disadvantages include the prolonged echo time (TE) contribution of the excitation pulse and increased repetition time (TR), which may lead to reduced SNR in fast imaging sequences and longer total acquisition times.

With the introduction of parallel transmission (pTx) it was shown that significantly shorter excitations can be achieved, while maintaining the overall excitation quality [2–4]. Similar to the parallel imaging sensitivity encoding (SENSE) method [50], the distinct TX sensitivity profiles of the multiple RF excitation coils can be used to enable a reduced k-space sampling during RF transmission without aliasing effects (*Figure 2.2*). With respect to the single channel implementations, the sparser TX k-space sampling is also known as RF pulse acceleration or TX SENSE. Alternatively, the increased spatial degrees of freedom can be also utilized to mitigate  $B_1$  inhomogeneity effects [6, 12, 51, 52] or SAR deposition [9, 53, 54] at (ultra-) high-field MRI. The basic pTx RF design method, extensions and practical framework shall be recapitulated in the following.

#### Spatial Domain Design Approach

The spatial domain design approach introduced by *Grissom et al.* [4] is the multi-coil generalization of the iterative pulse design method described above [48]. In contrast to the

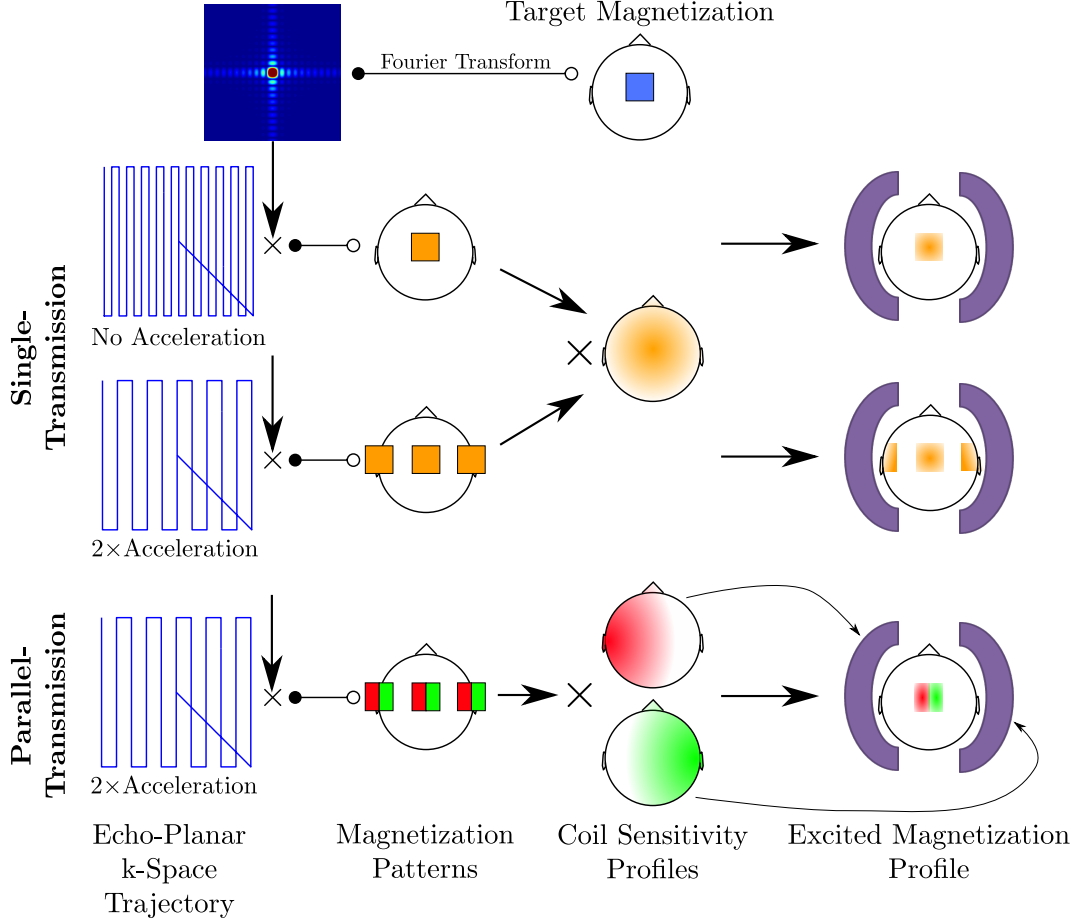


**Fig. 2.2:** Schematic illustration of TX SENSE with RF pulse acceleration factor 2 based on an echo-planar TX k-space trajectory. The single-coil transmission follows the strategy of *Section 2.2.2*. An undersampled k-space trajectory in combination with the global coil sensitivity profile results in aliasing/wrap-around effects. When employing the undersampled trajectory with parallel transmission, the distinct coil profiles of the two orthogonal coils can be utilized to produce the target magnetization without aliasing.

initially proposed pTx RF pulse design methods [2, 3], it again supports arbitrary k-space trajectories, off-resonance correction and a spatial weighting of the cost function. For that purpose, the STA in *Equation 2.11* is extended by multiple RF coils with spatially resolved TX sensitivity profiles  $S_c(\mathbf{r})$ :

$$M_{xy}(\mathbf{r}) = i\gamma M_0 \sum_{c=1}^C S_c(\mathbf{r}) \int_0^{T_{pulse}} B_{1,c}(t) e^{i(\mathbf{r}\mathbf{k}(t) + \gamma \Delta B_0(\mathbf{r})(T_{pulse} - t))} dt, \quad (2.15)$$

where  $C$  is the number of TX channels and  $B_{1,c}(t)$  the RF waveform of the  $c$ th RF channel. Here, the overall magnetization pattern is composed of the linear spatial superposition of the excitation patterns from multiple transceivers. After discretization, the full system matrix

$\mathbf{A}_{full}$  consists of a concatenation of the original system matrix  $\mathbf{A}$  (Equation 2.13) that is weighted channel-wise by the spatial coil sensitivity profile:

$$\mathbf{m} \approx \mathbf{A}_{full} \mathbf{b}_{full} = [\tilde{\mathbf{S}}_1 \mathbf{A} \cdots \tilde{\mathbf{S}}_C \mathbf{A}] \begin{bmatrix} \mathbf{b}_1 \\ \vdots \\ \mathbf{b}_C \end{bmatrix}, \quad (2.16)$$

where  $\tilde{\mathbf{S}}_c = \text{diag}\{S_c(\mathbf{r})\}$  is diagonal matrix containing samples of the  $c$ th TX sensitivity profile and  $\mathbf{b}_c$  the discretized RF waveform of the  $c$ th RF coil with  $N_t$  samples. Given a k-space trajectory  $\mathbf{k}$  and  $B_0$  map  $\Delta B_0$ , the complete system matrix  $(\mathbf{A})_{full}$  again describes the physical situation with dimensions  $N_s \times CN_t$ .

A reasonable estimate of the respective  $B_1$  waveforms  $\hat{\mathbf{b}}_{full}$  with adequate spatial fidelity to a given magnetization pattern  $\mathbf{m}_{des}$  can again be obtained by the formulation and solution of a quadratic minimization problem (Equation 2.14). Depending on the discretization level, number of RF channels, spatial excitation resolution and target pattern, the high dimensional complex system of equations can be both over- and under-determined and requires a robust solving algorithm with sufficient computation speed and convergence. In an elaborate study, *Zelinski et al.* [55] have found the least-squares QR decomposition (LSQR) solver to outperform the singular value decomposition (SVD) based inversion and conjugate gradient least-squares (CGLS) solver in terms of excitation quality and regularized RF power deposition. To find the appropriate balance between excitation fidelity and RF power deposition, the L-curve criterion [56, 57] can be used to determine a suitable regularization parameter  $\beta$ . RF channel-dependent regularization has been shown to be advantageous to reduce local and global SAR [58], but at cost of increased computational complexity.

So far, the cost function of the described optimization problem minimizes both the magnitude and phase difference to a pre-defined magnetization pattern, i.e. a complex least-squares (CLS) optimization. While the convex cost-function allows a direct approximation of the global optimum, the phase distribution of the achieved magnetization is often not of interest. Rather, an RF solution is desired, which provides the minimal distance to the magnitude of the target pattern among all possible phase distributions:

$$\hat{\mathbf{b}}_{full} = \arg \min_{\mathbf{b}_{full}} \{ \|\mathbf{A}_{full} \mathbf{b}_{full} - \mathbf{m}_{des}\|_{\mathbf{W}}^2 + R(\mathbf{b}_{full}) \}, \quad (2.17)$$

However, in this case the determination of the global optimum is no longer guaranteed due to the non-convex nature of the optimization problem. To this end, *Setsompop et al.* [15] proposed a variable exchange method, which iteratively relaxes the target phase to the previously obtained phase pattern. The magnitude least-squares (MLS) method was shown to provide improved excitation accuracy with significantly reduced RF power.

## Simultaneous Gradient and RF Optimization

pTx has shown great potential to shorten RF pulse durations by the introduction of additional spatial degrees of freedom. In fact, RF pulses can be designed on the basis of downsampled k-space trajectories without occurring aliasing effects [2–4], but still rely on static and predefined k-space trajectories. Considering that the Fourier relationship is not feasible with pTx (the resulting excitation pattern is not a direct FT of each pulse, see Equation 2.16),

the choice of the k-space trajectory path can leave significant room for improvement. The simultaneous optimization of both the gradient/k-space trajectory and RF waveforms has been widely employed in the field of slice-selective RF pulse design optimizing so-called fast- $k_z$  trajectories [6, 59–62]: Fast- $k_z$  or ‘spokes’ RF pulses use fixed slice-selective RF waveforms played along the  $k_z$  k-space direction. A sparse selection of spokes locations in the  $k_{xy}$  plane and suitable RF waveform weights are mostly optimized with the objective to mitigate  $B_1$  inhomogeneity effects. Typically, the optimized locations are near to k-space center to introduce low spatial frequencies tackling the spatially slow varying  $B_1$  transitions. Similar, this approach was transferred to non-selective RF pulses optimizing a RF time course and a small number of sampling positions in 3-D k-space [12, 16]. Finally, a joint gradient and RF optimization was applied to multi-dimensional spatially selective RF pulses [63, 64], which can further shorten the RF pulse durations.

To determine the optimal k-space trajectory either Fourier driven [12, 59], greedy [60, 61, 64], sparsity penalized [6] or a combination of local and greedy optimization methods [62] were proposed. However, all approaches have in common that they can considerably increase the computational demands. The already complex RF waveform optimization for multiple channels is encapsulated by another optimization loop that aims to find the proper k-space trajectory parameterization.

## SAR Optimization

Safety regulations require the application of RF pulses not to exceed strictly defined tissue warming limits [65]. For this purpose, global (power absorbed by whole body) and local (power absorbed by 10 g of tissue) SAR metrics have been established to approximate the degree of global and local tissue heating. However, with the simultaneous application of independent waveforms by multiple geometrically arranged RF transmitters, the SAR evaluation is more complicated. In particular, the regularization of the forward RF power [4, 15, 66] is not necessarily sufficient to control local SAR due to the complex interference scenarios between the electric fields generated by the different TX channels [5, 54, 67, 68]. To encounter generally a SAR increase, different methods have been suggested. First, k-space trajectories can be adapted to provide a RF energy efficient design [69–71], but which do not deterministically lower the local SAR expense. Further, regularization strategies have been introduced to tackle global SAR [3] and local SAR [58] by either common or channel specific RF power penalties. Finally, constraint optimization methods showed great potential to explicitly limit global and local SAR, but also considering the RF hardware constraints [9, 13, 53]. In this process, the iterative numerical prediction of the SAR expense can be tremendously reduced by model compression techniques [72, 73].

## Large Tip-Angle Design

When intending to design RF pulses with FA beyond  $30^\circ$ , e.g. saturation ( $90^\circ$  FA) or refocusing/inversion pulses ( $180^\circ$  FA), the non-linear characteristic of the Bloch equation cannot be neglected any longer. Here, the linear relation between the transverse magnetization and the applied excitation field loses its validity as the variation of the longitudinal magnetization component has to be considered. Therefore, large tip-angle RF pulses designed with the STA, which assume the longitudinal magnetization to remain constant (*Section 2.2.2*), are likely to result in non-optimal excitation performance.

Different hybrid methods [66, 74–77] have been proposed to fill the gap between STA and the Bloch equation. All methods try to capture the non-linear evolution of the magnetization, while maintaining the reduced complexity of the STA: The non-iterative linear class of large tip-angle (LCLTA) approach is based on the early work of *Pauly et al.* [74] and was later extended to the pTx regime [66, 75]. Basically, a concatenation of a sequence of small-excitation pulses is used, where each subpulse has to be inherently self-refocused. Thus, the method is limited only to certain k-space trajectories, which approximately fulfill this requirement. In contrast to that, the additive angle method (AAM) [76] works iteratively and is not restricted to specific k-space trajectory types. To minimize the distance to the desired pattern, small tip-angle pulses are systematically updated. At each iteration the deviation between the excitation of summed pulses and the desired pattern is first estimated. Then another small tip-angle pulse is added to further improve the spatial fidelity of the summed pulses. This procedure is repeated until a convergence criterion is met. Similar, to AAM, the perturbation analysis (PTA) approach [77] evaluates the STA deviation to the target magnetization, but as an analytically function of the applied RF pulse. This function is subsequently used to iteratively calculate a correction term, which has been shown to be more robust for higher acceleration factors.

Full non-linear high FA pTx RF pulse optimizations were presented in [78–80] and are based on optimal control theory. This method has also no restrictions regarding k-space trajectories and uses the result from STA (or from another high-flip algorithm) as an initial guess. Multiple controls are defined directly on the Bloch equation to search the parameter space for the optimal solution. The method was demonstrated to perform well for arbitrary large tip-angle pTx RF pulses. However, computation times and memory consumption can be more intensive compared to the hybrid methods.

### TX k-Space Trajectories

Most characteristics of an RF pulse are determined by the underlying TX k-space trajectory. In particular, the spatial dimension and selectivity, the total RF pulse length and coverage of TX k-space are given by the trajectory encoding gradient waveforms. Moreover, it was shown that the choice of k-space sampling can greatly influence both the resulting excitation fidelity (see *Section 2.2.3*) and RF power/global SAR dissipation (*Section 2.2.3*). Many different static and dynamically optimized trajectory designs have been suggested addressing  $B_1$  inhomogeneity mitigation up to the selection of sub-volumes of arbitrary shape and dimension.

In *Figure 2.3* a selection of common TX k-space trajectory designs are illustrated. First, tailored non-selective excitations (*Figure 2.3a,b*) have been shown to benefit from sampling of a few optimized locations in multi-dimensional k-space. Depending on the RF sampling strategy, i.e. whether RF is applied continuously or solely point-wise during the k-space transition, one can refer to the spiral non-selective (SPINS) [16] or  $k_T$  points [12] trajectory. Second, spokes-based trajectories with additional sparse sampling of the  $k_{xy}$  plane have been proven advantageous in combination with slice-selective waveforms (*Figure 2.3c,d*) for  $B_1$  inhomogeneity mitigation [6, 60–62] (see fast- $k_z$  methods in *Section 2.2.3*). When optimizing single RF samples instead of fixed RF waveforms, the trajectory spokes are also denoted as ‘rungs’ and were successfully used in pre-compensating through-plane susceptibility induced signal loss [14, 59, 81, 82]. Clearly, the spokes can be arranged to build an echo-planar (EP) trajectory, which is also suited for 2-D excitations. In combination with slice selective sub-pulses the EP trajectory is often used in the context of inner-volume excitation [45, 46, 83]. Third, 2-D spatially selective excitations (*Figure 2.3e-g*) are mainly based on 2-D spiral

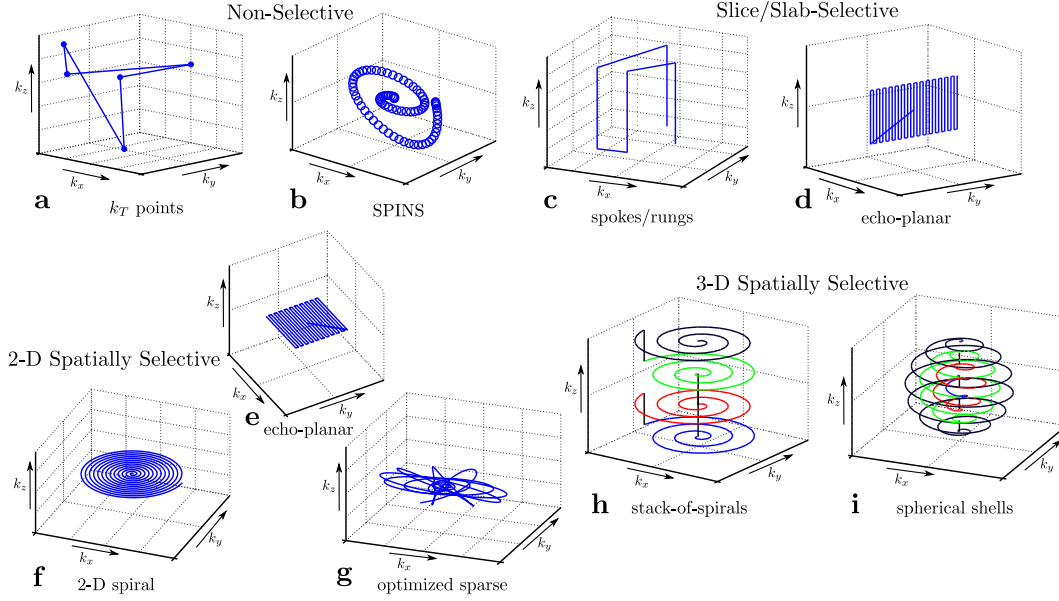


**Fig. 2.3:** Selection of TX k-space trajectories. Depending on the application purpose, different k-space designs have been suggested. Non-selective excitation: **a**  $k_T$  points and **b** SPINS. Slice selection: **c** spokes and **d** echo-planar trajectories. 2-D spatially selective excitation: **e** echo-planar, **f** 2-D spiral and **g** optimized sparse trajectories. 3-D spatially selective excitation: **h** stack-of-spirals and **i** spherical shells trajectories.

trajectories due to its time-efficiency covering the k-space [4, 15, 54, 70, 84, 85]. Next to the 2-D spiral and EP trajectory, arbitrary shaped sparse trajectory paths can be optimized [64]. Last, stack-of-spirals and spherical shells trajectories have been shown suitable for 3-D selective excitations [17, 86] (Figure 2.3h,i). Those trajectory types are capable for a deterministic TX acceleration, which is important to reduce the extensive 3-D k-space encoding and the RF pulse durations.

Independent from the desired k-space trajectory, the corresponding gradient design must be in compliance with the given gradient hardware limits. Apart from proposed analytical designs for certain trajectory types [87–90], a time-optimal design was presented to realize arbitrary trajectories within hardware constraints [91]. However, the actual applied k-space trajectory might still significantly differ from the theoretically calculated one due to technical imperfections and interfering gradient effects and can result in poor excitation performance. Several practical issues, e.g. anisotropic timing delays of the gradient amplifiers and superimposed eddy current terms, have to be considered regarding the robustness of the optimized pTx RF pulse and may require additional calibrations of the actual k-space trajectory [16, 92, 93].

### Practical Framework and Considerations

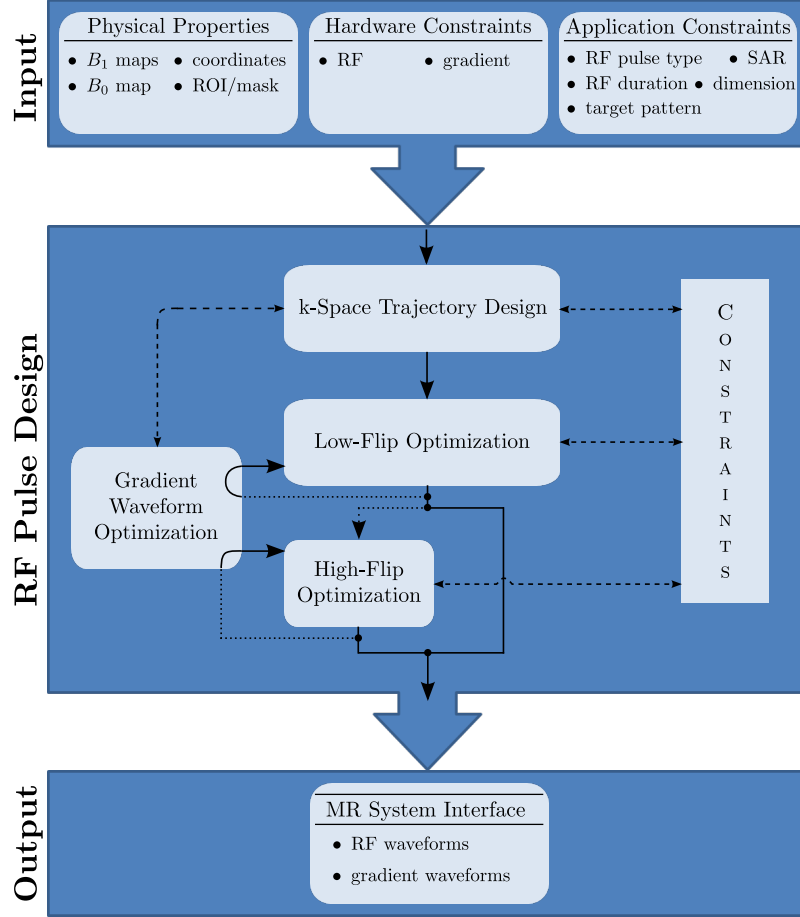


**Fig. 2.4:** Overview of pTx RF pulse design framework. The RF pulse design process is based on various input information describing the prevailing physical properties and defining the hardware and application specific requirements. Based on the input data an appropriate TX k-space trajectory can be chosen before optimizing in the low-FA regime (*Section 2.2.3*). Optionally, gradient waveform and/or high-FA can be performed to further improve quality. During optimization all given constraints have to be considered to ensure the application of the ultimate RF pulse. Finally, the gradient and RF waveforms are handed over to the MR system hardware interface.

Since its introduction, the pTx technology has established a new “zoo” of methodologies to improve the overall excitation quality, but also imaging performance in MRI. A possible framework describing the practical RF pulse design workflow including most features is shown in *Figure 2.4*. Clearly, before making use of the potential benefits coming along with pTx, various input information has to be determined before optimization: First, the physical properties of the experimental situation have to be obtained, i.e. the measurement of the prevailing TX coil sensitivity profiles ( $B_1$  maps) and static field inhomogeneities ( $B_0$  map)

at the given spatial location. Typically, the  $B_1$  and  $B_0$  maps are acquired at the beginning of the scanning schedule and once per examination area, e.g. once for brain and once for body examinations. Based on these images, also a binary mask can be calculated to separate the background noise from the subject to serve as the ROI for subsequent RF pulse optimizations. Note, that this information is very crucial for the successful design of RF pulses, as the minimization procedure aims to compensate for the inhomogeneous field distributions within the ROI. In other words, if the ROI is not well defined or the  $B_0$  map is corrupted by phase-wraps [94], the optimized RF pulse may significantly deteriorate image quality. Similar issues can arise, when the subject is moving and the whole physical situation changes. The assessment of reliable  $B_1$  and  $B_0$  maps in-vivo is non-trivial and is still an on-going research field. For established methods, please refer to [95–101] for  $B_1$  and to [94, 102–106] for  $B_0$  mapping.

Second, RF and gradient hardware limits have to be considered during the RF pulse design to ensure their successful application. The gradient hardware limits are directly influencing the RF pulse duration by encoding the underlying TX k-space trajectory with a finite k-space traversing velocity. The RF amplifier sets the maximum applicable RF power and can thus, also indirectly restrain the achievable FA level.

Last input information includes the application specific constraints and requirements. The RF pulses to be optimized can cover excitation, saturation or inversion, which can completely differ in their characteristics next to their FA level. The RF optimization can involve different spatial dimensions, target patterns or spectral-spatial specificity. Further, the summation of all RF pulses in the duty-cycle are not allowed to exceed the SAR limits. However, the number and properties of optimized RF pulses, the SAR balance and RF pulse timing in an imaging sequence can greatly fluctuate and be challenging to assess in advance. In summary, the application specific constraints define the scope and the target purpose of the RF pulse optimization.

After gathering and defining all the input information, the RF pulse design process starts with the calculation of an appropriate TX k-space trajectory. Depending on the spatial dimension, coverage and shape of the target magnetization pattern, a suitable trajectory type can be appointed (*Section 2.2.3*). The spatial excitation resolution required by the target magnetization and given field of excitation (FOE) directly determine the extent and density of k-space sampling. The final trajectory path has to be realized within gradient hardware limits and is taken as a basis for the following RF waveform optimization. For many clinical relevant classes of RF pulses, the low-FA optimization (*Section 2.2.3*) is entirely sufficient and needs no sequential steps for further improvement of the magnetization performance. Although, the fundamental STA is theoretically valid for FA below  $30^\circ$ , the assumption was shown to perform well for FA up to  $90^\circ$  [42]. Due to its straight-forward and fast design, many applications can be limited to this single optimization step. However, to further improve the magnetization fidelity for e.g. inversion pulses, high-FA optimization strategies can be pursued (*Section 2.2.3*) using the low-FA solution as an initial guess. Optionally, gradient waveform optimization can be iteratively applied to gain in both improved performance and reducing the RF pulse duration (*Section 2.2.3*). However, these optional optimization steps are linked with increased computational demands. Certainly, the given SAR and hardware constraints have always to be considered during optimization.

Finally, the ultimate gradient and RF channel specific waveforms are transferred to the MR system hardware interfaces, where additional safety checks can be run before their application.



Although, in most cases the whole RF pulse optimization process can be reduced to a single step, i.e. low-flip optimization, the computational complexity and demands must not be under-estimated or ignored. *Figure 2.5* illustrates various accumulative factors, which directly contribute to the computational expenditure. Bearing the mandatory constraints in mind, it is challenging to find the proper trade-off between quality and computation time. Clearly, this trade-off and compromises in quality have often to be determined individually for each application to fulfill the clinical requirements.

In conclusion, the aims of the (clinically capable) pTx RF pulse optimization are:

- Accurate magnetization quality.
- RF pulse durations as short as possible due to its direct influence on TE, TR and off-resonance effects.
- Abiding all practical constraints, i.e. hardware and SAR constraints.
- Moderate computational complexity.
- Low sensitivity or inherent robustness towards errors driven by technical inaccuracy, e.g. gradient or RF deviations.

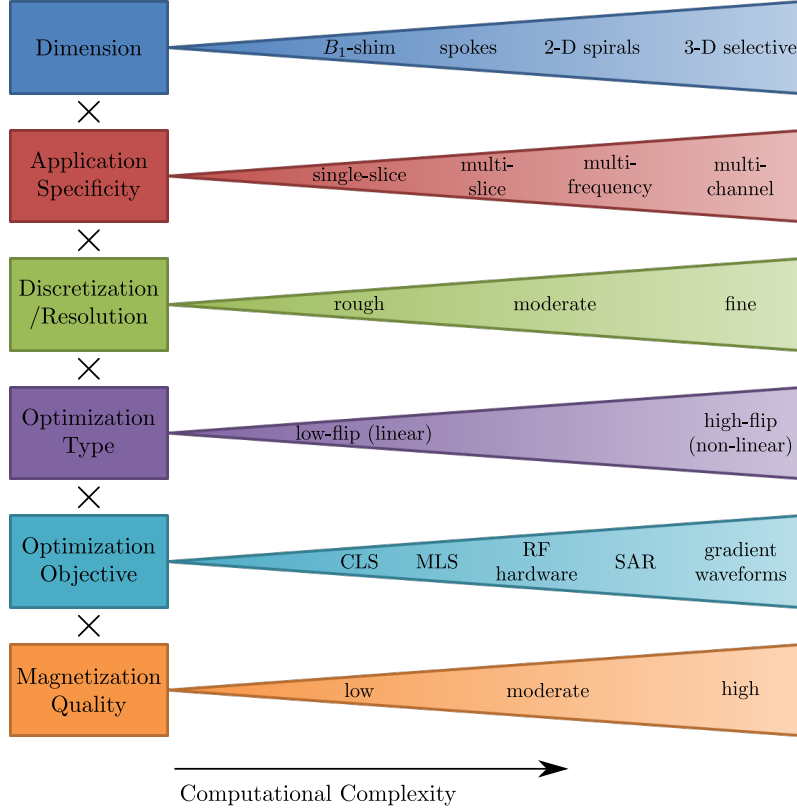


**Fig. 2.5:** Computation complexity of pTx RF pulse design. Different *multiplying* factors influencing the computational demands of the RF pulse optimization. Note, that in some categories multiple options are possible at the same time, e.g. multi-slice combined with multi-frequency and low-flip with subsequent high-flip optimization. Depending on the scenario, the resulting computation time can vary from real-time ( $< 1$  s) to clinically unacceptable durations ( $> 24$  h).

## 2.3 Off-Resonance

### 2.3.1 Sources

This section gives a brief outline about the off-resonance phenomena in MRI. Generally, off-resonance effects cover atomic nuclei, which experience a different precessing frequency than theoretically expected within an ideal system.

There are several sources of off-resonance resulting in an effective distortion of the static magnetic field  $B_0$  changing its magnitude. The sources can be distinguished between static ( $\Delta B_{0,static}(\mathbf{r})$ ) and dynamic ( $\Delta B_{0,dyn}(\mathbf{r}, t)$ ) field offsets, where static denotes components that remain approximately constant during the acquisition time of an imaging sequence:

$$\begin{aligned}
B_0(\mathbf{r}, t) = & B_{0,nominal} \\
& + \underbrace{\Delta B_{0,tec}(\mathbf{r}) + \Delta B_{0,\chi}(\mathbf{r}) + \Delta B_{0,CS}(\mathbf{r})}_{\Delta B_{0,static}(\mathbf{r})} \\
& + \underbrace{\Delta B_{0,conc}(\mathbf{r}, t) + \Delta B_{0,EC}(\mathbf{r}, t) + \Delta B_{0,mot}(\mathbf{r}, t) + \Delta B_{0,phys}(\mathbf{r}, t) + \Delta B_{0,dyntec}(\mathbf{r}, t)}_{\Delta B_{0,dyn}(\mathbf{r}, t)} .
\end{aligned} \tag{2.18}$$

The effective magnetic main field and its static and dynamic constituents can be further subdivided into:

- **Nominal static magnetic field strength  $B_{0,nominal}$**  : This is the nominal perfectly uniform magnetic field of e.g. 1.5 T, 3 T or above.
- **Static technical imperfections  $\Delta B_{0,tec}(\mathbf{r})$**  : In general, the technically achievable  $B_0$  homogeneity is very high around the isocenter. The magnet manufacturers state homogeneity deviations down to  $< 1$  ppm within a 50 cm-diameter spherical volume [107, 108], i.e. less than 100 Hz at 3 T.
- **Susceptibility variation  $\Delta B_{0,\chi}(\mathbf{r})$**  : As soon as an object is placed into the scanner magnet, the static magnetic field is superimposed by local  $B_0$  field variations produced by susceptibility differences/gradients of bordering materials, such as air, water, tissue and metal (implants). The magnetic susceptibility  $\chi$  is a physical property that characterizes the degree of magnetization of a material placed in an external magnetic field. The parameter is dimensionless and related to the relative permeability  $\mu_r$ :

$$\chi = \mu_r - 1 = \frac{\mu}{\mu_0} - 1 , \tag{2.19}$$

where  $\mu$  is the effective permeability and  $\mu_0$  the permeability of free space. With  $B_0$  being oriented along the positive z direction, the susceptibility induced field perturbations can be approximated by [109]:

$$-\chi(\mathbf{r})B_0 \leq \Delta B_{0,\chi}(\mathbf{r}) \leq \chi(\mathbf{r})B_0 , \tag{2.20}$$

with  $\chi(\mathbf{r})$  being the spatial susceptibility distribution in the human body. Hence, the impact of susceptibility based field perturbations rises linearly with the main magnetic field strength. For human tissues, which mainly consists of diamagnetic properties, the values are  $|\chi| \ll 1$  and range from  $-10$  ppm (lipids) to  $-6.52$  ppm (desoxygenated blood cell) [109]. Due to the distinct gap to the magnetic susceptibility behavior of air ( $\chi = 0.36$  ppm), the tissue/air borders within the human body do certainly produce the major local field interference (except for metal implants). In the human head, such pronounced areas can be found near the air sinuses, frontal and temporal lobe. Overall, the great susceptibility variety in the human body results in a subject-specific and spatially complex distribution of local field distortions.

- **Chemical shift  $\Delta B_{0,CS}(\mathbf{r})$**  : The chemical shift originates from protons experiencing different electron environments in the presence of an applied magnetic field. In particular, protons in e.g. lipids, silicone or water are embedded in different molecular environments, in which the circulating electrons yield an unequal nuclear shielding effect against the external magnetic field and thus different resonance frequencies. The strength of the

nuclear shielding can be measured in the difference of the resonance frequencies relative to another. In terms of MRI, this can be interpreted as a frequency offset relative to the static magnetic field being tuned to water:

$$\Delta B_{0,CS}(\mathbf{r}) = \delta(\mathbf{r})B_0, \quad (2.21)$$

where the chemical shift  $\delta(\mathbf{r})$  at position  $\mathbf{r}$  and its deviation in the Larmor frequency (see *Equation 2.1*) linearly scales with the main field strength. The difference in chemical shift of fat-like hydrogens and water is approximately  $\delta_{fat} = 3.4$  ppm, which corresponds to a frequency separation of  $\approx 440$  Hz at 3 T.

- **Concomitant (Maxwell) fields  $\Delta B_{0,conc}(\mathbf{r}, t)$**  : As soon as a linear gradient field is imposed to enable the spatial encoding during the excitation or acquisition phase of the MRI experiment, additional gradient fields are produced as a result of the Maxwell equations. Precisely, spatial field components of higher order, i.e. concomitant or Maxwell fields, are produced being perpendicular to the main field orientation axis (z-axis). Hence, the orientation of the net magnetization  $M_0$  is caused to slightly diverge from its original orientation and accumulates an additional phase, whenever a linear gradient is activated. Assuming cylindrical gradient coils, the lowest order approximation of concomitant field offset at spatial location  $\mathbf{r} = [x, y, z]^T$  yields [35, 110]:

$$\begin{aligned} \Delta B_{0,conc}(x, y, z; t) = \frac{1}{2B_0} & \left[ \frac{G_z^2(t)}{4}(x^2 + y^2) + (G_x^2(t) + G_y^2(t))z^2 \right. \\ & \left. - G_x(t)G_z(t)xz - G_y(t)G_z(t)yz \right]. \end{aligned} \quad (2.22)$$

Here, the magnitude of the concomitant fields is inversely proportional to the magnetic field strength and scales quadratically with the amplitude of the applied gradient. The concomitant fields follow directly the temporal and spatial course of the *active* gradient fields, but can be analytically calculated for a given gradient waveform. However, at higher field strengths the effect of concomitant fields can be neglected, when moderate gradient strengths are used [35].

- **Eddy currents  $\Delta B_{0,EC}(\mathbf{r}, t)$**  : As described above, gradient fields are time-varying fields required to encode the image space. According to Faraday's law of induction, the changing magnetic flux induces currents, i.e. eddy currents, in the magnet bore, the gradient coils themselves and other conducting parts of the MR system. Similar to the concomitant fields, the spatially-varying induced field produced by the eddy currents superimpose  $B_0$ , once gradients are applied. However, the field properties are different in many aspects [35]: The field distortions endure and only slightly decay after the gradients are being switched off. As the field perturbation is associated with the change of the magnetic flux, they scale with the temporal derivation of the gradient magnitudes and antagonize its origin (Lenz's law). The field components created by the eddy currents can be modeled with the changing gradient waveforms convoluted with a sum of decaying functions [35, 111, 112]:

$$\Delta B_{0,EC}(\mathbf{r}, t) = -\frac{\partial G(\mathbf{r}, t)}{\partial t} \otimes \left[ h(t) \sum_n \alpha_n e^{(-t/\tau_n)} \right], \quad (2.23)$$

with  $h(t)$  being the unit step function,  $\alpha_n$  the  $n$ th amplitude and  $\tau_n$  the  $n$ th time constant of the exponential functions characterizing the resistance and inductance of the corresponding circuits, respectively. Consequently, the influence of the eddy currents distortions rise linearly with the current gradient slew-rate and are independent from the main magnetic field strength. Typical values for amplitude and time constants range from  $0.001 - 0.05$  and  $1 - 100$  ms, respectively and have to be empirically calibrated [35, 112].

- **Gross subject motion  $\Delta B_{0,mot}(\mathbf{r}, t)$**  : Clearly, the effective static magnetic field is also time-varying due to the non-stationary movement of the subject to be examined. During the scanning procedure and between protocol breaks, unconscious and conscious body movements of the patient lead to a continuous change of the spatial position of tissues with different susceptibility and/or chemical shift properties. As a consequence, the  $\Delta B_{0,\chi}$  and  $\Delta B_{0,CS}$  field components show a dynamic and non-predictable deformation, which increases with the magnitude of spatial displacement.
- **Physiological effects  $\Delta B_{0,phys}(\mathbf{r}, t)$**  : The gross subject motion is superimposed with the physiological movement of inner organs as the heart and digestive system, the blood or cerebrospinal fluid pulsation and breathing cycle. These effects can significantly change the position of the abdominal wall and associated organs, but also the volume properties of tissue filled with air. For example, field perturbations of the human spine showed fluctuations of  $\approx 45$  Hz at 3 T due to respiration [113]. Respiration induced fluctuations were even reported to produce virtual motion artifacts in the brain at 1.5 T [114].
- **Dynamic technical noise  $\Delta B_{0,dyntec}(\mathbf{r}, t)$**  : The dynamic field perturbations of the dynamic technical noise summarizes different effects regarding the stability of the technical setup and potential external disturbing sources. The latter can stem from insufficient shielding of the MR scanner room, so that external magnetic fields from e.g. other medical devices can additionally compromise the main field homogeneity. Regarding the stability of the MR scanner's technical components, heating processes due to extensive and/or long-term usage of the gradient coils can lead to a significant drift of the magnetic field. In particular, eddy currents can heat up materials near the magnet's bore and can cause temporally and spatially field variations of the order of  $0.8 - 2.5$  ppm [115]. Moreover, mechanical vibrations of the gradient coils can further heat up shielding elements via regular mechanical stress and friction or can even facilitate subject movement, when being transferred to the patient table [116].

In summary, the effective static magnetic field is disturbed by various off-resonance sources, which show coupling effects and steady mutual influence. Although, a variety of methods have been proposed to mitigate the  $B_0$  inhomogeneity components, some residual field deviations remain in practice. Especially, the influence of the patient specific offset components, i.e. susceptibility, chemical shift and movement induced distortions are challenging to compensate. With respect to pTx RF pulse design, a static field offset map  $\Delta B_0 = \Delta B_{0,static}$  can be considered during optimization (Section 2.2.3), which is mainly dominated by susceptibility component.

### 2.3.2 Effects

Generally, the macroscopic effect of off-resonance results in a deterioration of the MR image quality. In the following, the off-resonance effects of the static magnetic field inhomogeneities  $\Delta B_{0,static}$  are presented in more detail. Here, the magnitude of image distortions associated

with off-resonance effects depends heavily on the imaging sequence type<sup>1</sup>. Spin-echo (SE) or turbo spin-echo (TSE) imaging sequences show only subtle sensitivity towards off-resonance effects. In contrast, fast and ultra-fast imaging sequences, e.g. gradient recalled echo (GRE), echo-planar imaging (EPI) or spiral imaging, are very sensitive due to the missing  $180^\circ$  RF pulses that refocus the phase error accumulation [35]. Consequences of the phase error accumulation during the frequency-phase encoded acquisition process are:

- **Spatial distortions:** The frequency offset leads to a spatial mis-registration in the frequency encoding direction (see *Figure 2.1b*), which is most pronounced in the presence of chemical shift effects. Signals arising from fat tissue experience a constant spatial shift, which is typically in the order of a few pixels in conventional GRE sequences acquiring the k-space signal line-by-line. This becomes more critical in the phase-encoding direction in EPI, where the complete k-space is acquired at once. Phase errors can evolve during the whole image encoding process and cause a prominent global shift in dimensions of the image size. These effects are superimposed by the smaller, but spatially more complex field deviations produced by the susceptibility effects. Especially in EPI and spiral imaging, they provoke strong local geometric distortions severely compromising the image quality [35, 109, 117].
- **Signal loss:** Due to local off-resonance, i.e. mainly susceptibility effects, variations of the Larmor frequency appear within an image voxel. Consequently, the spins or net magnetization in a voxel start to loose phase coherence and destructively interfere (see  $T_2^*$  decay in *Section 2.2.1*). The intra-voxel dephasing arising with off-resonance can result in a noticeable local signal loss, which is often found near air-tissue interfaces or metallic implants [118, 119].
- **Blurring:** In ultra-fast imaging sequences, where the image k-space data is acquired at different times of the  $T_2^*$  decay, the various  $T_2^*$  results in a reduction of spatial resolution [117]. This image blurring effect is enhanced with shorter  $T_2^*$  values, which is again fostered by the local off-resonance effects.

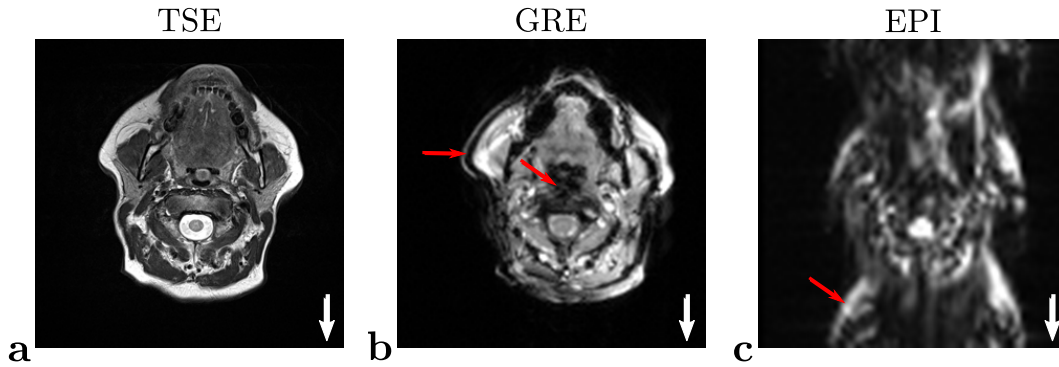


**Fig. 2.6:** Off-resonance effects in different imaging sequences. Axial slice near lower jaw acquired with **a** TSE, **b** GRE and **c** EPI. Image phase encoding direction is indicated with a white arrow. Off-resonance effects are highlighted with red arrows.

<sup>1</sup> For a detailed discription of various imaging sequences please refer to [34–36].

Finally, all off-resonance effects interfere with each other giving rise to complex image artifacts. *Figure 2.6* exhibits different levels of image distortions depending on the imaging sequence. As described above, TSE is robust against off-resonance effects due to the refocusing RF pulse (*Figure 2.6a*). In contrast, the same slice acquired with the GRE sequence shows a constant shift of fat tissue along the frequency encoding direction, which can be noticed by e.g. the dark band near the cheek (*Figure 2.6b*). Further, signal loss can be detected close to the esophagus (air-tissue boundary). In EPI the off-resonance effects results in a non-interpretable image being heavily distorted along the phase encoding direction. Fat signals are shifted by approximately half the image size and is superimposed by serious geometric deformations, signal loss and blurring.

The same artifacts can be also observed in the context of RF excitation. Here, the frequency displacement can cause bended slice-selections. Regarding multi-dimensional spatial excitations, the effects are similarly severe as in EPI or spiral imaging. Off-resonance based excitation artifacts are exemplary shown for a 2-D spiral pulse in *Figure 2.7*. Geometrical distortions, magnetization loss and blurring explicitly increase with rising off-resonance level and/or pulse durations and can additionally impair the image quality.

To provide reliable diagnostic imaging the consideration of off-resonance effects is crucial in both the excitation and acquisition phase. The next two chapters introduce strategies to explicitly correct off-resonance effects with tailored pTx RF pulses. *Chapter 3* covers the advanced off-resonance correction during 2-D slice-selective RF excitations. In contrast, the method in *Chapter 4* also utilizes the pTx technology to compensate for off-resonance related signal dephasing in GRE-based acquisition schemes.

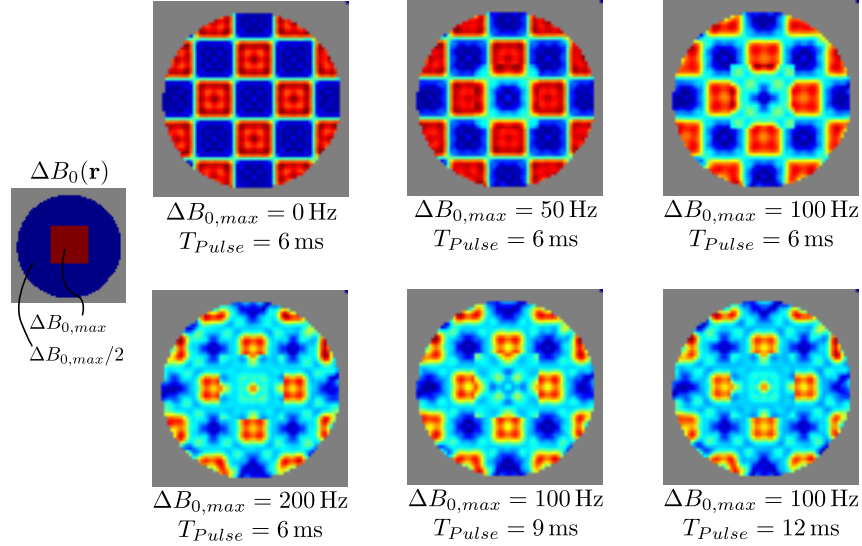


**Fig. 2.7:** Off-resonance effects in RF excitation. Numerical Bloch simulations were calculated for a 2-D spiral RF pulse exciting a checkerboard pattern at different off-resonance magnitude levels and RF pulse durations. Main field deviations  $\Delta B_0$  are imposed with a local square-shaped elevation. Either off-resonance magnitude level or RF pulse duration is systematically increased from 0 to 200 Hz or 6 to 12 ms, respectively.





## 2DRF Pulse Design for Reduced FOV Imaging with pTx

### 3.1 Enhanced Correction of Off-Resonance Effects in 2DRF-Pulse Design

This section contains methods & principles that were accepted for publication in:

R. Schneider, D. Ritter, J. Haueisen, and J. Pfeuffer. Novel 2drf optimization framework for spatially selective rf pulses incorporating b1, b0 and variable-density trajectory design. In *Proceedings of the 20th Annual Meeting of the ISMRM, Melbourne, Australia*, page 3454, 2012.

R. Schneider, D. Ritter, J. Haueisen, and J. Pfeuffer. Evaluation of 2drf echo-planar pulse designs for parallel transmission. In *Proceedings of the 20th Annual Meeting of the ISMRM, Melbourne, Australia*, page 3459, 2012.

R. Schneider, D. Ritter, J. Haueisen, and J. Pfeuffer. B0-informed variable density trajectory design for enhanced correction of off-resonance effects in parallel transmission. *Magn Reson Med*, 71:1381–1393, 2014. ISSN 1522-2594. doi: 10.1002/mrm.24780. URL <http://dx.doi.org/10.1002/mrm.24780>.

#### 3.1.1 Introduction

The application of spatially selective pulses in pTx is commonly used for reducing image acquisition time and mitigating prevailing  $B_1$  and  $B_0$  inhomogeneities. The majority of studies adopt the well-known spatial domain design approach [4, 15]. This approach allows the incorporation of the prevailing transmit coil sensitivity and off-resonance information for the subsequent optimization of a proper RF pulse (Section 2.2.3).

Spatially two-dimensional selective pulses based on concatenated RF sinc pulses played along a rectilinear, i.e. echo-planar, trajectory (EP-2DRF) are reported in human applications [45, 46, 120–122]. However, upon closer investigation and optimization only a partial correction of the geometric distortions caused by evolved phase errors along the slow direction was observed. The severity of these phase errors is directly linked to the off-resonance magnitude and is pronounced with long RF pulse durations. A similar sensitivity to off-resonance has also been denoted for three-dimensional spokes excitation pulses, i.e. fast- $k_z$  and echo-volumar pulses [60, 62, 123]. The reason for their limited off-resonance

compensation seems to be their limited capability to make use of the full transverse-plane  $B_0$  inhomogeneity information. For example, the spokes of the transmit trajectory of an 2-D spatially selective RF pulses based on a echo-planar trajectory (EP-2DRF) pulse are spanned along the slice selective and perpendicular to the phase encoding direction. Subsequently the trajectory offers only one dimension to tackle the two dimensional transverse-plane off-resonance information.

Recently, it has been shown that the actual k-space trajectory or spokes positions have a great impact on the excitation performance and should also be optimized in dependence of the prevailing  $B_1/B_0$  maps setting [60, 62, 64, 123–126]. However, only few of the spokes related reports consider off-resonance in the context of parallel transmission [60, 62, 123]. To date, all of these methods determine optimized k-space locations partially or solely on the basis of iterative greedy or high dimensional optimization algorithms, which can be computationally intensive for large parameter sets. Consequently, their application has been limited to spokes based trajectories [60, 62, 123–125] or other low parameter trajectory representations [64, 126]. Yet, their effect was not analyzed on finely sampled pulses like spiral pulses. Furthermore, most reports do not take into account the SAR nor the RF power levels as an implicit indicator [64, 123–126].

In this study, an empirical approach on the basis of a novel k-space trajectory design is introduced to further address the geometric distortion correction in presence of strong off-resonance. In contrast to previous k-space trajectory optimization algorithms [62, 124] the k-space locations are determined non-iteratively from the  $B_0$  fieldmap via an analytically computed metric representing the effective k-space density distribution. Thus, the approach can be used in a straightforward manner for low and high parametric RF pulses, as it does not require any additional computations. The method is applied to EP-2DRF pulses as an often-used representative of spoke trajectory based pulses. This approach is shown to offer enhanced inhomogeneity mitigation, whereas it reduces the RF power levels in parallel transmission. Preliminary work has been presented previously [23, 24].

Furthermore, the definition of the target magnetization pattern in dependence of the actual physical excitation resolution of the k-space trajectory is discussed. To our knowledge the majority of studies used an identical spatial resolution for the spatial grid and actual transmit k-space trajectory [4, 15, 17, 124]. However, in practical workflows the grid resolution is often different and possibly higher than that of the RF pulse. In this case, an appropriate spatial adjustment of the target pattern is required. The benefits of this circumstance have not been demonstrated so far, but it proves to be very important in practical pulse design for better utilization of the available degrees of freedom (DoF) in the pulse optimization process.

All proposed methods are implemented for the widely used slice-selective EP-2DRF pulses. The general benefit of additional RF transmit channels, i.e. higher DoF, on the  $B_1$  and  $B_0$  inhomogeneity compensation is assessed in comparison to the single channel circular polarized (CP) mode. The proposed methods are systematically analyzed in a simulation study demonstrating the achievable gain in excitation quality and reduction of RF power deposition. Finally, human in-vivo experiments were performed to validate the proposed trajectory design for EP-2DRF pulses.

### 3.1.2 Theory

#### *EP-2DRF Pulse Extension of the Spatial Domain Design Approach*

The EP-2DRF pulse optimization framework is based on the well known spatial domain design approach [4, 15], which exploits the linearity of the low flip angle regime. The final equation poses an inverse problem looking for proper RF waveforms  $\mathbf{b}_{full}$  for an arbitrary number of RF channels in order to minimize the distance to a desired magnetization pattern  $\mathbf{m}_{des}$  defined in a region of interest  $\mathbf{W}$ :

$$\hat{\mathbf{b}}_{full} = \arg \min_{\mathbf{b}_{full}} \{ \|\mathbf{A}_{full} \mathbf{b}_{full} - \mathbf{m}_{des}\|_{\mathbf{W}}^2 + R(\mathbf{b}_{full}) \}, \quad (3.1)$$

where  $\mathbf{A}_{full}$  denotes the overall system matrix and  $R(\mathbf{b}_{full})$  represents a regularization term, e.g. Tikhonov regularization for damping the RF power.  $\mathbf{A}_{full}$  is further defined as:

$$\begin{aligned} \mathbf{A}_{full} &= [\tilde{\mathbf{S}}_1 \mathbf{A} \cdots \tilde{\mathbf{S}}_C \mathbf{A}] \quad \text{with} \\ \tilde{\mathbf{S}}_c &= \text{diag} \{ S_c(\mathbf{r}) \} \quad \text{and} \\ a_{ij} &= i\gamma M_0 \Delta t e^{i(\mathbf{r}_i \mathbf{k}(t_j) + \gamma \Delta B_0(\mathbf{r}_i)(t_j - T_{pulse}))}, \end{aligned} \quad (3.2)$$

that is the concatenation of the system matrix  $\mathbf{A}$  and diagonal matrices  $\tilde{\mathbf{S}}_c$ , which hold information about the RF coil sensitivity profiles  $S_c$  for all RF channels  $C$ . The system matrix  $\mathbf{A}$  incorporates the used excitation k-space trajectory  $\mathbf{k}$  at given spatial ( $\mathbf{r}$ ) and temporal ( $t$ ) properties discretized with  $N_s$  and  $N_t$  samples. Main field inhomogeneities  $\Delta B_0$ , which lead to off-resonances are considered within the total RF pulse duration  $T_{pulse}$ .

Spatially selective pulses enabling reduced field of view (rFOV) imaging can be analytically calculated via EP-2DRF pulses with a rectilinear trajectory according to the low flip angle theory, which results in a sinc-shaped amplitude modulation of the concatenated sinc-shaped RF subpulses (spokes) in the fast direction [42, 46].

In order to optimize such EP-2DRF pulses regarding  $B_1$  and  $B_0$  inhomogeneity mitigation the approach (*Equation 3.1*) can be customized: In order to preserve a defined slice selectivity of the EP-2DRF pulse, the basic shape  $\mathbf{p}$  of the single spokes (RF sinc subpulses) along the fast direction is fixed during RF pulse optimization. For that purpose, a complex optimization weight  $w$  for each single spoke is introduced, that commonly scales all RF samples  $N_p$  of  $\mathbf{p}$ , respectively.

$$\mathbf{b}_{full}(t_j) = w_k \mathbf{p}(t_{j \bmod N_p}) \quad \text{with } t_j = 1 \dots CN_t \text{ and } k = \lceil t_j / N_p \rceil \quad (3.3)$$

In other words, solely the pulse weights of the single RF sinc subpulses are adapted allowing an optimization along the phase encoding excitation direction. Consequently, for an EP-2DRF pulse made up by  $N_{spoke}$  spokes, the solution vector  $\mathbf{b}_{full}$  contains  $CN_t/N_p = CN_{spoke}$  optimization weights (*Equation 3.3*). Furthermore, the information of the basic shape  $\mathbf{p}$  of each single spoke has to be transferred from the solution vector  $\mathbf{b}_{full}$  to the matrix  $\mathbf{A}_{full}$ :

$$a'_{ik} = \sum_{j=(k-1)N_p+1}^{kN_p} a_{ij} \mathbf{p}(j \bmod N_p) \text{ with } k = 1 \dots CN_{spoke}. \quad (3.4)$$

Thus, the resulting one dimensional optimization problem along the phase encoding direction is compressed by factor  $N_p$ : The modified inverse problem is now built on the compressed system matrix  $\mathbf{A}'_{full}$  with dimensions  $N_s \times CN_{spoke}$ . Whereas the solution vector  $\mathbf{b}_{full}$  is mainly composed of the optimization weights for the respective spokes. Clearly, the preservation of the RF shape per spoke comes along with a restriction of the available degrees of freedom. In particular, the optimization is limited to a rather non-continuous, section-wise manner.

#### *Accurate Definition of the Target Magnetization Pattern*

In a practical pTx oriented workflow,  $B_1$  and  $B_0$  maps are acquired once and build the basis for subsequent RF pulse designs. Typically, they are resampled to the same spatial resolution, which is also the spatial discretization of the desired target magnetization pattern  $\mathbf{m}_{des}$  within the pulse optimization framework, i.e. the grid resolution  $G_{res} = FOV/N_s$ . Though, the TX k-space trajectory is defined independently from the grid and may require an adaption of the target pattern to its physical characteristics. In particular, the transmit k-space trajectory is traversing the k-space to a maximal extent, i.e.  $\pm k_{max}/2$ . Thus, the effective excitation resolution  $TX_{res}$  is also physically limited to that spatial resolution. However, the commonly used conjugate gradient (CG) algorithms [4, 15] to solve the linearized complex system in Equation 3.1 are not considering this limitation: They deterministically reduce the squared error to the defined target pattern. Consequently, in the frequent case that the spatial resolution of the grid exceeds the physically set constraints ( $G_{res} > TX_{res}$ ), the solver algorithms are likely to spend available DoF for attaining the physically impossible sharp magnetization transitions. Here, the pattern has to be adjusted to the maximum possible excitation resolution by e.g. spatial low-pass filtering: The appropriate kernel size  $h$  of a spatial average box filter is defined by the next odd value of the ratio  $h = TX_{res}/G_{res} = N_s/(k_{max}FOV)$ .

#### *$B_0$ Map Driven Variable Density Trajectory Design*

The k-space trajectory design proposed in the following aims at improving off-resonance compensation by sub-sampling k-space regions with potentially high accrued phase errors coupled to the target pattern. In the presence of main field inhomogeneities  $\Delta B_0$  the accrued phase error in k-space  $\Phi_{error}$  can be estimated via the two dimensional Fourier transform of the absolute spatial phase error in image domain over time  $t$ :

$$\Phi_{error}(\mathbf{k}) = \left| \int e^{i\gamma\Delta B_0(\mathbf{r})t} e^{-i\mathbf{k}\mathbf{r}} d\mathbf{r} \right|. \quad (3.5)$$

Hence, this metric represents  $\Delta B_0$  artifacts in k-space. To specify the accrued phase error towards the target magnetization pattern, it is weighted with the absolute k-space representation of the target pattern function  $\mathbf{m}_{des}$ . The result is denoted as the weighted B0 error metric  $\Phi_{w,error}$ :

$$\Phi_{w,error}(\mathbf{k}) = \Phi_{error}(\mathbf{k}) \left| \int (\mathbf{m}_{des} - \bar{\mathbf{m}}_{des}) e^{-i\mathbf{k}\mathbf{r}} d\mathbf{r} \right|. \quad (3.6)$$

In the proposed method, the impact of the accrued phase error at k-space center is neglected by zero mean normalization of  $\mathbf{m}_{des}$ . The  $\Delta B_0$  artifact at k-space center is equivalent to a constant shift in the spatial domain. This can be easily compensated analytically by applying the corresponding conjugate constant phase term to the RF pulse phase. Therefore, the mean phase error is not considered as problematic and is excluded from the metric.

The effective k-space density  $\rho$ , which is finally the basis for the final k-space locations to be sampled by the trajectory, is defined by:

$$\rho(\mathbf{k}) = (1 - \epsilon \frac{\Phi_{w,error}(\mathbf{k})}{\max(\Phi_{w,error})}) + 2\alpha/k_{max} \cdot \|\mathbf{k}\| \quad \text{with } 0 \leq \epsilon \leq 1. \quad (3.7)$$

In principle,  $\rho$  is determined by two parts: First, by the omission of k-space locations with potential phase errors. This is achieved by subtracting the normalized  $B_0$  error metric  $\Phi_{w,error}$  from an uniform distribution. The uniform distribution basically represents the default equal-density (ED) k-space sampling scheme and can be expressed with the constant density value 'one' over all k-space locations (*Equation 3.7*). By the use of the weighting factor  $\epsilon$  the impact of  $\Phi_{w,error}$  can be further controlled from minimal ( $\epsilon = 0$ ) to maximal ( $\epsilon = 1$ ) influence. Note that the density at k-space center is always set to  $\rho(\mathbf{0}) = 1$  due to the initial discard of the mean phase error. Thus, an adequate sampling near and at the k-space center is provided.

The second part is a linear balancing gradient with slope  $\alpha$  and is based on empirical observations: From our experience the severity of the phase errors at lower spatial frequencies is higher than those of higher spatial frequencies. This is quite intuitive as the main contribution to the final excitation result is determined by lower frequencies. Consequently, the impact of the artifact at those k-space locations is also more prominent. This observation is approximately counterbalanced by the linear balancing gradient. Here the slope  $\alpha$  is directly proportional to the ratio of low frequency versus high frequency  $\Delta B_0$  artifact severity and its degree of sub-sampling. Hence, for  $\alpha > 0$  lower spatial frequency phase errors get further sub-sampled.

Finally, to compute the discrete k-space locations from the k-space density  $\rho$  an adapted density weighting approach similar to Ref. [127] is used. For this purpose, the resulting density  $\rho$  is normalized to keep the number of k-space sampling points constant. A simplified schematic of the variable density trajectory computation process is depicted in *Figure 3.1*.

When analyzing the proposed variable density sampling scheme for each  $t_j$  of  $T_{pulse}$  the center of mass of  $\Phi_{error}$  is typically located at lower spatial frequencies, which get consequently strongly sub-sampled according to the resulting  $\rho$ . Though, these locations are generally critical to sub-sample as the RF power expense is likely to increase. As a tradeoff,  $\Phi_{error}$  is restricted merely to its extreme case, i.e. the maximal phase error over the total RF pulse time  $t = T_{pulse}$ , rather than considering an evolved phase error for each  $t_j$ .

### 3.1.3 Methods

The input data of the simulations were acquired on a 3 T MAGNETOM Skyra system equipped with two independent and integrated pTx channels (Siemens AG, Healthcare Sector, Erlangen, Germany).  $B_1$  and  $B_0$  information were obtained with presaturation TurboFLASH

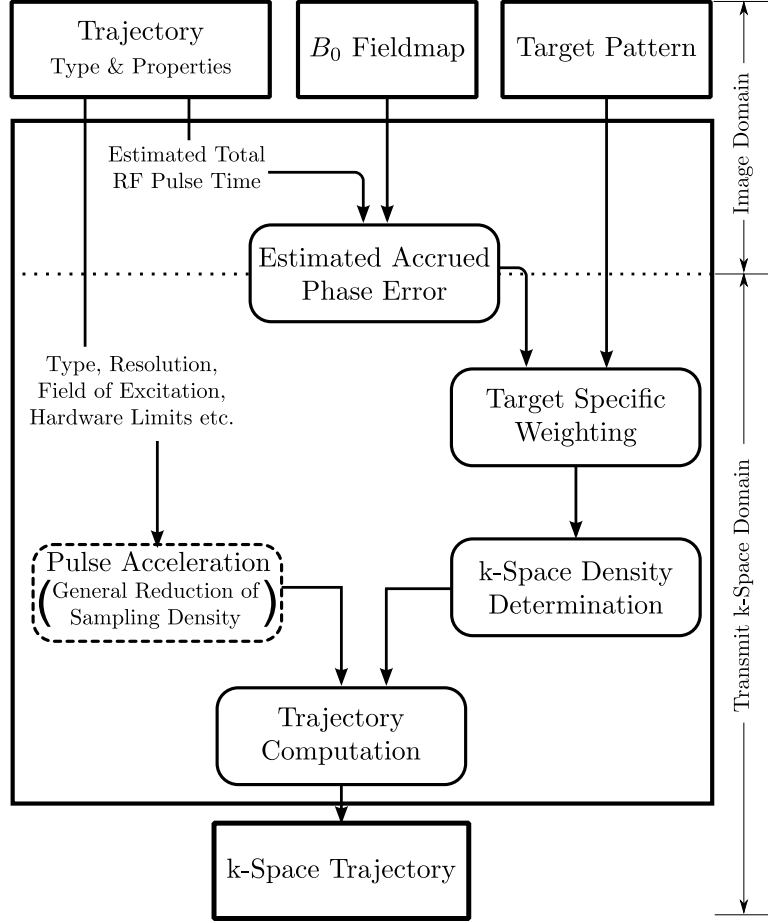


**Fig. 3.1:** Diagram showing the basic steps and procedure of the  $B_0$  fieldmap driven variable density trajectory approach.

[99] and a dual echo time gradient-echo approach, respectively. Fieldmaps were additionally smoothed before pulse design via the regularized weighted least-squares method proposed in [102]. RF pulses were calculated with a conjugate gradient algorithm in MATLAB 7.11 (MathWorks Inc. Natick, MA, USA). Note that no regularization was used in order to exclude further optimization effects like the damping of RF power via Tikhonov regularization. The EP-2DRF pulse design followed the extension described above with  $\mathbf{p}$  being an RF sinc pulse and uses a two-dimensional bar target pattern representing the slice-selective rFOV. The target flip angle was set to  $15^\circ$ . All optimizations were done on the basis of a regular trajectory design, i.e. equal-density (ED), and a variable-density (VD) k-space trajectory design according to our proposed method integrating the respective  $B_0$  fieldmap information. Multichannel optimized RF pulses (2-ch pTx) and the corresponding single RF channel pulses in circular-polarized mode (1-ch CP) were calculated. Thereby, the benefit of additional degrees of freedom of an additional transmit channel was analyzed. Furthermore, respective analytically computed pulses in the small tip-angle approximation (STA) as described in [46] were determined as a reference to demonstrate the limited off-resonance compensation ability

of the optimization process towards EP-2DRF pulses. To provide a reasonable comparison, all basic RF pulse specifications (e.g.  $k_{max}$ , total RF pulse duration, number of spokes) were kept constant independent from the number of RF channels, trajectory design or RF optimization.

Bloch equation simulations were performed for all pulses using a  $64 \times 64$  grid to predict the magnetization result. The simulations incorporated the  $B_0$  and  $B_1$  maps information and thus, the prevailing off-resonances and spatial variation of the  $B_1$  excitation field. Deviations from the target pattern were assessed via the root mean square error (RMSE) of the magnitudes within the region of interest  $\mathbf{W}$ :

$$RMSE = \sqrt{\left\| |\mathbf{A}_{full} \hat{\mathbf{b}}_{full}| - \mathbf{m}_{des} \right\|_{\mathbf{W}}^2}. \quad (3.8)$$

In order to get an estimate of the global SAR performance of the proposed methods, the effective RF pulse power ( $50 \Omega$  terminator) was noted. The RF power values were quoted relative to those of the corresponding optimized 1-ch CP EP-2DRF pulse with an ED k-space trajectory:

$$RF_{power} = \frac{U_{eff}^2}{R} = \left( \frac{\|\hat{\mathbf{b}}_{full}\|}{\sqrt{CN_t}} \right)^2 \cdot \frac{1}{50 \Omega} = \frac{\|\hat{\mathbf{b}}_{full}\|^2}{CN_t \cdot 50 \Omega}. \quad (3.9)$$

#### *Simulation I: Accurate Target Magnetization Definition*

Our aim was to demonstrate the RF pulse optimization effects of target magnetization patterns adjusted (smoothed) and not adjusted to the trajectory specifications in case of  $G_{res} > TX_{res}$ . Simulations with an adapted target pattern were done with reference to a rectilinear EP with equally distributed k-space density.  $B_1$  maps were acquired in a spherical water phantom with 150 mm field of view (FOV),  $64 \times 64$  matrix size and  $G_{res} = 2.34$  mm. The  $B_0$  fieldmap information was excluded from optimization for better illustration (omitting geometric distortions). EP-2DRF pulses were designed with a rFOV of 30 mm, an excitation resolution  $TX_{res}$  of 12 mm and a stop band of 250 mm resulting in 25 EP lines and 17 ms pulse time. The kernel size  $h$  of the spatial average box filter was determined to match the desired excitation resolution on the spatial grid of the predefined target pattern. Particularly, for the EP-2DRF pulse  $h$  was set to  $64 \cdot 12 \text{ mm} / 150 \text{ mm} \approx 5$ .

#### *Simulation II: Enhanced Off-Resonance Correction*

Optimized EP-2DRF pulses with the proposed field map driven and regular trajectory design were compared at different off-resonance levels. For this purpose exemplary human axial brain  $B_1$  and  $B_0$  maps were acquired from a healthy subject (FOV 240 mm, matrix  $64 \times 64$ ). For the rectilinear trajectory design, the effective sampling density relies on a one dimensional quantity, i.e. the discrete spoke positions along the phase encoding direction. Thus, the  $B_0$  error metric was reduced to one dimension prior to trajectory computation: A maximum projection orthogonal to the phase encoding direction was done so that the k-lines can avoid the accrued phase error elevations. Elevations of the accrued phase error were subsampled with factor  $\epsilon = 0.9$  and balanced with slope  $\alpha = 1$  (Equation 3.7). In other words,

the accrued phase errors in k-space are sub-sampled up to 90% and the sub-sampling (or severity) ratio of low versus high spatial frequency artifacts is approximated with factor two ( $\rho(\mathbf{0})/\rho(\mathbf{k}_{max}/2) \approx 1/(\alpha + 1) = 1/2$ ). EP-2DRF pulses had a 36 mm rFOV, 7 mm resolution and 43 lines resulting in a RF pulse length of 28 ms. The maximum absolute off-resonance level was systematically increased from 10 Hz to 300 Hz by scaling the normalized  $B_0$  map in 10 Hz steps. The actual in-vivo case is the 70 Hz setting. Prior to pulse optimization, the target pattern was adapted to the given transmit k-space trajectories following the approach described above. Note that a 2-ch pTx and a 1-ch CP mode pulse were calculated separately for the described setting.

### *Simulation III: Pulse Acceleration*

The human data sets above were also used to analyze the impact of pulse acceleration on the general off-resonance correction performance. Here, different acceleration levels of the 2-ch pTx EP-2DRF pulse type were simulated at a fixed off-resonance level of 150 Hz. At each acceleration level the excitation performance of ED and variable-density (VD) trajectory design was noted, respectively. Acceleration was done by stepwise reducing the number of k-lines of the transmit trajectory with identical nominal excitation resolution. The performance of the non-accelerated 1-ch CP EP-2DRF with regular trajectory density was taken as a reference and rough estimate for a suitable acceleration factor. To point out differences and possible effects of off-resonance with pulse acceleration, the excitation performance was compared to the accelerated 2-ch pTx pulses with ED trajectory design in presence of no off-resonance, i.e. with a nulled  $B_0$  map. Note that the field of excitation did not fit to the actual FOV, but was designed with extended outer volume suppression. Therefore, aliasing is expected to occur with higher acceleration factors.

### *Experiments*

The excitation performance of the ED and VD EP-2DRF pulse designs were evaluated in human in-vivo experiments utilizing two pTx channels. Particularly, imaging was done at two distinctive anatomical brain regions, which are known to be prone to off-resonance effects: First, a pseudo-transverse oblique slice through the frontal brain region was acquired. Second, sagittal imaging near the c-spine was performed. For both cases, corresponding  $B_1$  and  $B_0$  maps were obtained with the methods stated above. The EP-2DRF pulses were designed with similar settings used in the simulation (36 mm rFOV, 7 mm TX resolution). In contrast to the simulation study, a flyback scheme was used in order to avoid side-lobes and transmit ghosts resulting in a prolonged total RF pulse length of 45 ms. Images were acquired using a single-shot gradient echo EPI sequence with FOV  $240 \times 240 \text{ mm}^2$ , matrix  $64 \times 64$ , TR 500 ms and TE 42 ms.

#### **3.1.4 Results**

##### *Simulation I*

Figure 3.2 shows the Bloch simulations with normalized flip angle distributions and relative RF power levels of RF pulse design with and without adaptation of the target magnetization



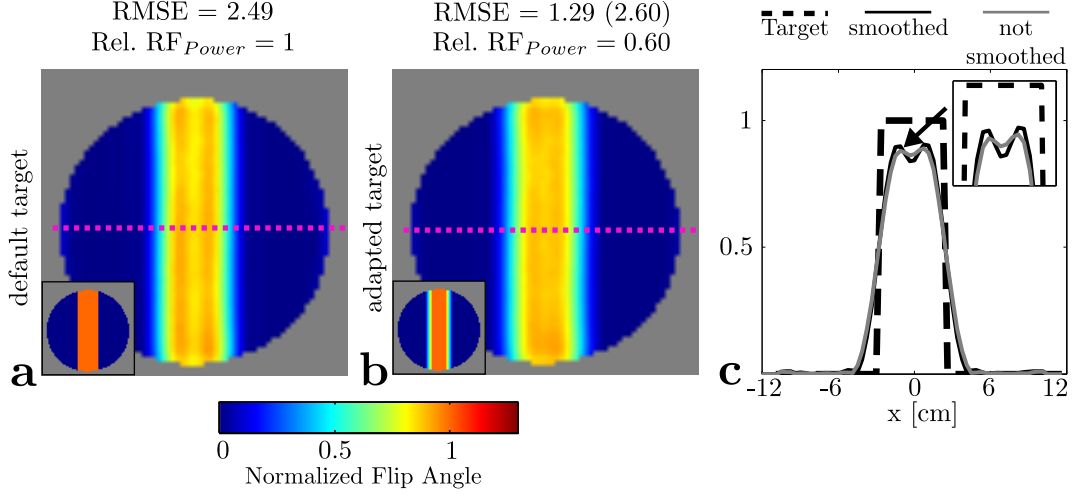


**Fig. 3.2:** RF pulse optimization **a** without and with **b** the target magnetization adapted to transmit k-space trajectory (target pattern is shown in the lower left corner). RMSE metrics of the latter case were stated relative to the smoothed and default (in brackets) target pattern. **c** 1-D profiles through the center of the Bloch simulations. The beneficial effect of the adapted target pattern is shown for a spoke trajectory based EP-2DRF pulse design. Despite the slightly lower spatial fidelity with respect to the default target pattern, improved homogeneity and less aliasing are visible while requiring significantly less RF power.

pattern. Note that the target adjustment is only necessary if  $G_{res} > TX_{res}$  applies. Possible off-resonance effects were excluded here for better illustration. The target pattern definition is shown as insert in the lower left corner, with the conventional target pattern definition in Figure 3.2a and with smoothed target pattern in Figure 3.2b. 1-D profiles of the respective Bloch simulations are depicted at Figure 3.2c. The smoothed magnetization transitions have been adjusted to the actual excitation resolution. The RF pulse design based on the adapted patterns reveals virtually improved inhomogeneity mitigation, i.e. 48% reduced RMSE (from 2.49 to 1.29) for the EP-2DRF design. In fact, the RMSE value calculated on the basis of the original unsmoothed target pattern reveals a slightly lower spatial fidelity (4% higher RMSE). However, noticeable improved inhomogeneity compensation can be located for example in the middle of the excitation bar (Figure 3.2c). The width of the actual transition band was not affected by the smoothing process. Furthermore, a significant RF power level reduction compared to the design with conventional target definition can be assessed. The EP-2DRF pulses required noteworthy 40% less RF power to achieve the desired magnetization.

### Simulation II

In this section the proposed  $B_0$  map driven VD trajectory design is compared to conventional ED trajectory design at different off-resonance levels and for single and multichannel transmit modes. Simulations were run on the basis of human axial brain data illustrated in Figure 3.3a. The  $B_1$  coil profiles, i.e. the  $B_1$  maps, of the dual channel (2-ch pTx) and single channel (1-ch CP) transmit modes show a significant spatial variation. The  $B_0$  fieldmap shows a prominent off-resonance increase at the frontal brain area.

In Figure 3.3b schematics of the transmit k-space trajectories are shown relative to the

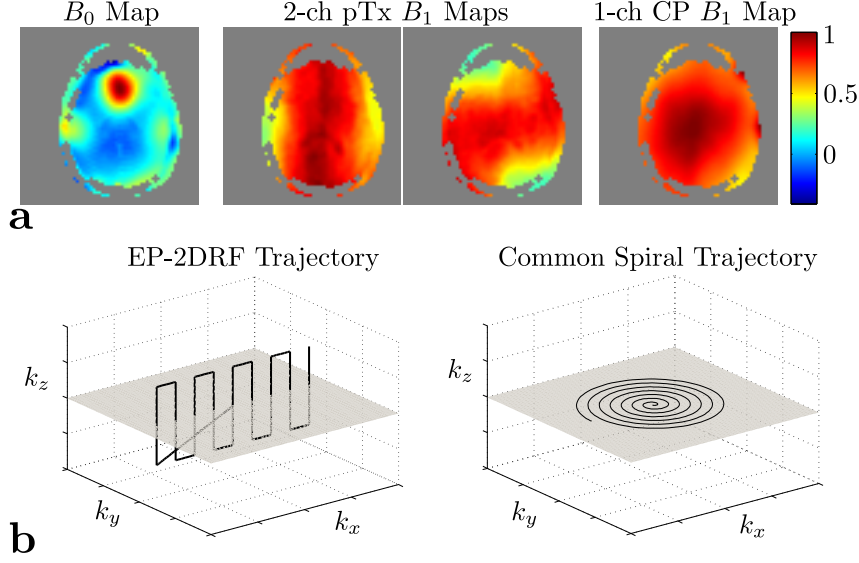


**Fig. 3.3:** **a** Normalized human axial brain  $B_0$  and  $B_1$  maps used in the simulation studies. **b** Schematic transmit k-space trajectories with the imaging plane colored in gray. *left* Rectilinear trajectory for a slice-selective EP-2DRF pulse with only one dimension in image plane. *right* A common spiral trajectory of a non-slice selective 2-D spiral pulse.

transverse imaging plane. The ability of the spoke trajectory based EP-2DRF pulse to fully exploit the transverse-plane  $B_0$  map information is limited to one dimension, i.e. the phase encoding (slow) direction  $k_x$ . In contrast, the conventional spiral pulse trajectory traverses the k-space in-plane in two dimensions, i.e.  $k_x$  and  $k_y$ , and thus offers potentially more degrees of freedom for rewinding a locally accrued phase error.

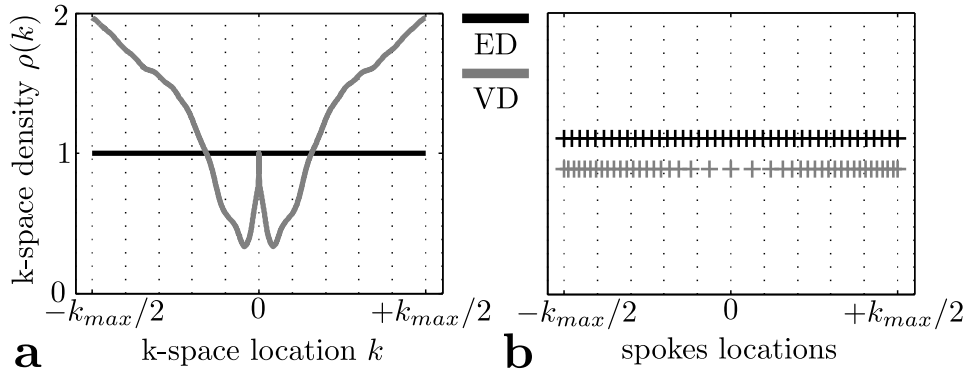


**Fig. 3.4:** Comparison of  $B_0$  map driven variable density (VD, gray) and regular equal density (ED, black) trajectory design for an maximum off-resonance level of 150 Hz. **a** k-space density function for the phase encoding direction. **b** According discrete spokes locations. The k-space density function of the VD indicates a less dense sampling of the lower and a denser sampling of the higher spatial frequencies.

k-space density functions of the proposed VD approach were calculated as described above for the spoke trajectory based EP-2DRF design (*Figure 3.4*). The VD design (gray line) is compared to the conventional ED design (black line). The k-space density functions  $\rho(\mathbf{k})$  were determined at an off-resonance level of 150 Hz (*Figure 3.4a*) and were reduced to one dimension prior to the computation of the trajectory. The latter was achieved by projecting the maximum values of the k-space density distribution onto the k-space phase encoding direction along  $-k_{max}/2 \dots +k_{max}/2$  for the spoke positioning. The resulting effective discrete spoke positions along the k-space phase encoding direction reflect the predefined density distribution (bottom row of *Figure 3.4b*). The k-space density function reveals a less dense sampling of the lower spatial frequencies, i.e. the estimated accrued phase error elevations are mainly localized at lower spatial frequencies of the k-space.

To analyze the VD sampling scheme in more detail, different VD designs were pursued for the EP-2DRF pulse with respect to the two separate components of  $\rho(\mathbf{k})$  (*Figure 3.5*), i.e. the weighted phase error  $\Phi_{w,error}$  and the balancing gradient (see *Equation 3.7*). It can be observed, that both components reduce RMSE compared to the ED sampling, but with increased RF power demands (*Figure 3.5a* versus *3.5b* and *3.5d*). The VD trajectory solely based on  $\Phi_{w,error}$  results in better off-resonance compensation and a moderate RF power increase compared to the pure balancing gradient VD design. The combination of both superimpose to the proposed superior VD design with notably reduced RF power deposition (*Figure 3.5d*).

The simulation results are shown in *Figure 3.6* representing the overall excitation error and required RF power in dependence of the prevailing off-resonance magnitude. The RF power levels of the optimized pulses were noted in relation to the corresponding 1-ch CP pulse (dashed lines). Explicit Bloch simulations of the 2-ch pTx mode excitation results at off-resonance levels 50, 150 and 300 Hz are further depicted in *Figure 3.7*.

For the EP-2DRF pulses with conventional ED trajectory design, the RMSE values rise quite linearly from 0.75 to 4.2 in single channel (1-ch CP, black dotted line) and from 0.63 to 4.0 in dual channel (2-ch pTx, black solid line) transmit mode with rising off-resonance level. This trend is also reflected by the Bloch simulations in *Figure 3.7* (second column) showing the increasing residual geometric distortions and signal losses. Especially within the off-resonance elevation in the frontal lobe area (see *Figure 3.3a*) a severe magnetization degradation and target pattern deformation can be observed. Compared to the analytically calculated STA EP-2DRF pulses, the optimized EP-2DRF pulses with ED trajectory design seem to tackle the geometric distortions only slightly (*Figure 3.7*, left two columns). On the other hand, the optimization process generally adjusts the magnetization intensity, i.e. compensates  $B_1$  inhomogeneities. Concerning the number of transmit channels, ED trajectory pulses designed in 2-ch pTx mode exhibit a moderately enhanced, but constant lower excitation error ( $\approx 0.17$  less RMSE) than the according 1-ch CP pulses (*Figure 3.6*). However, the usage of the additional transmit channel comes along with generally higher and quite varying RF power requirements: The 2-ch pTx pulses with ED trajectory reveal significantly increased RF power levels and several quite arbitrary RF power peaks with up to 5.5 times higher power demands (see black solid line versus black dotted line at 40 Hz).

Compared to the ED design, EP-2DRF pulses based on the proposed VD trajectory design (gray color) show superior results: Though, the excitation accuracy still decreases with increasing off-resonance similar to the ED design, the proposed VD trajectory approach offers considerably improved excitation accuracy (*Figure 3.6*). Beyond off-resonance levels of 20 Hz, RMSE values get well reduced by additional 43% (e.g. 1.87 RMSE versus 3.27 RMSE for 2-ch pTx at 190 Hz). The corresponding Bloch simulations (*Figure 3.7*, third column)

---

**EP-2DRF: 2-ch pTx VD @ 150 Hz**


---

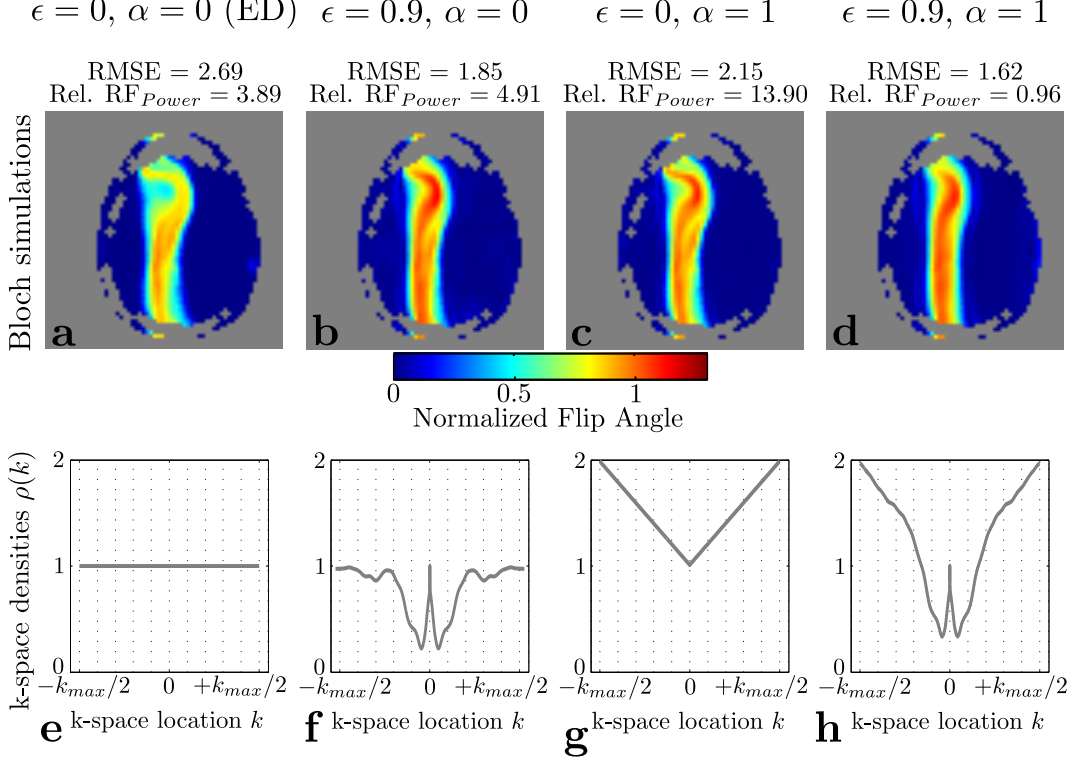


**Fig. 3.5:** **a-d** Bloch simulations of multi-transmit mode (2-ch pTx) EP-2DRF pulses with different variable density trajectory designs (VD, see *Equation 3.7*). **e-h** Corresponding k-space density sampling functions  $\rho$ . Simulations were done at off-resonance magnitude level of 150 Hz. Note that in each case all RF design parameters (e.g. number of lines and  $k_{max}$ ) were kept constant except for spokes distribution along the slow direction. **a, e** VD design neither influenced by balancing gradient ( $\alpha = 0$ ) nor by weighted  $B_0$  error metric  $\Phi_{w,error}$  ( $\epsilon = 0$ ), i.e. default ED design. **b, f** VD design solely determined by  $\Phi_{w,error}$  ( $\epsilon = 0.9, \alpha = 0$ ). **c, g** VD design solely based on the balancing gradient ( $\epsilon = 0, \alpha = 1$ ). **d, h** Default VD design combining both components ( $\epsilon = 0.9, \alpha = 1$ ). Both components clearly reduce RMSE compared to the ED design. Their combination exhibits a superior result with best spatial fidelity, but also with significant RF power reduction.

reveal that next to  $B_1$  inhomogeneities, also  $B_0$  inhomogeneities, i.e. geometric distortions, were clearly mitigated by the VD pulses compared to the STA pulse design. While offering enhanced off-resonance correction, the VD trajectory approach requires randomly higher and lower RF power than the ED design in 1-ch CP mode (gray dotted line). But it provides quite permanently lower power levels within 2-ch pTx mode (gray solid line), e.g. up to 79% less RF power at 90 Hz. Hence, the proposed  $B_0$  fieldmap driven variable density trajectory approach offers a gain in excitation performance, while reducing the RF power demand in parallel transmit mode.

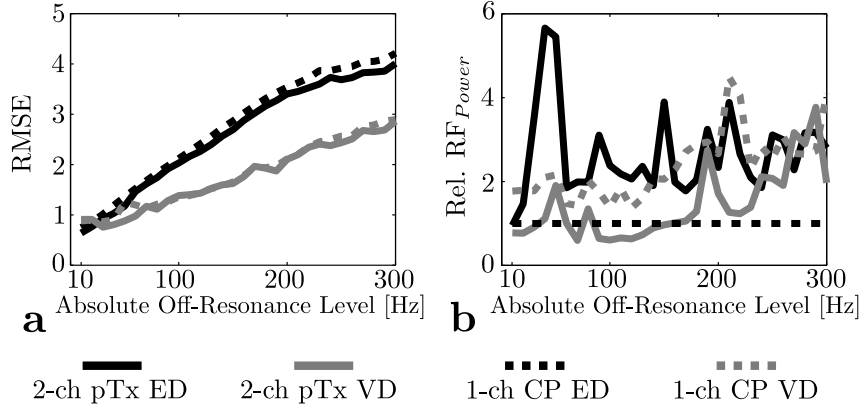


**Fig. 3.6:** Excitation performance analysis at different off-resonance magnitude levels based on human axial brain  $B_1$  and  $B_0$  maps. EP-2DRF designed with equal (ED, black) and the proposed fieldmap driven variable density (VD, gray) k-space trajectory design. Different calculations for two channel multitransmit (2-ch pTx, solid line) and circular polarized single channel mode (1-ch CP, dashed line). **a** RMSE as a function of peak off-resonance level. **b** Corresponding RF power levels. Note that RF power levels are normalized to the corresponding 1-ch CP pulse with ED trajectory. Compared to ED trajectory based pulses, the proposed VD trajectory approach offers persistently enhanced excitation performance for both RF pulse types. This is in line with partially higher RF power levels in 1-ch CP mode, but with constantly lower levels in 2-ch pTx mode.

### Simulation III

Within this section the ED and VD trajectory design were analyzed with respect to pulse acceleration for a fixed off-resonance level of 150 Hz. For comparison the ED trajectory based pulses were also calculated with no off-resonance. EP-2DRF pulses were stepwise accelerated up to three-fold (Figure 3.8), i.e. up to 66% of the spoke trajectory lines were omitted at maximum acceleration.

Different observations were made for the spokes trajectory based pulses: First, with no off-resonance (dash-dotted lines) the excitation accuracy is approximately maintained until 2.5 fold acceleration, but at rising RF power levels. Beyond this acceleration factor, the RMSE shows a steep increase because of severe aliasing effects (note again that pulses have an extended field of excitation). Second, in the presence of off-resonance the initial RMSE level is about 4 times higher within ED trajectory design (solid black lines) due to residual geometric distortions. Then the RMSE level diminishes with shorter pulse durations, i.e. less off-resonance impact, until aliasing effects become again the limiting factor. Further, the general RF power level, but also its slope with increasing acceleration is up to 4.5 times higher compared to the non off-resonance situation.

In contrast, the VD trajectory design based EP-2DRF pulses show a different trend (solid gray lines). As lower spatial frequencies are mainly less sampled (see Figure 3.4), aliasing is consequently quite noisy and gets worse with less available spokes. Hence, the low RMSE at low acceleration (enhanced excitation accuracy) is steadily increasing with increasing acceleration factors and becomes worse than ED EP-2DRF pulses beyond 1.4 fold acceleration. On the other hand, the RF power values are approximately constant with acceleration and

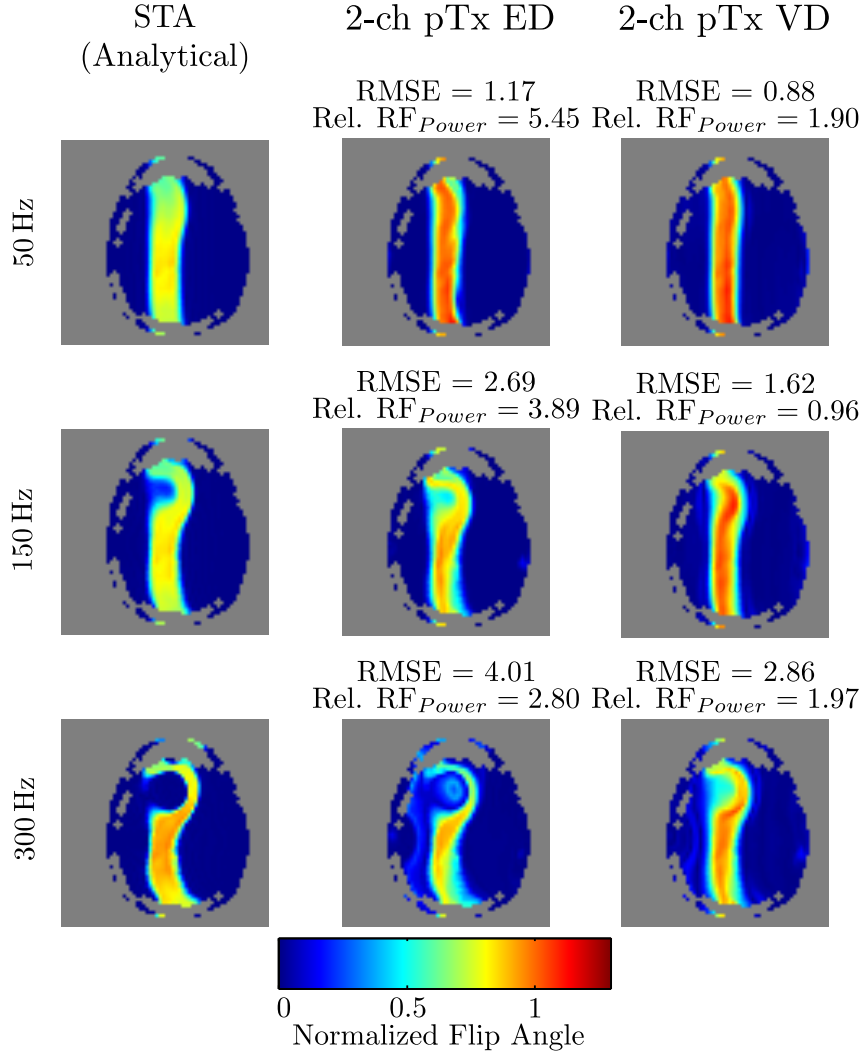


**Fig. 3.7:** Bloch simulations of multi-transmit mode (2-ch pTx) pulses at off-resonance magnitude levels of 50, 150 and 300 Hz. Optimized slice selective EP-2DRF pulses clearly improve  $B_1$  inhomogeneity mitigation compared to analytically computed STA pulses, but still lack in complete off-resonance correction resulting in residual geometric distortions. The proposed variable density trajectory design (VD) improves the situation up to 43% while reducing the RF power level at the same time.

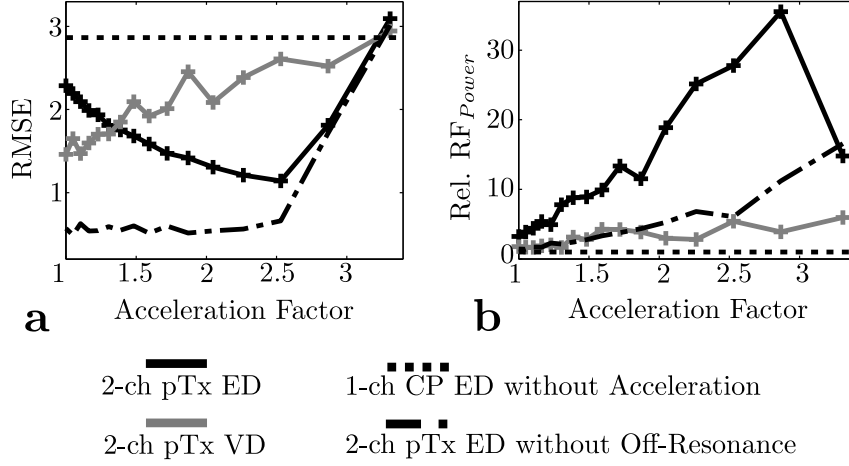


**Fig. 3.8:** Pulse acceleration at an off-resonance level of 150 Hz for EP-2DRF pulses. Multi-channel transmit pulses (2-ch pTx) were accelerated up to factor 3.3 with equal density (ED, black) and  $B_0$  map driven variable density (VD, gray) trajectory design. Same simulations for ED design pulses were done without off-resonance in order to highlight its influence on acceleration (black, dash-dotted line). As a performance reference the result of the non-accelerated 1-ch CP ED is indicated (black, dotted line). **a** RMSE performance as a function of TX acceleration factors. **b** Corresponding RF power metrics. Up to 1.4 fold acceleration the VD design offers enhanced excitation performance with reduced RF power deposition. Beyond, the method is still beneficial for low RF power design.

are up to 9 times lower than those of the ED design. Beyond 1.8 fold acceleration the RF power values are even below the level of those pulses without off-resonance. Compared to the results of the regular 1-ch CP ED pulse, all 2-ch pTx pulses can be accelerated by a factor 3 with better RMSE values, and always significantly enhanced RF power.

### Experiments

Figure 3.9 shows the excitation results of the different EP-2DRF designs for two different anatomic locations (Figure 3.9a,c). In both cases, the Bloch simulations agree well with the corresponding experiments (Figure 3.9b,d: bottom versus top row) and depict prominent geometric distortions due to off-resonance for the analytical STA design. The numerically optimized 2-ch pTx pulses (ED and VD) outperform the STA RF pulses regarding the spatial fidelity. But similar to the observations of the simulation study, the EP-2DRF pulses based on ED trajectory design mainly tend to compensate  $B_1$  inhomogeneity. With respect to off-resonance compensation, only the overall shift is basically corrected by the ED approach, but leaves the more complex geometric distortions. In contrast, the proposed VD method successfully tackles these complex geometric distortions offering an additional gain in excitation accuracy (additional 15% and 35% less RMSE). Furthermore, the required RF power level is also remarkably reduced, i.e. 12% and 53% less RF power relative to the ED pulses.

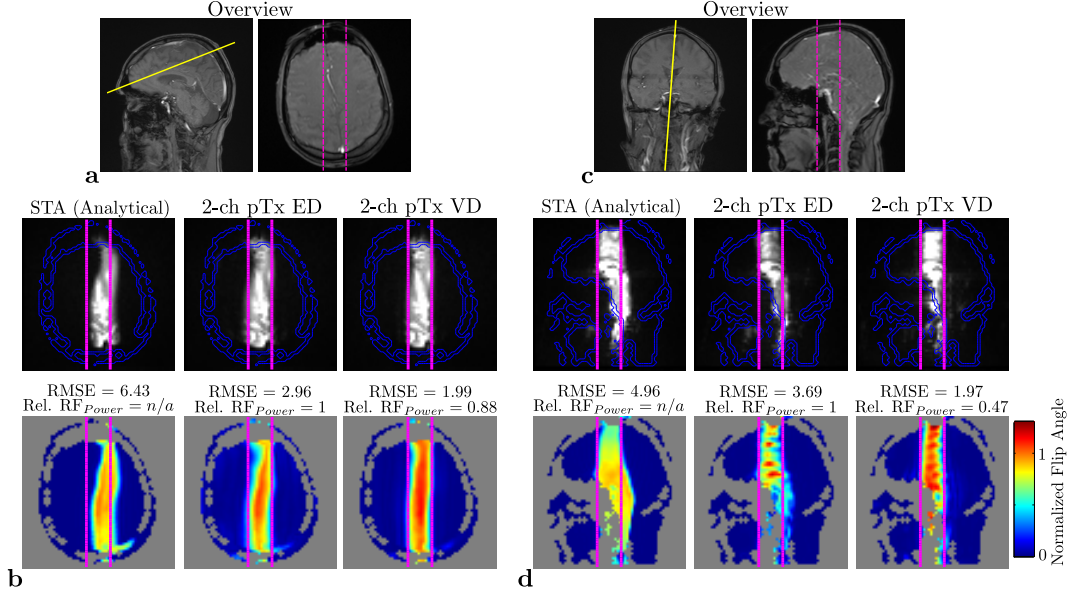


**Fig. 3.9:** Human in-vivo experimental results. **a,c** Overview of slice position (yellow line) and target pattern (magenta) **a** through frontal brain area and **c** near c-spine. **b,d** Corresponding experimental results (top row with subject contours in blue) and numerical Bloch simulations (bottom row) for analytical (STA), numerical optimized ED and VD 2-ch pTx EP-2DRF designs. In contrast to the other designs, the VD approach shows an enhanced compensation of geometric distortions, while lowering the RF power demands.

### 3.1.5 Discussion

In this study, the accurate definition of the target magnetization pattern was discussed to ensure the efficient usage of the available degrees of freedom during RF pulse optimization. Furthermore, a novel variable density trajectory design approach to enhance off-resonance correction in parallel RF pulse design was proposed and implemented. The possible benefits in excitation accuracy and RF power reduction of the introduced methods were demonstrated in a simulation study based on measured human data at 3 T. Based on the well known spatial domain design approach, rectilinear spoke trajectory based RF pulses (EP-2DRF) were determined without any regularization techniques for e.g. RF power damping in order to exclude an interference of different optimization effects. Finally, human in-vivo experiments were presented confirming the beneficial effects of the new EP-2DRF design.

The consideration of the transmit (TX) trajectory characteristics within the target pattern definition has been not reported so far [4, 15, 17, 124]. It was observed that the solving algorithm generally tries to minimize the distance to the predefined target pattern and does not take the maximum possible excitation resolution into account. Therefore, degrees of freedom are likely be squandered for the optimization towards physically impossible sharp magnetization transitions, if the actual grid resolution exceeds the physical TX k-space trajectory resolution. A target pattern adaptation was suggested, which considers the actual physical excitation properties. Bloch simulations revealed that with the target adjustment the approximation of the solution, but also the RF power efficiency are significantly improved (Figure 3.2). However, the RMSE calculations based on the original unsmoothed target



pattern definition show a slight reduction of the spatial accuracy. In spite of this discrepancy, a visible gain in inhomogeneity mitigation could be still assessed (*Figure 3.2c*). Ringing artifacts are explicitly reduced as the smoothed target pattern (image domain) results also in an appropriate apodization in k-space according to the TX resolution. Further it is important to point out the difference to an anti-ringing filter, which is applied to the RF pulse after the optimization process. In contrast to the spatial target smoothing, an anti-ringing filter would firstly not address the described optimization problem. Secondly, it might considerably decrease the excitation accuracy by reshaping the RF pulse forms or weights. The described approach is easily applicable to all types of spatial selective pulses as it relies on simple spatial low-pass filtering. Besides the used spatial averaging box filter, other spatial low-pass filters, for example with a Gaussian kernel, are also applicable.

In order to enhance off-resonance error correction in parallel pulse design, a variable density trajectory design which incorporates the actual  $B_0$  fieldmap information to calculate the modified k-space trajectory sampling density was introduced. Within this design, k space locations with potentially high accrued phase errors are determined and subsequently less sampled. In contrast to other methods, which jointly optimize the trajectory with the RF pulse [60, 62, 64, 123, 124] in a highly iterative manner, this approach is rather heuristic. Therefore it is likely that it does not offer the optimal k-space positions as the overall optimal solution involves certainly further unknown effects of importance. But on the other side, no additional computations and a constant gain in excitation performance come along with the method. The k-space trajectory is determined straightforward prior to RF pulse optimization, whereas the joint optimization approaches are based partially [62] or solely [60, 64, 123, 124] on iterative greedy algorithms. Here, the proposed trajectory design incorporates the estimated accrued phase error solely for the total RF pulse duration  $T_{pulse}$ . However, in a more sophisticated extension, for example a time-variant phase error could be used considering the evolved phase error, which could further improve performance. As shown in *Figure 3.5* the improved off-resonance behavior can be mainly attributed to the  $B_0$  map based phase error component (*Equation 3.7*). Though, the re-balancing of this density quantity by the linear density gradient helps remarkably to reduce the RF power level. The method was applied to spokes trajectory based RF pulses, which are known to be sensitive to their effective placement in k-space. The off-resonance correction performance of both pulse types was assessed as a function of the maximum off-resonance magnitude, different number of RF transmit channels and different pulse acceleration factors while taking the RF power level into account.

The proposed  $B_0$  map driven variable density (VD) trajectory design approach offers a significant additional gain in excitation accuracy from low to high off resonance magnitudes for multi-channel, but also for single channel RF pulses (*Figure 3.6*). EP-2DRF pulses was shown to benefit greatly from the new design: Simulations (*Figure 3.7*) and experiments (*Figure 3.9*) yielded that the optimization based on the conventional trajectory design with equally distributed (ED) spokes lack in off-resonance correction, which is likely due to their limited transverse plane encoding capability and rather non-continuous optimization. The optimization process mainly resolves  $B_1$  inhomogeneity mitigation, but poorly tackles the geometric distortions getting worse with higher off-resonance levels. In comparison, the VD method enables significantly less RMSE by enhanced  $B_0$  inhomogeneity mitigation getting more distinctive with higher off-resonance magnitudes.

Regarding the global SAR performance of the proposed custom trajectory approach, the RF power levels of the optimized pulses were noted in relation to the corresponding single channel mode pulse with ED design. Single channel pulses (1-ch CP) with VD design can require higher RF power levels, whereas for dual channel mode (2-ch pTx) the RF power deposition

is considerably reduced. At first glance, this gain in RF power efficiency is rather counter-intuitive, as the VD design mainly proposes a sub sampling of lower spatial frequencies (*Figure 3.4*). Consequently, one would expect an increase of the required RF power as the sub-sampling is done where most of the target pattern energy lies. Two other effects counteract a hypothesized RF power increase. First, pTx technology has been generally shown to enable enhanced global SAR and RF power efficiency [3, 9, 128]. Second, based on the simulations in *Figure 3.6* and *Figure 3.8* it can be assumed that the off-resonance compensation can require an additional RF power expense. In case of ED EP-2DRF pulses the algorithms for solving the optimization problem tend to turn up RF power trying to resolve off-resonance effects (*Figure 3.8b*). Consequently, also the required additional RF power expense is lowered by sub sampling the accrued phase errors as proposed. Adding up all three effects, the VD approach can offer enhanced RF power efficiency overall.

As indicated by the simulations and experiments in *Figure 3.7* and *Figure 3.9*, a similar off-resonance sensitivity of the ED EP-2DRF pulses independent of the used design scheme for the echo-planar k-space trajectory, i.e. bipolar and flyback design (data not shown) was observed. Both design schemes show strong geometric distortions of the target pattern, but no transmit  $N/2$  ghosting on the basis of off-resonance. Though, the flyback design can be necessary to tackle strong  $N/2$  ghosting due to the imperfections in the gradient delays on the real world scanner, but comes along with a prolonged total RF pulse duration. These observations for the spokes based EP-2DRF pulse were previously shown in [46, 83, 120]. The proposed VD trajectory approach was found to improve off-resonance correction for both echo-planar design schemes, bipolar and flyback design.

Furthermore, the  $B_0$  map informed trajectory design was shown to be advantageous when accelerating the RF pulses up to factor 1.4 (*Figure 3.8*). Beyond this acceleration factor, the VD approach could be still valuable for low RF power design. However, EP-2DRF pulses designed with VD trajectory and higher acceleration factors ( $> 1.4$ ) indicate that aliasing can become a problem. In contrast to pulses with ED trajectory, the VD design exhibits steadily rising RMSE values with increasing acceleration factors. Similar to other approaches using variable density k-space trajectories [47, 129–133], also the proposed VD method shows increased noise-like in-plane aliasing occurring in the corresponding point spread function as the k-space is unevenly sampled. As a consequence, the suppression of the magnetization in the outer volume (regions with defined zero magnetization) is likely to get worse with less available k-space trajectory lines resulting in higher RMSE. Additional aliasing effects can be expected in experiments due to k-space trajectory errors. Trajectory distortions near the k-space center can become critical, as mainly lower k-space frequencies are less densely sampled within the introduced VD approach. Hence, the assessment and correction of the actual k-space trajectory might be necessary as suggested in [92, 93, 134].

The general robustness of the proposed method further relies on the  $B_0$  fieldmap quality. The  $B_0$  map information is used twice for designing VD trajectory based RF pulses: Firstly, for the determination of the actual proposed variable density trajectory. Secondly, for calculating the rewinding term within the system matrix  $\mathbf{A}$  as proposed in the spatial domain design approach [4]. In practice, the acquisition of accurate  $B_0$  fieldmaps can be quite challenging. In-vivo  $B_0$  fieldmaps acquired from problematic regions, e.g. c-spine or t-spine, often contain phase wraps or noisy values, which can subsequently impair the proposed VD trajectory approach and RF pulse design. Therefore, proper phase unwrapping and smoothing of the  $B_0$  maps prior to their utilization are important. Moreover, a regular update of the  $B_0$  fieldmap information has to be investigated to tackle its dynamic change. The compensation of  $B_0$  inhomogeneities will be increasingly more important at higher field strength of 7 T and more. When generally surveying the quality metrics of corresponding single and multi-channel

RF pulses based on the VD trajectory, further RF power savings with even more advanced excitation accuracy can be expected for systems with more transmit channels, such as eight [135, 136] and 32 channel body pTx arrays [137] at 3 T or 16 channel local transmit coils at 7 T [138–140].

In conclusion, the proper target pattern definition with respect to the actual TX resolution of the k-space trajectory was analyzed. Appropriate spatial filtering of the target pattern may be required to avoid an unnecessary RF power level increase and a reduction of the spatial fidelity. Secondly, a  $B_0$  fieldmap information driven variable density trajectory design approach was introduced, which avoids high accrued phase errors in k-space. As a consequence, the capability to compensate off-resonance related geometric distortions and blurring gets considerably enhanced. At the same time, the required RF power deposition is lowered. Similar to the examined pulse type, the methods have been also proven beneficial for 2-D spiral pulses [25] and can be considered for 3-D spatially selective pulses [17, 141] or fast- $k_z$  pulse design [59, 142]. A combination with more sophisticated optimization schemes for e.g. low local SAR pulse design, are also of interest.

## 3.2 Asymmetric 2DRF-Pulse Design

This section contains methods & principles that were accepted for publication in:

R. Schneider, J. Haueisen, and J. Pfeuffer. Asymmetric two-dimensional spatially selective excitation in echo-planar imaging. In *Proceedings of the 22nd Annual Meeting of the ISMRM, Milan, Italy*, page 4436, 2014.

J. Ream, C. Gliemli, M. Lazar, N. Campbell, J. Pfeuffer, R. Schneider, and A. Rosenkrantz. Zoomed epi using parallel transmission for tractography of the prostate gland with an endorectal coil: a feasibility study. In *Proceedings of the 22nd Annual Meeting of the ISMRM, Milan, Italy*, page 2179, 2014.

### 3.2.1 Introduction

In echo-planar imaging (EPI), the effective echo time (TE) is a major limiting factor for the resulting image quality due to off-resonance effects and rapid  $T_2^*$  decay. One approach to tackle this problem is the application of 2-D spatially selective RF pulse (2DRF), which enable reduced field of view (rFOV) imaging and thus a shortening of the echo-train length and TE [46, 121]. However, the 2DRF excitation requires long pulse durations and limits further TE savings. To alleviate this disadvantage, parallel transmission (pTx) was shown to shorten pulse durations without aliasing [15], but the technology is not widely accessible, yet. A simple strategy to further shorten 2DRF pulse durations is proposed, which is independent of pTx acceleration. The approach is shown to offer substantial TE savings without affecting the excitation quality. For this purpose, phantom and human in-vivo experiments were conducted to show the benefits.

### 3.2.2 Methods

The proposed method generally applies to multi-dimensional spatially selective RF pulses, which are based on a symmetric TX trajectory, e.g. the EP, which is commonly used for 2DRF

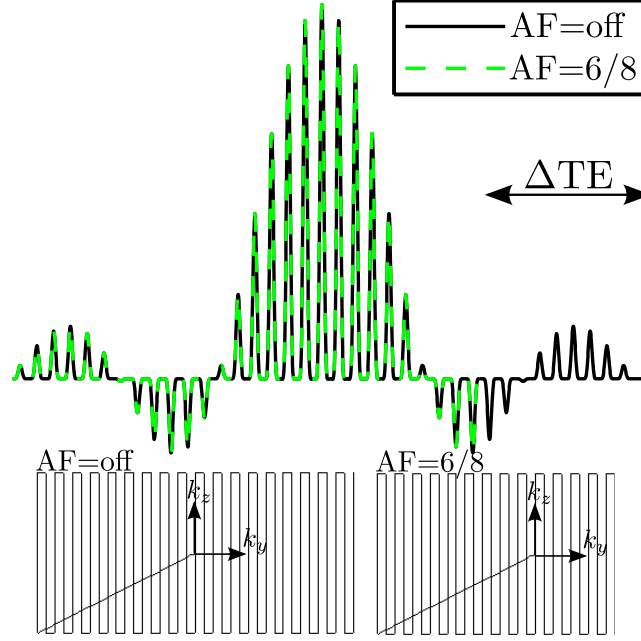


**Fig. 3.10:** Exemplary EP-2DRF pulse with  $AF=6/8$  and corresponding EP k-space trajectories.

pulses in rFOV imaging [46, 121]. In this case, the symmetry of k-space can be exploited similar to the partial-Fourier method in imaging: Particularly for the TX EP trajectory, lines of the second trajectory half can be spared out to a certain degree without any severe penalties in excitation quality. The reduction of the pulse duration can be directly transferred into TE savings (*Figure 3.10*). This can be applied in addition and independently of potential pTx accelerations. A phantom study was pursued to analyze the degree of asymmetry that can be applied to 2-D spatially selective RF pulses based on an echo-planar trajectory (EP-2DRF) without degradation in excitation quality. Asymmetry factors (AFs) from  $5/8$  to  $7/8$  were systematically applied to the EP-2DRF trajectory, i.e. only  $5/8$  to  $7/8$  of the transmit (TX) k-space trajectory was encoded. EP-2DRF pulses were designed according to [46] using a Hamming window to suppress any truncation artifacts. Images were acquired on a 3 T MAGNETOM Skyra scanner with two transmit channels (Siemens, Erlangen, Germany) using a prototype gradient-echo EPI sequence with FOV  $180 \times 180 \text{ mm}^2$ , matrix  $128 \times 128$  and TR / TE 100/35 ms. The same experiments were pursued with pTx acceleration factor  $R = 1.4$  following the approach of [25]. The potential benefits of the asymmetric EP-2DRF excitation towards TE savings and resulting SNR gains were further investigated in human in-vivo diffusion experiments of the posterior brain. rFOV diffusion images were obtained in an in-house-modified bipolar acquisition scheme with b-values 50, 500,  $800 \text{ s/mm}^2$ , slices 15, slice thickness 3 mm, FOV  $240 \times 90 \text{ mm}^2$ , matrix  $128 \times 48$  and TR 3400 ms. EP-2DRF pulses were designed without and with a trajectory asymmetry of  $AF=6/8$  with and without pTx acceleration, respectively. TE was always set to the lowest possible value.

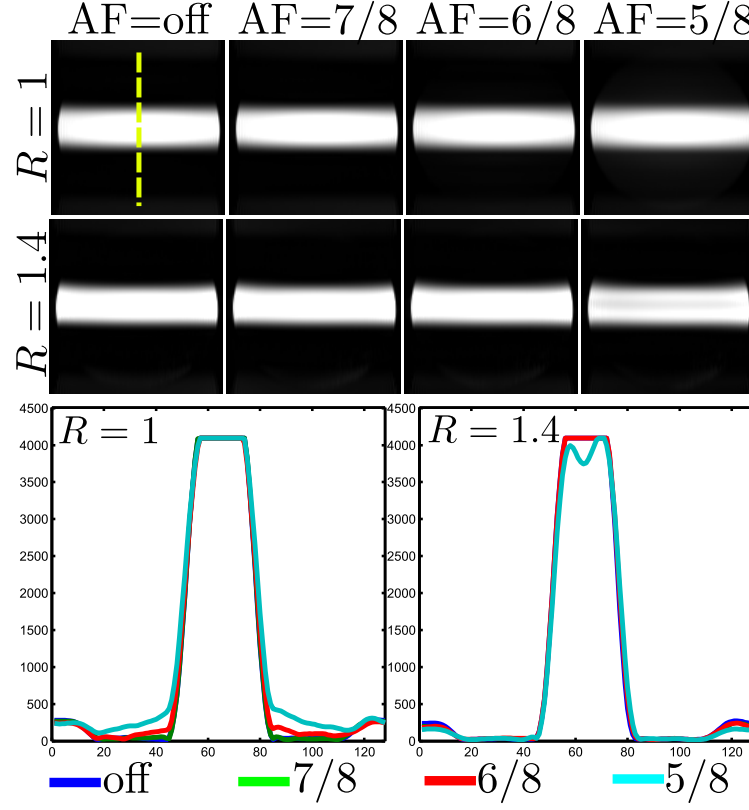


**Fig. 3.11:** EP-2DRF excitations with different asymmetry factors. Top row: no acceleration. Middle row: 1.4 fold acceleration. Bottom row: 1-D profiles of the different experiments (dashed line).

### 3.2.3 Results

Phantom images acquired with EP-2DRF pulses of different asymmetry factors are shown in *Figure 3.11*. The excitation quality is maintained up to an asymmetry factor of 6/8 and independent of pTx acceleration. With large asymmetry (5/8), deviations from the targeted excitation profile can be observed in both the outer- ( $R = 1$ ) and inner-volume ( $R = 1.4$ ). Savings in EP-2DRF pulse durations can be directly transferred to shorter TE and increased SNR in the human diffusion experiments (*Figure 3.12a*). Here, TE savings up to 17 ms could be directly achieved from the introduced asymmetry. The TE savings using (AF 6/8,  $R$  1.0) resulted in an average SNR increase of 25% compared to the experiments using the common EP-2DRF pulse (*Figure 3.12b*). Similar TE savings and slightly higher gains in SNR could be achieved with 2.1 fold acceleration. Moreover, when combining the asymmetric design with pTx acceleration, another SNR increase of 8% from 30% to 38% was obtained.

### 3.2.4 Discussion

With the introduction of asymmetry to EP-2DRF, the pulse duration can be remarkably reduced without affecting the excitation quality independently from pTx acceleration. The

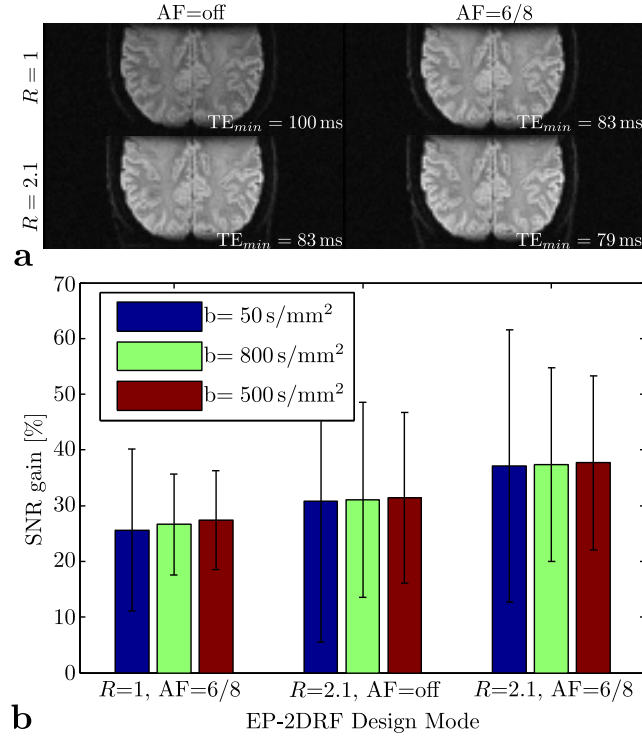


**Fig. 3.12:** **a**  $b = 800$  s/mm<sup>2</sup> weighted rFOV diffusion images acquired with different EP-2DRF pulses. **b** Mean gain in SNR over all slices in dependence of  $b$ -values, pTx acceleration  $R$  and RF asymmetry  $AF$ . Values are stated relative to the experiments acquired with  $R = 1$  and no asymmetry ( $AF=off$ ).

resulting savings in TE and gain in SNR can be significant in EPI-based sequences. However, the absolute level of TE savings does not only depend on the chosen EP-2DRF design parameters (e.g. slice thickness), but also on sequence details as diffusion parameters and image resolution. Further note that in case of TX acceleration only half of the omitted encoding lines contribute to TE shortening, as the EP trajectory is equally sub-sampled. In contrast, the savings due to the asymmetric design account completely for TE reduction. The introduced approach can be easily transferred to other symmetric multidimensional spatially selective 2-D and 3-D RF pulses.

## pTx z-Shim for Local Signal Recovery

This chapter contains methods & principles that were accepted for publication in:

R. Schneider, C. Gliemli, C. Geppert, J. Haueisen, F. Boada, and J. Pfeuffer. Local signal recovery in clinical flash imaging with parallel transmission. In *Proceedings of the 22nd Annual Meeting of the ISMRM, Milan, Italy*, page 4777, 2014.

R. Schneider, F. Boada, J. Haueisen, and J. Pfeuffer. Automated slice-specific simultaneous z-shim method for reducing b1 inhomogeneity and susceptibility-induced signal loss with parallel transmission at 3t. *Magn Reson Med*, page in press, 2014. ISSN 1522-2594.

### 4.1 Introduction

In high-field MR imaging the susceptibility-induced signal loss in  $T_2^*$ -weighted images is still a major problem in many clinically important GRE-based sequences, such as fast low angle shot (FLASH) and susceptibility weighted imaging (SWI). In the human brain, prominent signal losses mainly occur in the frontal orbital and inferior temporal cortex and can seriously impede the diagnosis of, e.g. stroke and hemorrhage. Longer echo times as required in blood oxygenation level dependent (BOLD) functional MRI studies impair the effect, which is particularly caused by the  $B_0$  field variations along the slice profile, i.e. the through-plane field components.

To address this problem several techniques have been proposed in the past, but most of them are accompanied by other drawbacks and were therefore not practical for clinical routine: Z-shim methods [143–147] have been shown to tackle the through-plane magnetic field variations by applying different gradient z-lobes after the excitation pulse, but require multiple sub-images and can significantly increase scan time. Protocol parameters can be optimized [148, 149] for reducing the signal loss, but come along with decreased coverage and longer TR. With additional  $B_0$  shim coils [150, 151] or diamagnetic shim materials [152–154] the local field inhomogeneity and thus the signal loss can be mitigated, but can raise manual efforts [152–154], discomfort of the patient [150, 153, 154] or additional specialized hardware [151]. An alternative solution includes custom-designed three-dimensionally tailored [14, 59, 141] and spectral-spatial [81, 82, 155, 156] RF pulses, which have been shown promising to compensate the through-plane susceptibility-induced signal loss without additional hardware or major imaging constraints. However, RF pulse durations can be inefficiently long and

increase TE / TR. They can be shortened in combination with the pTx technology [14]. Nevertheless, these RF pulse design approaches show generally high computational complexity and thus have inadequate computation times for clinical multi-slice imaging. Moreover, the spatial selectivity along the slice direction, i.e. the slice-selectivity, is not inherently provided, but has to be fully optimized. Hence, the RF pulse computation relies on the proper sampling density and coverage of the RF design grid to enable an accurate definition of the slice profile without aliasing effects. The custom designed RF pulses are also difficult to realize within RF hardware and SAR limits. Critical peak voltages occur already at moderate flip angle levels around 30 degrees and limit their application for higher flip angles. Recently, *Deng et al.* [8] proposed another RF pulse design method, which is based on common slice-selective RF pulses. The RF waveforms are applied with a different time-delay on separate transmit coils to create a pre-compensating z-shim phase along the slice profile. In contrast to the RF pulse design methods stated above, this approach has conceptually short RF pulse durations, robust spatial slice encoding and low computational complexity. The original approach by *Deng et al.*, using a custom-built local 4-channel transmit head coil, revealed promising results in recovering the signal, but generally left noticeable  $B_1$  inhomogeneity effects being related to the RF coils' spatial profiles [8]. Moreover, the time-delay was manually adjusted to match the desired signal recovery level, which hinders its application in clinical practice.

In this work, an extension to the approach by *Deng et al.* [8] for  $B_1$  inhomogeneity mitigation and automatic time-delay determination on the basis of the prevailing  $B_1$  and  $B_0$  maps is proposed. The approach is implemented and integrated in a commercially available 3T MR scanner with two fully integrated whole-body transmit channels. The proposed method was evaluated with experiments in humans using a clinical multi-slice FLASH sequence with a low flip angle level. In addition, a breath-hold BOLD functional MRI study was performed with GRE-EPI using high flip angles of 90 degrees. It is shown that major areas with susceptibility-induced signal loss can be recovered by the proposed automated approach, but at cost of a SNR penalty.

## 4.2 Theory

### *Automatic Time-Delay Determination*

The RF-based z-shim approach uses a time-delayed excitation to impose a linear phase gradient along the slice profile to pre-compensate the spatially varying through-plane magnetic field gradients. This concept is derived from the basic Fourier formalism, where a shift in the time-domain creates a linear phase in the frequency domain. Analogously, in the presence of a slice-selection gradient  $G_z$  a time-shifted RF pulse waveform  $b(t)$  results in a phase term along the slice profile  $m(z)$ . When combining this approach with pTx, a simultaneous z-shim can be achieved by applying  $b(t)$  on  $C$  separate transmit channels with an individual time-delay  $\tau_c$ , respectively [8]:

$$b_c(t + \tau_c) \leftrightarrow m(z)e^{i\gamma G_z z \tau_c}, \quad (4.1)$$

where  $b_c(t + \tau_c)$  is the RF waveform of the  $c$ th transmit channel delayed by  $\tau_c$ . With increasing time-delay of the static RF waveform the steepness of the phase-gradient along the slice-profile can be determined, which potentially compensates the prevailing through-plane field gradient



$G_s$ . Ideally, the time-delay  $\tau_c$  at slice-position  $z_n$  of  $N$  slices is individually matched to cancel out the through-plane phase variation at given echo-time  $TE$ :

$$G_z \cdot \tau_c(z_n) = G_s(x, y; z_n) \cdot TE. \quad (4.2)$$

However, this approach is not able to fully resolve the required spatially varying phase gradient as the imposed linear phase is globally applied along the slice profile  $m(z)$  independent from the in-plane  $x, y$  coordinates. On the other hand, the spatially localized sensitivity profiles  $S_c$  of the transmit coils combined with individual time-delays  $\tau_c$  again allow some degree of spatially varying phase distributions. Further, it was shown that the field gradient  $G_s$  can be roughly predicted from the fieldmap  $\Delta B_0(x, y; z_n)$  offset as a first linear approximation [81, 157] with  $G_s(x, y; z_n) = \alpha \cdot \Delta B_0(x, y; z_n)$ . Thus, the  $B_0$  map being initially acquired for pTx RF pulse optimizations can be reused and no additional adjustments are required. After adding these assumptions to Equation 4.2, the slice- and RF-coil-specific time-delay can be calculated by means of

$$\tau_c(z_n) = \frac{\alpha \cdot \max(\Delta B_0(x, y; z_n))_{\mathbf{W}_{S_c}} \cdot TE}{G_z}, \quad (4.3)$$

where  $\alpha$  is the slope describing the functional relation between the frequency offset and through-plane field gradient and  $\max(\Delta B_0(x, y; z_n))$  the worst-case field offset and thus most critical field gradient within the coil-specific region of interest ROI  $\mathbf{W}_{S_c}$ . From earlier studies at 3 T [81, 157] the typical value of  $\alpha$  was found between  $-1.0$  and  $-2.0 \mu\text{T/m/Hz}$ . The coil-specific region of interest  $\mathbf{W}_{S_c}$  aims to localize the impact of the  $c$ th RF coil of the spatial sensitivity profile  $S_c(x, y; z_n)$ . To match the most suitable transmit coil to a given spatial field gradient distribution  $G_s(x, y; z_n)$  a sequential algorithm is used, which is capable to handle strongly overlapping coil-profiles. First, initial coil-specific region of interests  $\tilde{\mathbf{W}}_{S_c}$  are computed by adequate thresholding of the sensitivity profiles. The threshold is defined that all initial coil masks  $\tilde{\mathbf{W}}_{S_c}$  completely cover the ROI  $\mathbf{W}$  with the smallest possible overlap. Then, final coil-specific region of interest  $\mathbf{W}_{S_c}$  are subsequently calculated by excluding the afore processed ROIs for  $c > 1$ :  $\mathbf{W}_{S_{c+1}} = \tilde{\mathbf{W}}_{S_{c+1}} - \bigcup_{i=1}^c \tilde{\mathbf{W}}_{S_i}$ . Last, the  $\mathbf{W}_{S_c}$  are correlated with the most critical dephasing gradients to find the proper time-delays. To make full use of the RF coils providing high local spatial sensitivity, the RF coil indices can be ordered according to their average  $B_1$  sensitivity prior to the masking and delay calculation process.

Figure 4.1 illustrates the basic algorithm for an arbitrary number of slices and transmit channels. After the initial estimation of the through-plane  $B_0$  field gradient from the prevailing  $B_0$  maps, a channel-and slice-specific time delay can be determined by evaluating the impact of the transmit sensitivity profiles. The example was pursued for a local transmit array with rather distinct coil sensitivity profiles and a global 2-channel body transmit array as used in this study. The latter shows strongly overlapping coil profiles with a large spatial scope, so that a single coil is quite sufficient to cover the complete ROI  $\mathbf{W}$ . Note that solely the worst-case field gradient is considered within the coil specific region of interest to determine the corresponding time-delay. The higher the absolute value of the time-delay the higher is the steepness of the pre-compensating phase along the slice profile. The sign of the time-delay is determined to counteract the direction of the worst-case field gradient in presence of slice-select gradient  $G_z$ . In this example, the second and third transmit channel of the local and the first transmit channel of the global TX array mostly contribute to the

pre-compensation of the signal loss in the frontal orbital cortex as indicated by  $G_s(x, y; z_n)$ . Clearly, other more sophisticated approximations are possible. For example, the histogram of the field gradient distribution within  $\mathbf{W}_{S_c}$  can be analyzed to avoid extreme values associated with noise and to provide a more robust estimate.

### *B<sub>1</sub> Inhomogeneity Correction*

The approach is further extended towards  $B_1$  inhomogeneity mitigation on the basis of the spatial domain design approach [4]. After defining the optimal time-delay per channel and slice, the algorithm aims to calculate proper TX coil power levels for each individual setting. Please note that prior  $B_1$  map normalization and channel-specific ROI processing was solely applied in the context of the time-delay determination. Here, the unprocessed  $B_1$  maps information within the complete ROI is used. When discretizing in time and space, an inverse problem has to be numerically solved to determine the optimized RF pulse  $\mathbf{b}_{full}$ :

$$\hat{\mathbf{b}}_{full} = \arg \min_{\mathbf{b}_{full}} \{ \|\mathbf{A}_{full} \mathbf{b}_{full} - \mathbf{m}_{des}\|_{\mathbf{W}}^2 + R(\mathbf{b}_{full}) \}, \quad (4.4)$$

where  $\mathbf{A}_{full}$  denotes the overall system matrix,  $\mathbf{m}_{des}$  the desired target magnetization pattern,  $\mathbf{W}$  the ROI and  $R(\mathbf{b}_{full})$  a regularization term. Essentially, the posed  $B_1$  optimization problem is quite similar to the basic RF shimming approach, where a flat target magnetization  $\mathbf{m}_{des}$  has to be optimized. For this purpose, RF-transmit-channel-specific complex optimization weights  $w_c$  are introduced that aim to optimally scale a static RF waveform  $\mathbf{p}$ . But in contrast to conventional RF shimming, the static RF waveform is not applied simultaneously on all  $C$  transmit channels, but the onset of the waveform  $\mathbf{p}$  differs from channel to channel due to the introduced time-delay  $\tau_c$ :

$$\mathbf{b}_c(t_j) = \begin{cases} w_c \cdot \mathbf{p}(t_{j-N_{center}} - \tau_c) & \text{for } N_{center} + \tau_c/\Delta t \leq j \leq N_{center} + N_p + \tau_c/\Delta t \\ 0 & \text{otherwise} \end{cases} \quad (4.5)$$

with  $j = 1 \dots N_t$  and  $\mathbf{k}(t_{N_{center}+N_p/2}) = 0$ ,

where  $\mathbf{b}_c$  is the final discretized RF waveform of the  $c$ th channel with  $N_t$  time samples,  $\Delta t$  the sampling duration,  $N_p$  the number of samples of the static waveform  $\mathbf{p}$ .  $N_{center}$  denotes the sampling-onset-point, from which the center of a symmetric RF waveform aligns with the excitation k-space center. For the optimization process, the basic pulse shape  $\mathbf{p}$  is transferred from the solution vector  $\mathbf{b}_{full}$  to the matrix  $\mathbf{A}_{full}$  [25, 62], so that the actual solution vector is solely composed of the optimization weights  $\mathbf{b}_{full} = [w_1 \dots w_C]^T$ . In this case the overall system matrix  $\mathbf{A}_{full}$  is concatenated by both RF-channel-specific system matrices  $\tilde{\mathbf{A}}_c$  and diagonal matrices  $\tilde{\mathbf{S}}_c$ . The latter hold the information about the RF coil sensitivity  $S_c$  at the spatial coordinates  $\mathbf{r}$  with  $N_s$  samples, respectively.

$$\mathbf{A}_{full} = [\tilde{\mathbf{S}}_1 \tilde{\mathbf{A}}_1 \dots \tilde{\mathbf{S}}_C \tilde{\mathbf{A}}_C] \quad \text{with } \tilde{\mathbf{S}}_c = \text{diag}\{S_c(\mathbf{r})\} \quad (4.6)$$

The  $i$ th spatial element  $a_{ic}$  of a system matrix  $\tilde{\mathbf{A}}_c$  further incorporates information about the time course of the k-space trajectory  $\mathbf{k}$  and the evolving off-resonance effects based on the main field inhomogeneities  $\Delta B_0$  within the total pulse duration  $T_{pulse} = N_t \Delta t$ .

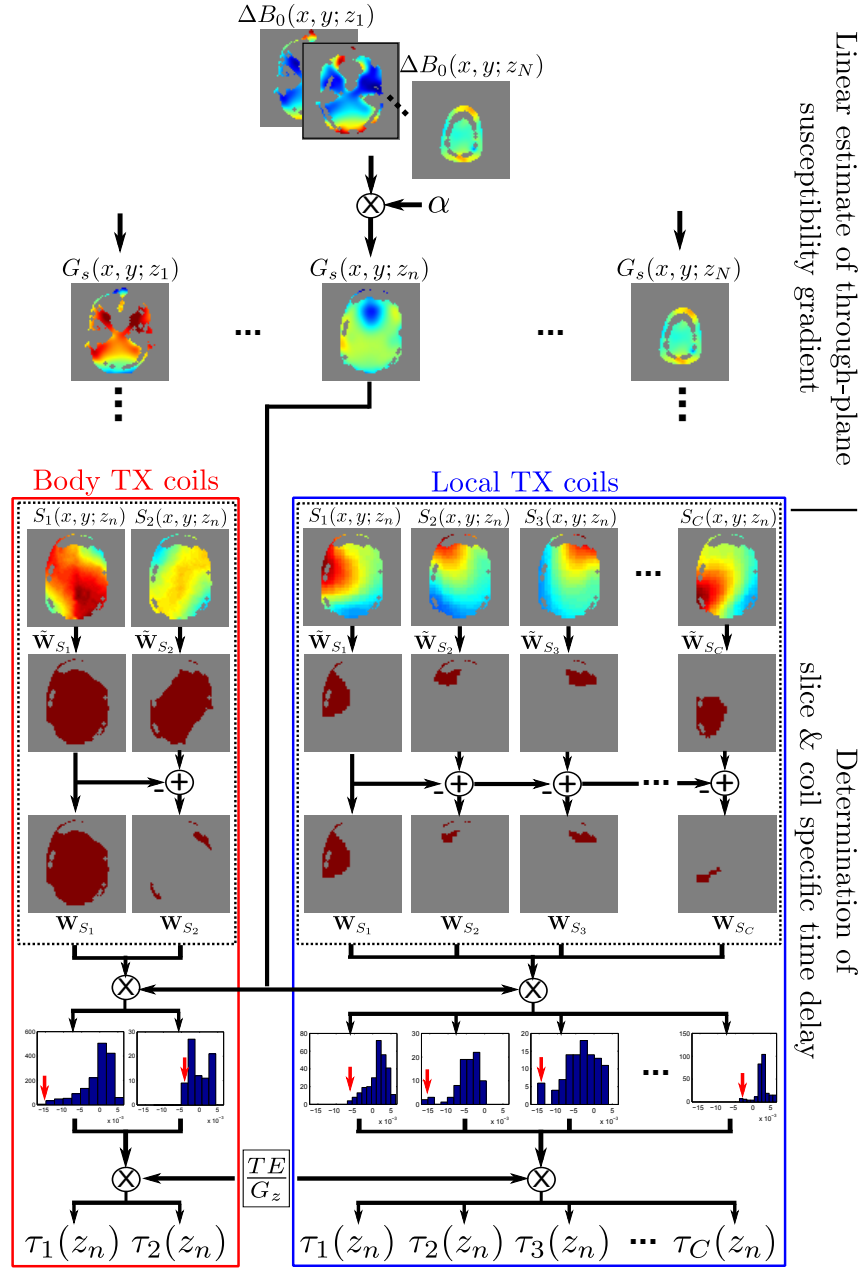


**Fig. 4.1:** Basic automated approach for determining a slice and transmit channel specific time-delay for imposing a simultaneous z-shim on an exemplary 2 channel body or 8 channel local transmit system. Based on the prevailing  $B_0$  maps  $\Delta B_0(x, y; z_n)$  the through-plane field gradient  $G_s(x, y; z_n)$  is predicted based on a linear estimate. Further, by considering the spatial sensitivity profiles of the transmit channels, a time-delay  $\tau_c(z_n)$  can be sequentially calculated to impose an adequate z-shim within the corresponding region of interest  $W_{S_c}$ .

$$a_{ic} = \sum_{j=N_{center}+\tau_c/\Delta t}^{N_{center}+N_p+\tau_c/\Delta t} i\gamma M_0 \Delta t e^{i\mathbf{r}_i \mathbf{k}(t_j)} e^{i\gamma \Delta B_0(\mathbf{r}_i)(t_j - T_{pulse})} \mathbf{p}(t_j - N_{center} - \tau_c) \quad (4.7)$$

Note that the time dimension is compressed by a factor  $N_p$  by the transfer of the static waveform  $\mathbf{p}$  from  $\mathbf{b}_c$  to the matrix  $\tilde{\mathbf{A}}_c$ . Thus, like in RF shimming the final dimensions of  $\mathbf{A}_{full}$  are  $N_s \times C$ , but differ slightly in its composition for  $\Delta t_c \neq 0$ .

### 4.3 Methods

#### *RF Pulse Design*

The time-delayed RF pulses were calculated in MATLAB 8.0 (MathWorks, Natick, MA) using the magnitude-least-squares approach of [15]. Common Hamming-filtered RF sinc pulses were used as static slice-selective RF waveforms  $\mathbf{p}$  discretized with  $N_p = 200$  samples. Slice- and TX coil specific RF pulses were optimized using the presented two-step approach. First, optimized time-delays were determined matching the coil-specific impact regions to the spatial distribution of the through-plane main field gradients estimated from the  $B_0$  map. Then, the set of time-delays was considered during the  $B_1$  optimization of the TX coil specific RF waveform weights. To control the degradation of the slice profile [8], high time-bandwidth products were used and the maximum time delay was limited to 50% of the main sinc lobe duration. Time-delays below 10  $\mu\text{s}$  were discarded due to their low impact. The slice-selection gradient amplitude  $G_z$  was set to 19 mT/m. All pulses were regularized to stay within the given RF hardware and SAR limits. No special SAR handling was used in this study beyond the commercially implemented SAR supervision features on the scanner system.

#### *Experiments*

All experiments were performed on a 3 T MAGNETOM Prisma system equipped with two independent and fully integrated whole-body transmit channels (Siemens AG, Healthcare Sector, Erlangen, Germany). The complex RF coil sensitivity profiles were measured using a pre-saturation TurboFLASH sequence [99]. A fat-water in-phase  $B_0$  map was calculated on the basis of the multi-echo approach similar to [106]. A regularized spatial filter was applied to avoid the presence of noisy extreme values [102]. The obtained  $B_0$  map was incorporated into both the RF pulse calculation (Equation 4.7) and the slice- and RF-coil-specific time-delays (Equation 4.3). Proof-of-concept human in-vivo experiments were pursued for a clinical multi-slice FLASH sequence and breath-hold BOLD functional MRI (fMRI) study for 3 healthy subjects. Breath-hold fMRI is known to create large BOLD contrast over the whole brain and is therefore also available to evaluate the method.

FLASH images were acquired with FOV  $240 \times 240 \text{ mm}^2$ , matrix  $256 \times 256$ , slices 21, slice thickness 5 mm, TE / TR 20 / 600 ms, GRAPPA acceleration factor 2 and 25 degrees flip angle resulting in a total acquisition time of 1 : 26 min. Several scenarios were applied using the standard RF excitation in circular polarized (CP) mode and the presented time-delayed excitation. To highlight the differences to the approach by Deng *et al.* [8], different time-delay

modes were explored: *a)* the default excitation with a manually optimized global static delay of  $\tau_2 = -150\mu\text{s}$  in CP mode and no  $B_1$  inhomogeneity mitigation, *b)* with the same global static delay including the proposed  $B_1$  correction and *c)* using both  $B_1$  optimization and automatic time-delay determination. In *a)* and *b)* the global static delay was chosen for the second RF coil providing generally the higher  $B_1$  sensitivity and was found to offer an appropriate signal recovery across all slices.

Four metrics were calculated to quantify signal recovery and image quality. First, the level of signal recovery was assessed similar to [156] by evaluating the percentage of voxels in void regions of the standard RF sinc pulse images recovered by the pTx z-shim pulses. The void regions were defined as areas that fall below 10 percent of the slice-specific intensity maximum. Background noise was masked out by using the mask  $\mathbf{W}$  gained from the  $B_1$  and  $B_0$  map adjustments. For the residual brain areas not suffering from signal loss, the sum of squared differences (SSD), standard deviation (STD) of differences and mean image intensity loss were calculated as a distance to the standard RF sinc acquisitions to quantify the preservation of signal intensity and image quality. In particular, the SSD metric covers the general loss in SNR and potentially new signal dropouts caused by the time-delayed RF excitation. On the other hand, the STD metric assesses the degree of introduced image inhomogeneity effects assuming that the RF sinc images provide proper image quality. The mean image intensity loss is stated as a rough estimate for the loss of SNR relative to the RF sinc images. Furthermore, two distinctive slices, i.e. with and without initially strong signal dropouts, were chosen for a more thorough visual analysis. Both were compared in dependence of different RF pulse optimization modes and  $\alpha$  values. Difference images were calculated relative to the standard RF excitation case with normalized image intensity.

fMRI breath-hold experiments were pursued consisting of alternating 19.2s blocks of a breathing / breath-holding paradigm with a total duration of 3 : 22 min. Sequence parameters were similar as above but with matrix  $96 \times 96$ , TE / TR 30 / 3200ms and 90 degrees flip angle. Here, standard RF excitation was solely compared to the proposed automated time-delayed excitation approach with  $\alpha = -2\mu\text{T/m/Hz}$ . fMRI data were processed using the commercially available software ('Inline BOLD', 'Neuro3D') available on the scanner. In short, all image time series were motion corrected and realigned with the first time frame. Regressors were modelled by the convolution of the block-designed breath-hold / normal-breathing paradigm with the canonical hemodynamic response function (HRF). Statistics across the 21 slices were calculated for all brain voxels using a general linear model approach [158]. The resulting whole-brain t-maps were further evaluated analyzing activation coverage in manually selected ROIs versus the other brain areas at threshold  $t > 2.5$ .

## 4.4 Results

### *Image Artifacts with Time-Delayed RF Excitation*

To prove the necessity for individually tailored time-delays and subsequent  $B_1$  inhomogeneity correction, the original method [8] with a static delay is systematically analyzed for two distinct slices across two subjects (*Figure 4.2*). With increasing time-delays a perturbation of the slice profile, i.e. a slight narrowing becomes observable. At the same moment, signal can be visibly recovered at the prefrontal cortex, but at different optimal levels: In subject 1, signal is progressively recovered up to the highest time-delay of  $-180\mu\text{s}$ . On the other hand,

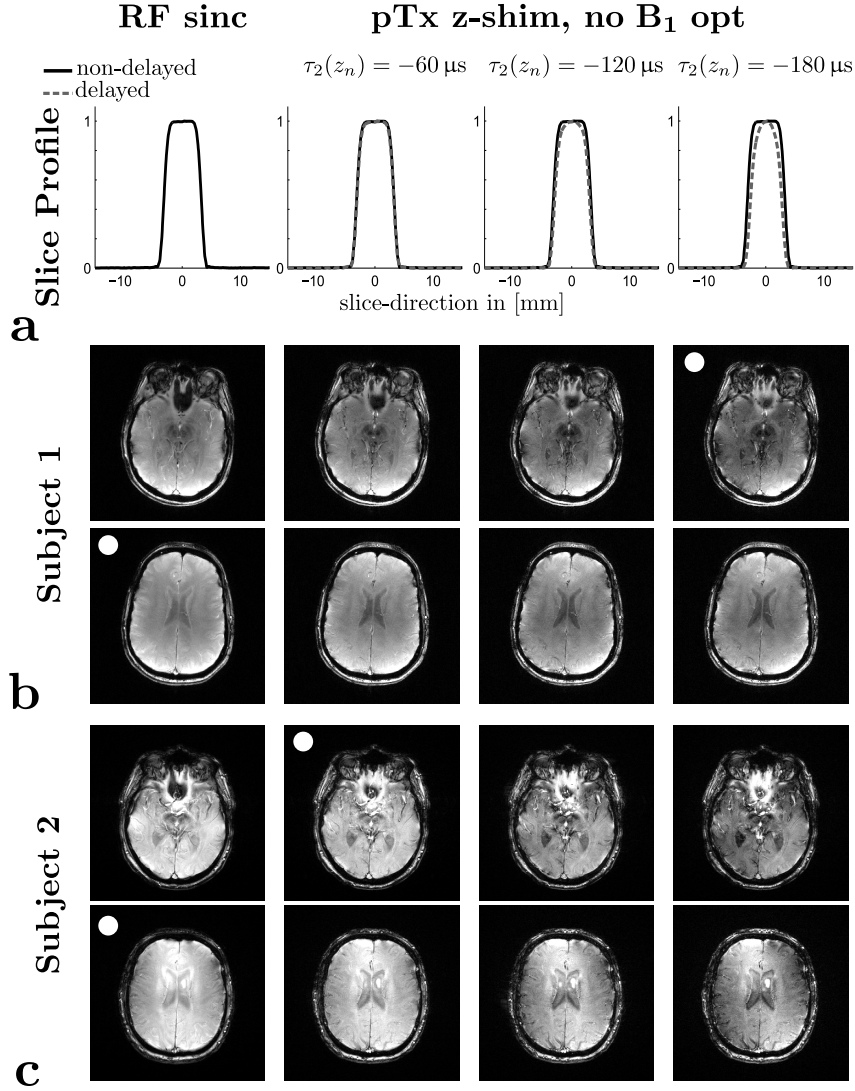


**Fig. 4.2:** Imaging artifacts associated with time-delayed RF excitation without  $B_1$  inhomogeneity correction. pTx z-shim RF pulses were applied without  $B_1$  optimization with static time-delays across all slices. Time-delays were stepwise increased from 0 to  $-180 \mu s$  in  $60 \mu s$  steps (from left to right). **a** Corresponding slice-profiles measured in a phantom. **b** FLASH images of two disctinct slices with and without initial susceptibility artefacts. **c** similar slice positions as in **b**, but different subject. With increasing time-delay, more prominent SNR penalties,  $B_1$  inhomogeneity and slice perturbations can be observed. The optimal time-delay (indicated by the white circle in the upper left corner of the images) providing the best compromise of signal recovery and artifact level varies from slice-to-slice and subject-to-subject.

signal is already sufficiently recovered with  $-60 \mu\text{s}$  in subject 2 at a similar anatomic position. A further increase of the time-delay does not provide any further boost in signal recovery, but a deterioration of image quality in the other areas. Similarly, the overall SNR and image homogeneity are generally impaired when applying time-delayed RF pulses to areas without through-plane  $B_0$  variations as is the case in the slices presented in the lower rows of *Figure 4.2*. Here, the z-shimming phase gradients lead to undesired signal loss. Consequently, the optimal time-delays should be limited to a required minimum to preserve the slice-profile and image quality.

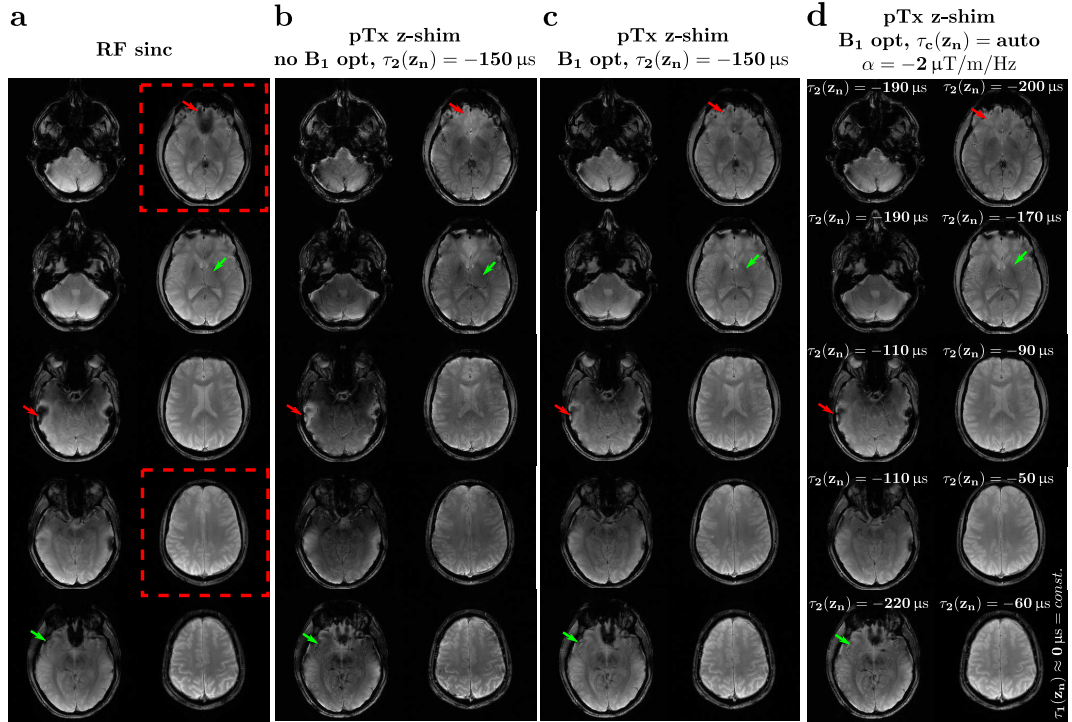


**Fig. 4.3:** Multi-slice FLASH images acquired from one volunteer with flip angle =  $25^\circ$  and different RF excitation modes. **a** Standard RF sinc excitation in CP mode. **b** The original simultaneous z-shim approach without  $B_1$  optimization and a global static delay of  $-150 \mu\text{s}$ . **c** Same as **b**, but with  $B_1$  inhomogeneity mitigation. **d** The final proposed approach including  $B_1$  inhomogeneity correction and a slice specific determination of the time delays. In **b-c** the delay was applied solely to the second transmit channel with dominating transmit sensitivity. In **d** the time-delay associated with first transmit channel having less  $B_1$  sensitivity was practically always resulting to minor values close to  $0 \mu\text{s}$  (see *Figure 4.4*). Exemplary areas initially suffering from through-plane field variation caused signal loss are marked with red arrows. Green arrows indicate areas, which partially show increased  $B_1$  shading due to the time-delayed excitation. The two red encircled slices were further analyzed in *Figure 4.4* and *Figure 4.5*.

*FLASH Experiments*

A representative subset of FLASH images of volunteer 2 is shown in *Figure 4.3* acquired with different RF excitation modes. From the visual inspection of the data using the standard RF sinc pulse, typical through-plane susceptibility-induced signal losses can be located in frontal and lower temporal brain areas (*Figure 4.3a*). All experiments based on the simultaneous pTx z-shim approach (*Figure 4.3b-d*) can partially recover the signal loss by the application of a time-delayed excitation on two separate whole-body RF excitation coils. First, images with the original pTx z-shim method (*Figure 4.3b*) were obtained by manually adjusting the time-shift to provide the most adequate signal recovery level across all slices. For this purpose, a static time delay of  $-150\ \mu\text{s}$  was found most suitable for all subjects and was applied to the second RF transmit channel with higher spatial sensitivity. Again, the images indicate that the signal recovery comes along with increased  $B_1$  shading effects and a globally reduced SNR. Second, the same time-delay was used, but in combination with the proposed  $B_1$  optimization approach (*Figure 4.3c*). Here, shading effects got visibly mitigated, but partially at cost of a lower, spatially dependent signal recovery level (e.g. see lower left image of *Figure 4.3*). Finally, the introduction of the automatic time-delay determination offers a slice-dependent time-shift (*Figure 4.3d*). For all subjects, the time-delays varied from  $-40\ \mu\text{s}$  to  $-250\ \mu\text{s}$  with  $\alpha = -2\ \mu\text{T/m/Hz}$  and correlate well with the prevailing initial through-plane susceptibility artifact level. The presented algorithm to determine the coil specific time-delays always yielded a single delay associated with the second coil with dominating spatial sensitivity (*Figure 4.4*). In matters of the corresponding spatial profile the second channel already covers sufficiently the whole FOV. Consequently, the first coil with lower  $B_1$  sensitivity showed only minor remaining coil-specific ROIs resulting in negligible time-delays. When comparing the proposed method to the  $B_1$  shimmed static delay results, no noticeable differences in image quality can be observed at first glance.

However, differences in the signal recovery and image preservation performance become more apparent by studying the proposed quality metrics (*Table 4.1*) and difference images (*Figure 4.5*). For the latter, slice 11 (affected by signal loss) and slice 16 (not affected) of *Figure 4.3* were picked for the detailed visual analysis and highlight the shortcomings of the different approaches. Regarding the experiments with a global time-delay (*Figure 4.5a,b*), the  $B_1$  optimization helps to balance the overall signal intensity level of both the recovered and non-affected areas. This results in an apparent reduction of the signal recovery intensity, but also in less degradation of the average intensity level and image quality (from  $-55\%$  to  $-35\%$ , SSD (STD) reduced from 1.00 (1.00) to 0.31 (0.68)). Still, slice 16 is unnecessarily compromised despite of the absence initial susceptibility artifacts. The automated time-delay determination tries to overcome this issue by offering a suitable time-delay by considering the  $B_0$  maps for a through-plane field gradient estimate. The appropriate choice of the  $\alpha$  value is important to describe this functional relationship. *Figure 4.5c-e* show the results with stepwise decreased  $\alpha$  values from  $-1$  to  $-3\ \mu\text{T/m/Hz}$ . Here, the image quality of slice 16 can be maintained independent from the chosen value. On the other hand, a trade-off between signal recovery level and SNR loss can be observed for slice 11 and in all quality metrics. With higher absolute alpha values more signal is likely to recover, but involves worse  $B_1$  shimming quality and SNR level. Across all experiments,  $\alpha = -2\ \mu\text{T/m/Hz}$  was observed as the best compromise between those factors.



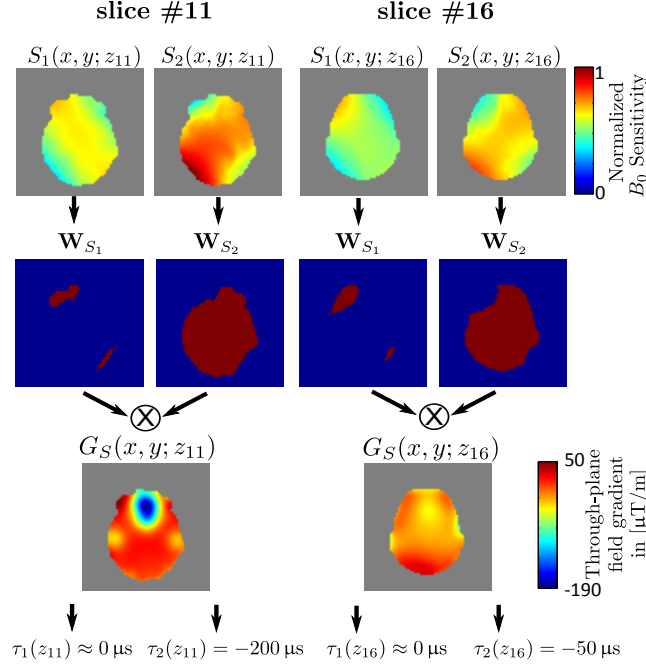


**Fig. 4.4:** Detailed illustration of the proposed time-delay determination of two FLASH images with and without initial through-plane susceptibility artifacts. The signal dropout in slice 11 can be well associated with the corresponding through-plane field gradient maps. The  $B_1$  maps reveal that the second RF channel always provides the superior  $B_1$  sensitivity covering quite the whole FOV. After determining the coil specific ROIs, the remaining mask of the first transmit channel shows only a minor spatial impact. The correlation of the coil specific ROIs with the estimated through-plane main field gradient results always in a distinct delay for the second and a negligible delay for the first RF transmit channel.

#### *fMRI Experiments*

In *Figure 4.6* selected slices of the processed breath-hold fMRI experiment are exemplary shown for two volunteers. Particularly, EPI images of the first time frame are overlaid with the thresholded BOLD fMRI activation maps for  $2.5 < t < 15$  using the standard RF sinc (*Figure 4.6a,d*) and proposed time-shifted spokes excitation (*Figure 4.6b,d*) with  $90^\circ$  flip angle. Differences in the spatial activation are further highlighted in *Figure 4.6c,f* where the discrepancy in coverage is encoded in red (pTx z-shim) and blue (RF sinc) color, respectively. Similar to the FLASH experiments prominent signal dropouts in the frontal orbital and temporal cortex can be observed in the acquired unprocessed EPI data using the standard RF pulse. Clearly, this results also in a noticeable loss in the corresponding areas of the BOLD activation maps. This through-plane susceptibility induced signal loss got visibly recovered with the application of the slice-specific time-delayed excitation, but can be partially accompanied with BOLD activation loss in other brain areas. This trade-off can be noticeably recognized in slices of subject 1 suffering from strong susceptibility, e.g. see 4th slice in 1st row in *Figure 4.6a,b*. The average change of the BOLD activation coverage regarding the different RF excitation is further summarized in *Table 4.2* for all subjects. The fMRI sensitivity was compared in manually selected ROIs (green contour lines in *Figure 4.6*)

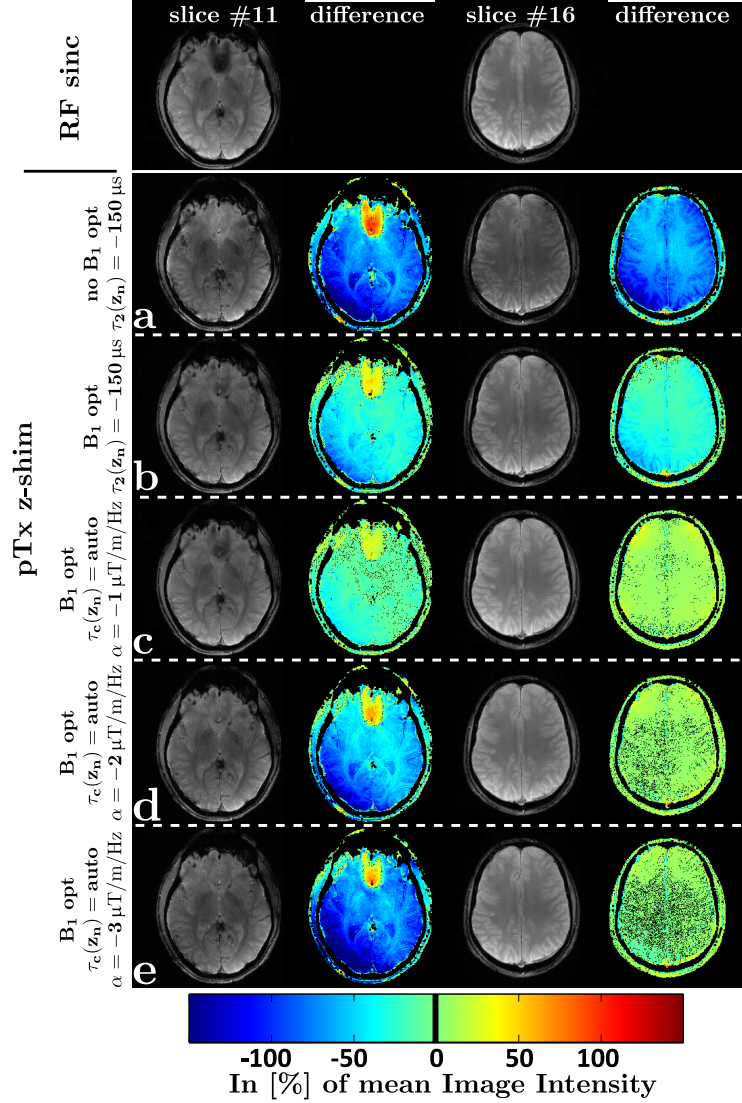


**Fig. 4.5:** Detailed analysis of two FLASH images with and without initial through-plane susceptibility artifacts. Difference images were calculated relative to the acquisitions using the standard RF sinc pulse and are normalized to the mean image intensity, respectively. The SNR loss coming along with the time-delayed excitation is quantitatively captured by the mean intensity loss. Similar to *Figure 4.3* the simultaneous pTX z-shim includes the following modes: **a** The original approach without  $B_1$  optimization and a global static delay of  $-150 \mu\text{s}$  (mean intensity loss for slice 11/slice 16:  $-40.0\%$  /  $-39.0\%$ ). **b** with  $B_1$  inhomogeneity mitigation ( $-21.5\%$  /  $-18.7\%$ ). **c-e** Including  $B_1$  inhomogeneity correction and slice specific determination of the time delays with varying  $\alpha$  values ( $\alpha = 1$  :  $-9.9\%$  /  $+8.0\%$ ;  $\alpha = 2$  :  $-33.9\%$  /  $+5.4\%$ ;  $\alpha = 3$  :  $-43.3\%$  /  $+1.8\%$ ).

**Table 4.1:** Performance analysis of multi-slice FLASH images acquired with pTx z-shim approach. Signal recovery performance is measured in percent of recovered voxels  $< 10\%$  of the normalized maximum intensity in standard RF sinc images. The image quality loss relative to the standard RF excitation in the remaining brain areas is further estimated by the SSD, STD of differences and mean image intensity loss. The SSD and STD values were normalized to the highest value per subject, respectively. The mean intensity loss was calculated outside the recovery regions with respect to the RF sinc images.

pTx z-shim approach		Subject			Average
		1	2	3	
Recovered signal in [%]	No $B_1$ opt, $\tau = -150 \mu\text{s}$	45.8	43.5	43.9	44.4
	$B_1$ opt, $\tau = -150 \mu\text{s}$	36.5	42.4	43.1	40.7
	$B_1$ opt, $\tau = \text{auto}$ , $\alpha = -1 \mu\text{T/m/Hz}$	41.7	45.8	41.2	42.9
	$B_1$ opt, $\tau = \text{auto}$ , $\alpha = -2 \mu\text{T/m/Hz}$	44.7	48.0	47.4	46.7
	$B_1$ opt, $\tau = \text{auto}$ , $\alpha = -3 \mu\text{T/m/Hz}$	47.9	50.5	48.9	49.1
SSD	No $B_1$ opt, $\tau = -150 \mu\text{s}$	1.00	1.00	1.00	1.00
	$B_1$ opt, $\tau = -150 \mu\text{s}$	0.40	0.31	0.49	0.4
	$B_1$ opt, $\tau = \text{auto}$ , $\alpha = -1 \mu\text{T/m/Hz}$	0.24	0.07	0.20	0.17
	$B_1$ opt, $\tau = \text{auto}$ , $\alpha = -2 \mu\text{T/m/Hz}$	0.67	0.33	0.69	0.56
	$B_1$ opt, $\tau = \text{auto}$ , $\alpha = -3 \mu\text{T/m/Hz}$	0.89	0.59	0.99	0.82
STD of differences	No $B_1$ opt, $\tau = -150 \mu\text{s}$	1.00	1.00	0.98	0.99
	$B_1$ opt, $\tau = -150 \mu\text{s}$	0.66	0.68	0.79	0.71
	$B_1$ opt, $\tau = \text{auto}$ , $\alpha = -1 \mu\text{T/m/Hz}$	0.64	0.55	0.65	0.61
	$B_1$ opt, $\tau = \text{auto}$ , $\alpha = -2 \mu\text{T/m/Hz}$	0.78	0.73	0.88	0.80
	$B_1$ opt, $\tau = \text{auto}$ , $\alpha = -3 \mu\text{T/m/Hz}$	0.86	0.82	1.00	0.89
Mean intensity loss in [%]	No $B_1$ opt, $\tau = -150 \mu\text{s}$	-31.5	-40.7	-32.8	-35.0
	$B_1$ opt, $\tau = -150 \mu\text{s}$	-20.4	-22.9	-20.1	-21.1
	$B_1$ opt, $\tau = \text{auto}$ , $\alpha = -1 \mu\text{T/m/Hz}$	-13.2	-15.3	-5.6	-11.4
	$B_1$ opt, $\tau = \text{auto}$ , $\alpha = -2 \mu\text{T/m/Hz}$	-28.6	-25.8	-19.0	-24.5
	$B_1$ opt, $\tau = \text{auto}$ , $\alpha = -3 \mu\text{T/m/Hz}$	-33.3	-38.5	-27.6	-33.1

against the other brain areas. Here, the fMRI coverage in through-plane susceptibility-affected areas could be significantly increased by the usage of the simultaneous z-shim approach (up to 70%). At the same time the BOLD coverage in the remaining brain areas got either slightly reduced or enlarged.

## 4.5 Discussion

In this study a new method is proposed which reduces through-plane susceptibility-induced signal loss in gradient-echo-based sequences. The method extends the previous work of *Deng et al.* [8] and is demonstrated to recover more signal while the image quality is less compromised at the same time. The final method can be used in a fully automated way and is integrated into a pulse sequence on a clinical pTx scanner.

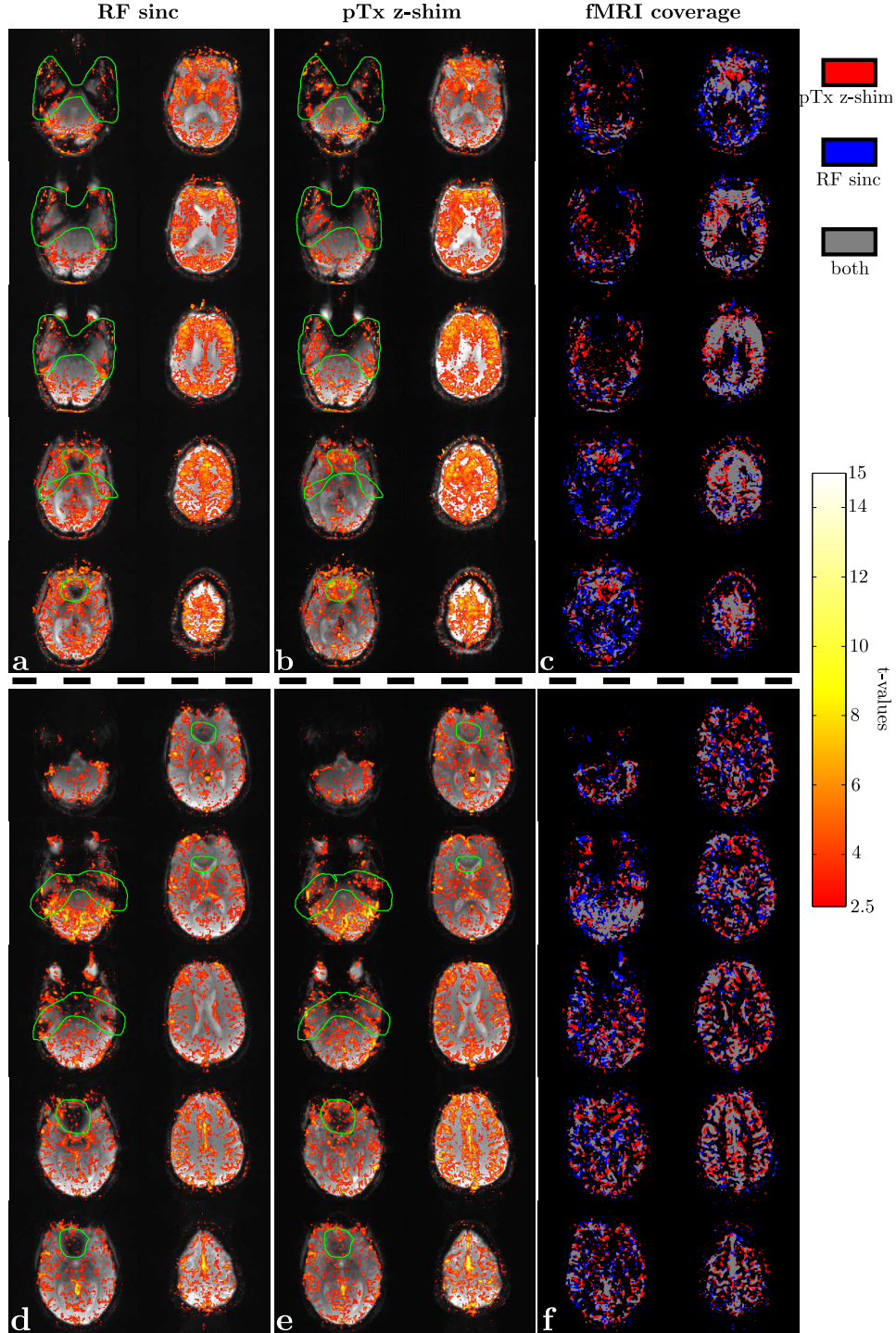


**Fig. 4.6:** Breath-hold BOLD fMRI results of subject 1 (top) and subject 2 (bottom) for  $t$ -values  $> 2.5$ . Results were obtained by using the standard RF sinc (a,d) and the proposed pTx z-shim approach with **B1** mitigation and automatic time-delay determination (b,e). The green overlaid contour lines show the manually selected ROIs, where most of through-plane susceptibility artifacts occur. Differences in the spatial BOLD activations are further highlighted in c,f: Red colored areas indicate BOLD activation solely achieved with pTx z-shim and blue areas with RF sinc excitation, respectively. Grey color encodes areas of common activation.

**Table 4.2:** Average change in the spatial fMRI BOLD activation coverage for  $t > 2.5$  with the proposed simultaneous pTx z-shim approach. Values are stated in percent relative to the results of the standard RF sinc excitation pulse for the manually selected ROI and the other remaining brain areas ( $\overline{\text{ROI}}$ ), respectively.

	Subject			Average
	1	2	3	
Recovery region (ROI)	+72.5%	+42.3%	+58.2%	+57.6%
Outside recovery region ( $\overline{\text{ROI}}$ )	-5.9%	+9.6%	+8.8%	+4.2%

An RF pulse optimization approach was introduced towards mitigating  $B_1$  inhomogeneities in the time-delayed RF excitation. For this purpose, the default RF shimming approach was extended to support RF-transmit-channel-specific time-delayed waveforms on the basis of the well-known spatial domain design approach. The FLASH experiments revealed that  $B_1$  shading effects could be visibly reduced compared to the original approach, but can also partially reduce the signal recovery level (*Figure 4.5a* vs. *Figure 4.5b*). This is probably due to the adaptation of the magnitude levels of the arbitrary time-delayed RF sinc waveforms to improve the overall  $B_1$  homogeneity. Thus, the impact of those RF coils being responsible for the local signal recovery can be decreased. Furthermore, it was observed that the  $B_1$  mitigation performance gets generally worse with increasing time-delays, see *Figure 4.2* and slice 11 in *Figure c-e*. The more the RF excitation is delayed, the farther is its distance relative to excitation k-space center. Hence, the possibility to adjust the weight of the respective RF coil sensitivity profile is limited to higher spatial frequencies and cannot longer compensate low frequency  $B_1$  shading, which is indicated by the fall-off of the second transmitter sensitivity profile (*Figure 4.4* vs. *Figure 4.5c-e*).

The simultaneous z-shim approach was extended by an automated time-delay determination method and aims to adapt the individually required pre-compensation phase to the susceptibility-provoked signal dephasing. Similar to [81, 157] the prevailing  $B_0$  maps were used as a rough linear predictor for estimating the through-plane field gradient  $G_s(x, y; z_n)$  for each slice. The coil-specific time-delay was then determined on the basis of the maximum dephasing gradient value within the corresponding region of interest  $\mathbf{W}_{S_c}$ . Here, the proposed delay-determination is practically limited to a single delay per slice due to the global spatial coverage of the coil sensitivity profiles (*Figure 4.4*). This is certainly restraining the intra-slice performance because of the missing adaption to different local through-plane main field variations. The signal-recovery performance is likely to improve with local transmit coil arrays with more distinct sensitivity profiles. However, at this time-point there is no commercially available MR scanner system with multiple local transmit channels for clinical use available, yet. To improve the robustness of the method, the histogram of the gradient values in  $\mathbf{W}_{S_c}$  can be analyzed to estimate the major dephasing component being less sensitive to outliers. The tailoring of RF pulse delays to the maximum field gradient alone is critical and relies on sufficient spatial filtering of the  $B_0$  map. Still, areas without through-plane  $B_0$  inhomogeneity can be affected by the application of phase gradients. Strategies to determine the need for z-shimming can help to enhance the adjustment of the time-delays. The introduction of a  $B_0$  map threshold can be exemplary used to indicate whether an effective z-shimming is required for an imaging slice. Especially in dorsal slices with negligible  $B_0$  artifacts, this strategy can help to avoid potential degradation of the image quality. Further, k-means clustering or advanced thresholding algorithms can be used to improve the definitions of  $\mathbf{W}_{S_c}$ , which is

important for matching the most suited transmit coil with the critical through-plane main field gradients.

One general drawback of the simultaneous z-shim method remains in the loss of image signal intensity with increasing time-delays. This effect was already reported in [8] and is mainly due to the degradation of the slice profile resulting from the superposition of shifted and un-shifted RF pulses (*Figure 4.2a*). The slice profile perturbation becomes worse with higher time-delays and thus the SNR loss correlates linearly with the parameter value  $\alpha$  (*Figure c-e*). In contrast to the work by *Deng et al.*, a global loss in SNR was observed since two whole-body RF transmit channels with rather global sensitivity profiles in the brain were used. On the other hand, our approach limits this effect to the required minimum by the adequate choice of slice-individual delays. Further, it offers an efficient signal recovery, short RF pulse durations and a simple and fast implementation, which is also important for clinical applicability. Based on both clinical multi-slice FLASH and breath-hold BOLD fMRI experiments the beneficial effects of the proposed methods were demonstrated.

Within the FLASH study, the linear estimate of  $G_s(x, y; z_n)$  with a slope of  $\alpha = -2 \mu\text{T/m/Hz}$  was found to provide the best compromise between image quality preservation and local signal recovery level (*Table 4.2*, *Figure 4.3* and *Figure 4.5*). Across all subjects, 47% of the signal could be recovered while limiting the signal intensity loss and inhomogeneity to an adequate level. Compared to the original approach with manual optimization of the time-delays, the automated time-delay determination provides approximately the same recovery level, but in combination with the  $B_1$  inhomogeneity mitigation significantly better overall image quality. The proposed simultaneous pTx z-shim approach was applied in a breath-hold BOLD fMRI study with 90-degree RF excitation flip angle level. Generally, a good performance of the small-tip-angle approximation used in the RF pulse optimization was observed for designing the large-tip-angle excitation pulses, which is in line with the early observations of [42]. For all subjects, the pTx z-shim approach helped to significantly increase the spatial coverage of BOLD activation maps up to 72% within the through-plane susceptibility affected brain regions compared to the default RF sinc excitation. However, the increased BOLD coverage in signal void areas came along with partial activation loss in the surrounding areas. Particularly, a strong weighting towards signal recovery was recognized by visual inspection in relevant slices of subject 1 (*Figure 4.6b*, lower left slice). Here, the chosen parameter value of  $\alpha = -2 \mu\text{T/m/Hz}$  is likely to overestimate the through-plane magnetic field variations. In fact, the study in [157] found  $\alpha = -1 \mu\text{T/m/Hz}$  to offer the best functional relationship and results in combination with spectral-spatial RF pulses. However, insufficient signal recovery was found, when combining this value with the proposed approach (*Table 4.1*). As indicated in [14], the used assumption of [81] may generally not be valid to predict accurately the through-plane dephasing for all slices. The relationship was shown to exist for regions above air space, but not necessarily for regions in the same z-plane as air space. Regarding the residual brain areas, the activation coverage could be maintained or even slightly increased (see *Table 4.2*). The loss in global SNR as observed in the FLASH experiments was not found to noticeably impair the final BOLD contrast. This is in line with previous studies analyzing the fMRI performance with respect to parallel imaging techniques [159, 160]. It was shown that the BOLD is not necessarily reduced by the loss of image SNR, but is mainly limited by the temporal SNR and physiological noise. However, a more thoroughly study is required to confirm these observations for the pTx z-shim approach.

In conclusion, a fully automated simultaneous z-shim approach was presented to recover local signal in gradient-echo-based sequences being impaired by through-plane susceptibility artifacts. The approach includes short RF pulse durations, a robust design for arbitrary

flip angle levels and is based on a time-delayed RF excitation on separate RF excitation coils. Thus, a pre-compensating phase along the slice-profile can be imposed to cancel out signal-dephasing. This approach was extended to improve both the signal-recovery and image quality preservation. The proposed methods take advantage from the prevailing  $B_1$  and  $B_0$  maps information to optimize the time-delayed RF excitation pulse towards  $B_1$  inhomogeneity mitigation and an appropriate slice-individual pre-compensation phase. Based on these optimized time-delayed RF pulses, clinical multi-slice FLASH and breath-hold BOLD fMRI experiments were pursued on a commercially available clinical pTx scanner system to evaluate their performance. Although, the method is generally accompanied with SNR penalties, it was shown to recover 47% of the signal and to improve 57% of the BOLD activation coverage within areas of initially noticeable signal dropouts. Furthermore, the straight-forward and fast implementation enables practicability for clinical routine. An application to systems with more TX channels with more focused RF coil sensitivities is of high interest.





## Shaped Saturation with pTx

### 5.1 Shaped Saturation with Inherent RF-Power-Efficient Trajectory Design

This section contains methods & principles that were accepted for publication in:

R. Schneider, M. Gebhardt, J. Haueisen, and J. Pfeuffer. Target-pattern-informed variable-density trajectory design for low-sar pulse design in parallel transmission. In *Proceedings of the 21st Annual Meeting of the ISMRM, Salt Lake City, USA*, page 4261, 2013.

R. Schneider, J. Haueisen, and J. Pfeuffer. Shaped saturation with inherent radiofrequency-power-efficient trajectory design in parallel transmission. *Magn Reson Med*, 72:1015–1027, 2014. ISSN 1522-2594. doi: 10.1002/mrm.25016. URL <http://dx.doi.org/10.1002/mrm.25016>.

R. Schneider, J. Haueisen, and J. Pfeuffer. Shaped saturation with rf power efficient 2d spatially selective spiral design in parallel transmission. In *Proceedings of the 22nd Annual Meeting of the ISMRM, Milan, Italy*, page 1463, 2014.

#### 5.1.1 Introduction

In clinical MR imaging the localized suppression of unwanted signals is often necessary to avoid their interference with the ROI. Typical applications in spectroscopy are the fat signal suppression in the vicinity of the prostate [161] or the suppression of the scalp cap [162]. In sagittal spine imaging the signal of the moving inner organs is often suppressed to reduce motion and aliasing artifacts along the phase-encoding direction. To date the localized signal suppression is commonly realized by the application of multiple saturation slabs. These are most often manually arranged to fit roughly the desired anatomy. However, this approach has several disadvantages in its clinical practicality: The manual arrangement of the slabs can be very time consuming and still lacks anatomical accuracy. Moreover, the usage of many saturation RF pulses can also significantly increase the SAR and TR, which further limits the imaging performance.

A suitable approach for anatomically shaped signal suppression would be the application of multidimensional spatially selective RF pulses [42]. This class of pulses can excite and saturate arbitrarily shaped patterns, but typically requires long RF pulse durations and is

very sensitive to off-resonance effects. The use of parallel transmit technology has proven very beneficial in overcoming these drawbacks [2, 15]. The incorporation of the different RF coil sensitivities and prevailing off-resonance information into the RF pulse design process allows not only the compensation of  $B_1$  and  $B_0$  inhomogeneities, but also the shortening of multidimensional RF pulses. Yet, the design of multi-dimensional spatially selective saturation RF pulses remains challenging as the required high FA level of  $\geq 90^\circ$  is difficult to achieve within the given RF hardware and SAR limits. Basically three groups of methods have been established to help to stay within these limits: Firstly, different variable-rate selective excitation (VERSE) based methods [85, 163] were introduced, which in general ‘time-dilate’ the local RF pulse and gradient shape where high  $B_1$  amplitudes occur. Some studies [54, 163] also redesign the RF pulse based on the elongated gradient waveforms. Secondly, regularized [4, 15] or constrained [53, 128] optimization strategies were proposed to limit the RF peak voltage and average power and/or the global and local SAR during the RF pulse optimization. Clearly, a combination of approaches from both groups is possible. However, both groups encounter the high RF hardware demands more or less a-posteriori, i.e. during the optimization or at the very end of the of RF pulse design. More favorable would be an approach which requires a-priori less RF hardware demands and SAR.

The third group considers the type and design of the underlying TX k-space trajectory, which have been shown to have a great inherent influence on the resulting RF hardware and SAR efficiency [62, 71]. Several publications [62, 63] use highly iterative methods to determine the optimal TX k-space locations, which can be computationally intensive and inefficient for clinical practice. Others provide default higher sampling density [71] or a slower sampling rate [70] near k-space center, which can already significantly improve performance. The a-priori knowledge of the k-space representation of the desired magnetization pattern offers further valuable information about the required RF energy deposition. The incorporation of this information into custom k-space trajectory design was reported advantageous in numerous publications [12, 16, 60, 63, 69, 124], but a detailed algorithm was not [12, 16, 63] or only partially [69] stated or was solely used in combination with iterative approaches [60, 63, 124].

A novel variable density k-space trajectory design is proposed, which combines the Fourier transform (FT) of the desired target magnetization pattern with a spatial spectral window function. The resulting TX k-space sampling distribution metric provides the basis for the geometric sampling density of the k-space trajectory, but also determines the sampling velocity. The new design is shown to be inherently RF hardware efficient, which can be beneficial regarding global and local SAR considerations. Thus, RF pulse optimization can be used more efficiently, e.g. for higher RF pulse acceleration. Moreover, additional RF pulse post-processing or design iterations can be omitted. The method is implemented and evaluated for different applications with an anatomically shaped saturation using a two-dimensional selective spiral RF pulse. First, within a simulation study the method’s RF hardware efficiency and global and local SAR performance are analyzed as a function of different TX accelerations factors and different spatial fidelities. Second, human in-vivo experiments were performed to further validate the proposed trajectory design. In all simulations and experiments the performance is also compared to two state-of-the-art TX trajectory designs, i.e. using an equidistant k-space sampling density with reduced sampling velocity near k-space center [70] and using a variable density k-space sampling density [71]. For the first time human in-vivo shaped saturation experiments in the brain and body on the basis of spatially selective pulses were achieved. Preliminary work has been presented in [30].

### 5.1.2 Theory

#### *Target Pattern Driven Variable Density Trajectory Design*

The target pattern driven (TD) k-space trajectory design proposed in the following, aims at providing an inherent RF hardware efficient RF pulse design. The design takes advantage from the a-priori knowledge of the pre-defined target magnetization pattern  $\mathbf{m}_{\mathbf{W}}$  in the region of interest  $\mathbf{W}$  with desired excitation resolution  $\mathbf{m}_{res}$ . The k-space representation of  $\mathbf{m}_{\mathbf{W}}$  can be obtained via the FT. Moreover, the required energy distribution in k-space is indicated by the squared magnitude of the FT of  $\mathbf{m}_{\mathbf{W}}$  within excitation k-space limits  $\pm \mathbf{k}_{max}/2 = \pm 1/(2\mathbf{m}_{res})$ :

$$E(\mathbf{k}) = \left| \int_{-\infty}^{+\infty} \mathbf{m}_{\mathbf{W}} e^{-i\mathbf{k}\mathbf{r}} d\mathbf{r} \right|^2 \quad \text{with } |\mathbf{k}| \leq \mathbf{k}_{max}/2, \quad (5.1)$$

where  $\mathbf{r}$  and  $\mathbf{k}$  are the spatial and k-space coordinates and  $E(\mathbf{k})$  the target pattern's energy at  $\mathbf{k}$ , respectively. This equation may be discretized in  $\mathbf{k}$ , forming a matrix  $\mathbf{E}$  describing the energy distribution in k-space. Thus, by putting more k-space trajectory samples in k-space locations of higher energy and fewer samples in k-space areas with negligible energy, the potential RF power expense should decrease. However, only subtle improvements or even higher RF power deposition was observed, if the k-space trajectory sampling density is adapted to the pure normalized density of Equation 5.1:  $\mathbf{E}$  is typically dominated by the prominent peak at the k-space center, which corresponds to the mean spatial magnetization of the target pattern. Then  $\mathbf{E}$  declines rapidly to the outer k-space regions, where all spatial details are encoded. The magnitude of the center peak compared to the outer k-space values can be 10 to 1000 times higher. Thus, an arbitrary k-space trajectory would strongly concentrate at lower k-space frequencies, when its' relative sampling density is matched to  $\mathbf{E}$ . Higher spatial frequency components are only sparsely covered by few samples. Based on these few samples in outer k-space, the subsequent RF pulse optimization process makes efforts to realize all the spatial details to be encoded. This effect is likely to counteract the hypothetical RF power savings near the k-space center. Similar observations about the suboptimal positioning of k-space samples based on  $\mathbf{E}$  alone has been already reported in [60, 124], which use a k-space thresholding strategy to determine potential k-space positions. To overcome this issue, a local weighting method is introduced, which weights  $\mathbf{E}$  according to the excited area/volume, but also to the available  $B_1$  sensitivity. In image acquisition, density weighted imaging techniques have been established to offer an optimized signal to noise ratio and spatial fidelity [127]. This approach was transferred to the TX case and specify the density weighting only to the relevant k-space regions. For this purpose, the energy distribution is firstly divided into  $N_{seg}$  disjunct k-space energy segments, where each segment  $\mathbf{E}_{seg\,n}$  contains one so called 'energy hotspot', i.e. a local energy elevation in TX k-space:

$$\begin{aligned} \mathbf{E} &= \bigcup_{n=1}^{N_{seg}} \mathbf{E}_{seg\,n} \quad \text{with} \\ \mathbf{E}_{seg\,n} \cap \mathbf{E}_{seg\,m} &= \emptyset \quad \text{for } n \neq m \quad \text{and } n, m \in N_{seg}. \end{aligned} \quad (5.2)$$

The segmentation of  $\mathbf{E}$  can be obtained by e.g. using a maximum/minimum detection algorithm. To increase the sensitivity of the detection process for the outer k-space regions,

the peak at the k-space center can be masked out by analyzing the zero-mean normalized target pattern. Consequently, a k-space segment would contain one local energy maximum. Its borders can be defined by the common local minima to the adjacent segments, respectively. Secondly, the weight of each k-space energy segments is adopted to a spatial spectral window function  $H(\mathbf{k})$ . Precisely, the basic envelope of the normalized energy segments is fitted to the shape of  $H(\mathbf{k})$ . The properties of  $H(\mathbf{k})$  are chosen to offer an adequate compromise between the resulting RF power efficiency and spatial fidelity. A Hanning window was found to be a good choice for handling this tradeoff [127, 164].

$$\begin{aligned} \mathbf{E}' &= \bigcup_{n=1}^{N_{seg}} \mathbf{E}'_{seg\ n} = \bigcup_{n=1}^{N_{seg}} \frac{\mathbf{E}_{seg\ n}}{\max(\mathbf{E}_{seg\ n})} H(\mathbf{k}_{local\ max\ n}) \text{ with} \\ H(\mathbf{k}) &= \prod_{d=1}^{D=3} \frac{1}{2} (1.2 + \cos(\frac{\pi}{\alpha} \frac{\mathbf{k}(d)}{\mathbf{k}_{max}(d)/2})) \text{ and } \alpha > 0, \end{aligned} \quad (5.3)$$

where  $\mathbf{E}'$  and  $\mathbf{E}'_{seg\ n}$  are the weighted k-space energy distribution and  $n$ th segment, respectively,  $\mathbf{k}_{local\ max\ n}$  the k-space coordinates of the local energy hotspot of the  $n$ th k-space energy segment with spatial dimension  $D$  and  $\alpha$  the width of the Hanning window function. Note that the parameterization for  $H(\mathbf{k})$  was chosen to provide a minimal weighting of 0.1. For  $\alpha < 1$  the spatial spectral window function was further limited to the main lobe. As an alternative approach a piecewise defined filter function can be determined on the basis of  $H(\mathbf{k})$  and the borders of  $\mathbf{E}_{seg\ n}$  and is applied once to the whole TX k-space.

Based on this modified k-space energy distribution  $\mathbf{E}'$  the geometry of the TX k-space trajectory and also its sampling density were then determined with the algorithm described in [127]. It ensures that denser sampling and increased coverage of the TX k-space trajectory is considered where higher energy density values occur.

Clearly, the tradeoff between the spatial response function and the expected RF power deposition based on the TX k-space trajectory is mainly determined by  $\alpha$ : The focus of the trajectory design on the central k-space peak of  $\mathbf{m}_W$  is the stronger the smaller the  $\alpha$  value is set. The optimal weighting may depend on the prevailing  $B_1$  sensitivities, the MR scanner system and its hardware specifications, the size, orientation and position of the desired magnetization pattern and the k-space trajectory type [67, 68]. A linear function to define a proper window width considering the interaction of the average  $B_1$  magnitude and pattern size was found empirically in a first approximation:

$$\alpha = \overline{\sum_{c=1}^C |\tilde{\mathbf{S}}_c|_{\mathbf{m}_W > 0}} \cdot \left( \frac{\beta}{A(\mathbf{m}_W > 0)} + \gamma \right), \quad (5.4)$$

with  $\tilde{\mathbf{S}}_c$  being the  $c$ th RF coil sensitivity profile of  $C$  RF transmit channels,  $\overline{\sum_{c=1}^C |\tilde{\mathbf{S}}_c|_{\mathbf{m}_W > 0}}$  the overall mean  $B_1$  magnitude within the inner-volume (parts of  $\mathbf{m}_W$  that shall be excited),  $A(\mathbf{m}_W > 0)$  the size of the inner-volume part of  $\mathbf{m}_W$  in square / cubic meters and  $\beta, \gamma$  the functional parameters to be empirically determined. This function may capture fluctuations of the pattern size and varying average  $B_1$  magnitude due to the changed position and orientation of the target pattern and different subjects. This relation is independent from the chosen TX acceleration factor or field of excitation. To find a proper parameterization of Equation 5.4 the following procedure is proposed and can be automatically calibrated for

a trajectory type on a scanner system: Based on  $B_1$  and  $B_0$  maps of different anatomical locations and subjects, multiple RF pulses are designed with varying  $\alpha$  values for target patterns of different size and shape. For each case an optimal  $\alpha$  value is chosen to provide a sufficient ratio between spatial accuracy and RF power expense. Finally, the parameters  $\beta$  and  $\gamma$  are fitted via linear regression to the optimally determined  $\alpha$  values. This procedure can be easily automatized to require solely a few  $B_1$  and  $B_0$  maps datasets of different anatomical locations of a group of subjects per MR scanner system.

### *TD Design for a 2-D Spiral Trajectory*

The TD k-space trajectory design approach described above was now further refined for 2-D spiral trajectories. A general description of a variable density spiral  $k(t)$  is [130]:

$$\begin{aligned} k(t) &= \tau(t)e^{i\phi(t)} \text{ with } t \in [0, T_{pulse}] \quad k_{max} \geq \tau(t) \geq 0 \text{ and} \\ [k_x(t) \ k_y(t)] &= [\text{real}(k(t)) \ \text{imag}(k(t))] , \end{aligned} \quad (5.5)$$

where  $\tau(t)$  and  $\phi(t)$  are the temporal evolution of the spiral radius and phase, respectively, and  $T_{pulse}$  the total RF pulse / gradient waveform duration. In the TX case  $\tau(t)$  and  $\phi(t)$  are monotonically decreasing functions. The corresponding gradient waveforms within hardware limits were obtained via the time-optimal design algorithm of [91].

Here the application of the TD method can be simplified since the spiral design depends only on one dimensional quantities. Thus, the 2-D k-space was reduced in a rotationally invariant manner prior to the energy density metric  $\mathbf{E}'$  computation, i.e. taking the mean magnitude along the angular coordinate direction after a polar coordinate transform. The resulting energy density is a vector describing the energy distribution from k-space center to  $k_{max}$  and is further denoted as  $\mathbf{E}'_{spiral}$ . Note that in this case the vectors  $\mathbf{m}_{res}$  and consequently  $\mathbf{m}_{max}$  are also one dimensional quantities and  $D = 1$  in Equation 5.3.

Based on  $\mathbf{E}'_{spiral}$  one can think of three different TD designs: First, the distribution of the spiral turns can be arranged according to  $\mathbf{E}'_{spiral}$ . This approach (TD<sub>traj</sub>) basically satisfies the spatial response function of  $H(\mathbf{k})$ . For that purpose solely, the temporal trend of  $\tau(t)$  has to be adjusted to the density metric  $\mathbf{E}'_{spiral}$  [127], whereas  $\phi(t)$  is linearly decreasing. The second design (TD<sub>samp</sub>) pursues the effective distribution of sampling points in k-space based on  $\mathbf{E}'_{spiral}$  and fulfills the RF power related issues of the design. The computation of the spiral trajectory is similar to the TD<sub>traj</sub> case, but  $\mathbf{E}'_{spiral}$  has to be re-weighted prior to the determination of  $\tau(t)$ . More precisely, the varying velocity of  $\tau(t)$  sampling through k-space has to be pre-compensated when designing gradient waveforms with maximum slew-rate. Based on [87] the relative and steady traversing speed  $\tau'(t)$  from outer k-space to k-space center can be approximated via

$$\tau'(t) = \frac{\partial \tau(t)}{\partial t} = \begin{cases} \left( \sqrt{\frac{3s_m \gamma}{k_{max}(2\pi N_{turns})^2}} \right)^{\frac{2}{3}} \cdot t^{-\frac{1}{3}} \propto t^{-\frac{1}{3}} & \text{(slew-rate limited case)} \\ \sqrt{\frac{4g_m \gamma}{k_{max}(2\pi N_{turns})}} \cdot t^{-\frac{1}{2}} \propto t^{-\frac{1}{2}} & \text{(amplitude limited case)} \end{cases} \quad (5.6)$$

with  $t = [T_{pulse}, 0]$  ,

with  $s_m$  being the maximum slew-rate,  $g_m$  the maximum gradient amplitude,  $\gamma$  the gyromagnetic ratio and  $N_{turns}$  the number of spiral turns. Finally, the re-weighted energy density  $\mathbf{E}_{spiral}''$  is obtained by

$$\mathbf{E}_{spiral}'' = \mathbf{E}_{spiral}' \tau'. \quad (5.7)$$

The third TD design ( $\text{TD}_{\text{traj}+\text{samp}}$ ) combines the properties of  $\text{TD}_{\text{traj}}$  and  $\text{TD}_{\text{samp}}$ , i.e. both the distribution of the spiral turns and the sampling points in k-space are arranged relative to  $\mathbf{E}_{spiral}'$ . This can be achieved by designing the gradient waveforms based on  $\text{TD}_{\text{traj}}$ , but simultaneously modulating the slew-rate  $s(t)$  in accordance with  $\tau(t)$ .

In the following, the basic algorithm is demonstrated for an elliptically shaped target pattern. *Figure 5.1* illustrates the basic procedure for determining the weighted k-space energy metric  $\mathbf{E}_{spiral}'$ , which is subsequently used to determine the final distribution of the 2-D spiral turns and/or sampling points. First, the fundamental energy distribution  $\mathbf{E}$  is calculated by transforming the spatial target pattern into k-space (*Equation 5.1*) and reducing its dimensionality in a rotational invariant manner. After that,  $\mathbf{E}$  is subdivided into six segments  $\mathbf{E}_{seg,n}$ , which basically contain one local energy elevation, respectively (*Figure 5.1a*). Finally,  $\mathbf{E}_{spiral}'$  is obtained by scaling each of the single segments to the spectral spatial window  $H(\mathbf{k})$  (*Figure 5.1b*).

### 5.1.3 Methods

#### *RF Pulse Design*

Two dimensional spatially selective spiral RF pulses were calculated in MATLAB 8.0 (MathWorks, Natick, MA) following the magnitude-least-squares approach of [15]. Concerning the shaped saturation RF pulses, this approach basically scales the RF pulses to the required high flip angle level based on a small tip angle design. Spiral RF pulse optimizations were pursued on the basis of five different k-space trajectory designs: First, using a variable-slew-rate spiral trajectory [70] with equi-distant sampling (ED). The slew rate was dynamically decreased going from the k-space maximum to the k-space center. Second, variable-density (VD) spirals were designed according to [71, 87, 165] using a constant slew rate with a density oversampling factor = 2. The third to fifth spiral trajectory designs consist of the three proposed TD trajectory designs making use of the respective target pattern information, i.e.  $\text{TD}_{\text{traj}}$ ,  $\text{TD}_{\text{samp}}$  and  $\text{TD}_{\text{traj}+\text{samp}}$ . The functional parameters  $\beta$ ,  $\gamma$  to determine the width of the Hanning weighting window (*Equation 5.4*) were calibrated by analyzing the RF pulse performance for exciting three target magnetization patterns of different spatial size at two different spatial orientations with varying  $B_1$  magnitude and FOV. For both simulations and experiments the same values were used, i.e.  $\beta = 26.5 \text{ V}/(\text{Gm}^2)$  and  $\gamma = 1.6e3 \text{ V}/\text{G}$ . The field of excitation of all trajectory designs was matched to the current FOV with a spatial excitation resolution of  $m_{res} = 7 \text{ mm}$ . Corresponding gradient waveforms were determined via the time-optimal design algorithm [91] within gradient hardware limits. RF pulse acceleration was done by stepwise reducing the number of spiral turns. To analyze the most suitable sampling strategy and to provide a reasonable comparison, all basic spiral trajectory and RF pulse specifications (i.e.  $k_{max}$ , total RF pulse duration and number of spiral turns) were kept constant for all trajectory designs.

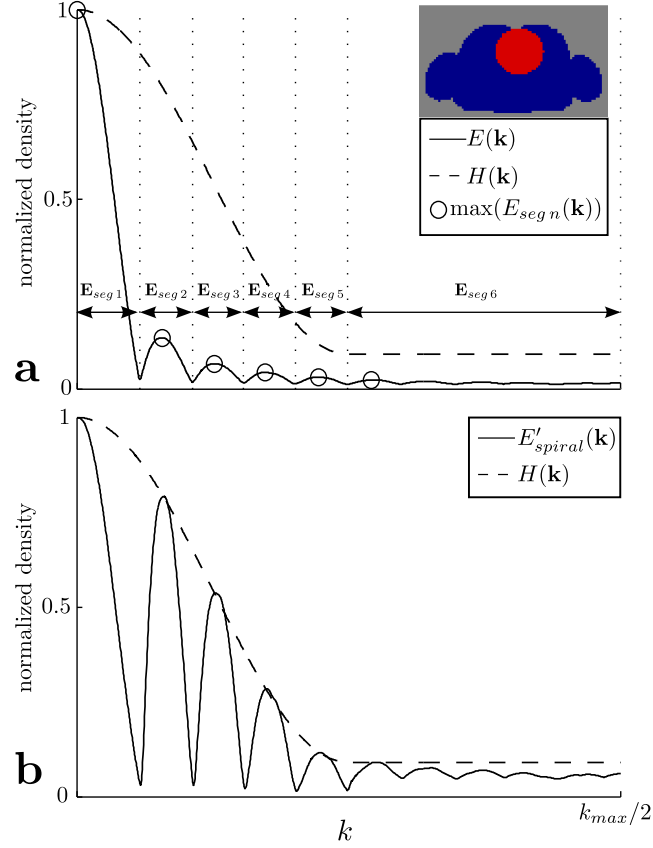


**Fig. 5.1:** Basic TD approach for 2-D spiral trajectory design of an elliptically shaped target pattern. **a** Illustration of initial k-space energy density  $E(\mathbf{k})$  from  $\mathbf{m}_W$  (upper right corner colored in red), the calculated Hanning weighting window  $H(\mathbf{k})$  with  $\alpha = 0.5$  and the six detected energy segments  $E_{segn}(\mathbf{k})$  and their borders (dotted lines). **b** Plot showing the weighted energy distribution  $E'_{spiral}(\mathbf{k})$ , where the energy segments were scaled according to  $H(\mathbf{k})$ .

### Simulations

The potential benefits of TD spiral trajectory designs have been evaluated in a simulation study for an eight channel 3 T whole body TX array ( $\omega_0 = 128$  MHz). The underlying electrodynamic field data were simulated using the anatomy model HUGO (Medical VR Studio, Lörrach, Germany) with 2 mm isotropic resolution and 32 unique tissue types as described in [72]. Shaped saturation spiral RF pulses were designed for three different anatomical locations and different target magnetization patterns (Figure 5.2): A t-spine shaped pattern was saturated in the central sagittal slice of the upper abdomen (FOV  $390 \times 340 \text{ mm}^2$ ). A ring shaped pattern was saturated in a transversal slice of the head (FOV  $340 \times 300 \text{ mm}^2$ ) masking the scalp. Finally, the heart was overlaid with an elliptical magnetization pattern in a transversal slice located in the upper abdomen (FOV  $340 \times 590 \text{ mm}^2$ ). Corresponding  $B_1$  maps, electric and magnetic fields were calculated using CST Microwave Studio (CST AG, Darmstadt, Germany).

RF pulses were optimized [15] for all three target pattern scenarios on the basis of the different spiral trajectory designs, i.e. ED, VD,  $\text{TD}_{\text{traj}}$ ,  $\text{TD}_{\text{samp}}$  and  $\text{TD}_{\text{traj+samp}}$  (see above for definition). Different metrics were assessed to compare the performance of the resulting RF pulse waveforms: The spatial fidelity was estimated via the RMSE of the corresponding complex valued numerical Bloch simulation  $\mathbf{m}_{\text{est}}$  to the real defined target magnetization pattern  $\mathbf{m}_{\text{des}}$  within the region of interest  $\mathbf{W}$ :

$$RMSE = \sqrt{\|\mathbf{m}_{\text{est}} - \mathbf{m}_{\text{des}}\|_{\mathbf{W}}^2}. \quad (5.8)$$

The RF pulse efficiency regarding the RF hardware was considered via the overall maximum voltage ( $V_{\text{peak}}$ ) and the average forward RF power over all RF channels ( $RF_{\text{power}}$ ). The  $RF_{\text{power}}$  was calculated via:

$$RF_{\text{power}} = \frac{\|\hat{\mathbf{b}}_{\text{full}}\|^2}{CN_t \cdot 50 \Omega}, \quad (5.9)$$

where  $\hat{\mathbf{b}}_{\text{full}}$  contains the RF waveforms and  $N_t$  is the number of time samples. The local and global SAR were evaluated similar to [53]:

$$SAR_{\text{local}} = \max_{v \in V_{\text{all}}} \left\{ \sum_1^{N_t} \hat{\mathbf{b}}_{\text{full}}^T(t) \left( \frac{1}{N_v} \sum_{v \in V_{10\text{cc}}} \frac{\sigma_v \Delta t}{2\rho_v T_{\text{pulse}}} \mathbf{Q}_v^T \mathbf{Q}_v \right) \hat{\mathbf{b}}_{\text{full}}(t) \right\}, \quad (5.10)$$

$$SAR_{\text{global}} = \sum_1^{N_t} \hat{\mathbf{b}}_{\text{full}}^T(t) \left( \frac{1}{N_{\text{all}}} \sum_{v \in V_{\text{all}}} \frac{\sigma_v \Delta t}{2\rho_v T_{\text{pulse}}} \mathbf{Q}_v^T \mathbf{Q}_v \right) \hat{\mathbf{b}}_{\text{full}}(t), \quad (5.11)$$

where  $v$  is the voxel position in the set of voxels of the model  $V_{\text{all}}$  containing  $N_{\text{all}}$  voxels,  $N_v$  the number of voxels of the 10 cubic centimeter region  $V_{10\text{cc}}$ ,  $\sigma_v$  the electric conductivity at voxel position  $v$ ,  $\rho_v$  the mass density at voxel position  $v$ ,  $T_{\text{pulse}}$  the total RF pulse duration with sample period  $\Delta t$  and  $\mathbf{Q}_v$  the electric field sensitivity matrix of all RF channels at voxel position  $v$ . The RF pulse  $\hat{\mathbf{b}}_{\text{full}}(t)$  is arranged as an  $C \times 1$  vector of  $N_t$  complex values.

The excitation performance was further analyzed as a function of different TX acceleration factors up to  $R = 4$  and different spatial fidelity levels. The latter was controlled by the stepwise increase of the Tikhonov regularization parameter and thus global damping of the RF energy [15]. In total 1500 different cases were simulated.

### Experiments

The experimental verification of the beneficial effects of the method proposed was done in human in-vivo experiments on a 3 T MAGNETOM Skyra system equipped with two independent and integrated whole body transmit RF channels (Siemens AG, Healthcare Sector, Erlangen, Germany). The two complex  $B_1$  maps of the respective RF coils were estimated using a presaturation TurboFLASH sequence [99]. The prevailing off-resonance information, i.e.  $B_0$  map, was acquired with a multi-echo approach similar to [106]. A fat-water in-phase  $B_0$  map was calculated and incorporated into RF pulse calculation [15]. Imaging



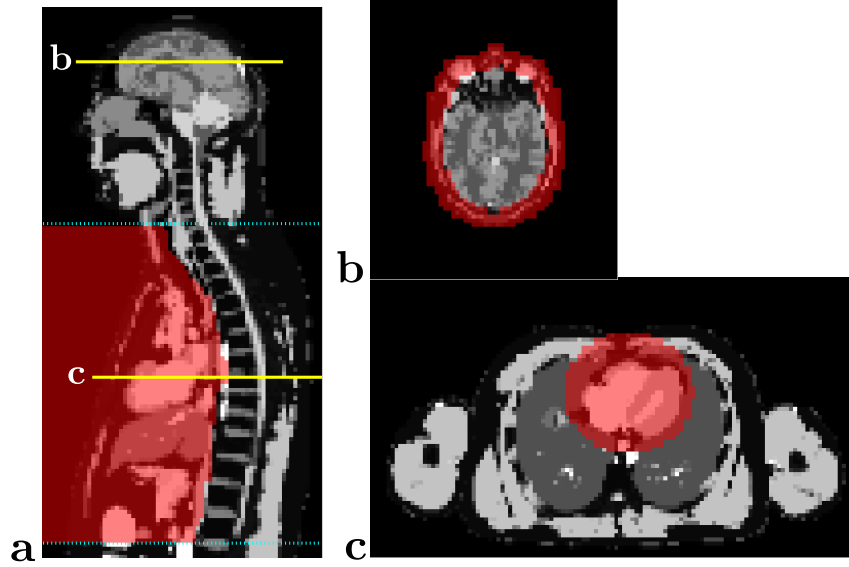


**Fig. 5.2:** Slices of the HUGO model with corresponding target patterns and their anatomical positions (overlaid in red). **a** Spine-shaped target pattern to saturate moving inner organs. **b** Scalp-shaped target pattern hypothetically saturating the fat ring of the scalp. **c** Elliptical pattern to saturate the heart.

was done at three distinctive anatomical locations similar to the simulations: A checkerboard pattern was saturated in a sagittal head slice (FOV  $240 \times 240 \text{ mm}^2$ ). Further, the heart signal was suppressed with an elliptical pattern in an axial slice (FOV  $330 \times 330 \text{ mm}^2$ ). Finally, a sagittal spine-shaped saturation was applied in the t-spine (FOV  $300 \times 300 \text{ mm}^2$ ). Images were acquired using a gradient echo sequence with matrix  $256 \times 256$ , TR 100 ms, TE 10 ms and GRAPPA acceleration factor 2. In the heart and thoracic-spine, fat saturation was applied using a spectral-selective Gaussian FATSAT method. 2-D spiral RF shaped saturation pulses were optimized on the basis of the ED, VD and  $\text{TD}_{\text{traj+ samp}}$  trajectories and for water-band only. The target flip angle was set to  $90^\circ$  and  $R = 1.4$  resulting in RF pulse durations from 7 to 10 ms (checkerboard: 7.5 ms, heart: 9.8 ms, spine: 9.7 ms). All RF pulses were regularized to stay within RF hardware limits and with controlled SAR. No special SAR handling was used in this study beyond the commercially implemented SAR supervision features on the MAGNETOM Skyra pTx system. Global and local SAR values were estimated using the virtual observer point (VOP) model described in Ref. [72], which allows a real-time calculation and supervision of sequences with high RF-duty cycle due to the high-level compression of underlying electric field models. Forward and reflected RF signals were continuously monitored using directional couplers. The online supervision and evaluation of SAR using the incoming digitized RF waveforms was done similar to Refs. [166, 167] to keep local SAR independently controlled.

### 5.1.4 Results

#### 8-Channel TX Simulations

Different characteristics of all analyzed spiral trajectory designs are summarized for the elliptical target pattern in *Figure 5.3*. The ED design has an equi-distant distribution of the spiral turns with virtually increased sampling point density at the k-space center coming along with a dynamic slew-rate reduction. However, in the sampling points histogram over the k-space radius it can be observed that the sampling weight of the k-space center is relatively low compared to the outer k-space regions. In contrast, the VD design concentrates its spiral turns strongly into the k-space center and leaves only few turns for the outer k-space regions. As a consequence, also the sampling points histogram tapers towards the spiral center. Both the ED and VD design, neither adapt their spiral turn coverage nor the sampling point density to the actual k-space representation of the target pattern. Any alignments with local energy elevations are accidental. The  $TD_{\text{traj}}$  spiral correlates well with the target pattern and shows a more balanced distribution of the spiral turns. Similar to the ED design the focus of the sampling points is not at k-space center where most of the RF energy effort is expected. The  $TD_{\text{samp}}$  design shows quite the opposite characteristics, i.e. a target-pattern-adapted distribution of its sampling points, but similar to VD, only a few spiral turns at the outer k-space. Finally, the  $TD_{\text{traj+samp}}$  trajectory combines the pattern-driven features of  $TD_{\text{traj}}$  and  $TD_{\text{samp}}$  and distributes the spiral turns and sampling points optimally according to the magnetization pattern.

Simulations were run for different target patterns, RMSE levels and TX acceleration factors resulting in the well-known L-curves. Exemplary results of the simulations are shown in *Figure 5.4* and *Figure 5.5*. The quality metrics were stated relative to the overall maximal ( $V_{\text{peak}}$ ,  $RF_{\text{power}}$ ,  $SAR_{\text{global}}$ ,  $SAR_{\text{local}}$ ) or minimal (RMSE) value of all simulations per target pattern. Generally, it can be observed that the basic trend of all metrics correlate quite well for the different scenarios. With increasing TX acceleration factor, the RF power requirements and effective SAR rise significantly and the differences between the different trajectory designs become more prominent. When analyzing the performance of the three proposed TD designs (*Figure 5.4*), the following observations can be made. The  $TD_{\text{traj}}$  design offers always the best achievable RMSE level, but mostly in conjunction with the highest RF hardware load and SAR values. In contrast, the  $TD_{\text{samp}}$  pulses have the opposite tendency. They significantly require less  $RF_{\text{power}}$  and have lower SAR, but can lack in spatial accuracy. The discrepancy between those two designs becomes larger with higher acceleration factors, but also with the spatial size of the desired target pattern, i.e. from the scalp to the heart to the spine-shaped pattern. The RF pulses being optimized on the  $TD_{\text{traj+samp}}$  trajectory again combine the properties of the other two TD design modes. Thus,  $TD_{\text{traj+samp}}$  provides high spatial accuracy with good RF and SAR efficiency (see e.g. heart shaped pattern, *Figure 5.4*). Overall  $TD_{\text{traj+samp}}$  shows superior results, especially in the gap between the L-curves of  $TD_{\text{traj}}$  and  $TD_{\text{samp}}$  (see e.g. scalp simulations of *Figure 5.4* in the range of 200 – 300% relative RMSE).

In *Figure 5.5*, the  $TD_{\text{traj+samp}}$  design is further compared with the two commonly used 2-D spiral designs, ED and VD. Regarding the overall performance, the ED k-space trajectory based RF pulses can involve considerably higher RF power, voltage and SAR metrics than VD and  $TD_{\text{traj+samp}}$ . Its' best achievable spatial accuracy decreases with the area of the target magnetization. The VD RF pulses can offer quite RF hardware efficient results (spine target, *Figure 5.5*). On the other hand the design has only moderate spatial accuracy for

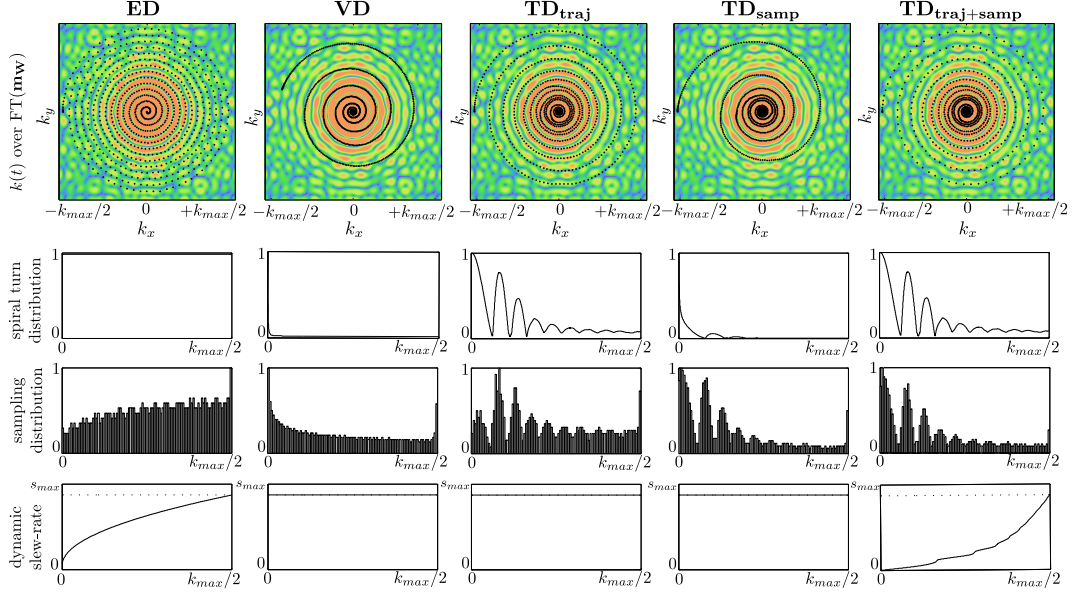


**Fig. 5.3:** Overview of different 2-D spiral trajectory designs for an elliptically shaped target pattern with  $R = 3$ . The top row shows the target pattern representation in k-space  $E(\mathbf{k})$  overlaid with the respective 2-D spiral trajectory. Note that the contrast of  $E(\mathbf{k})$  was scaled and windowed for better illustration. Further specifications of the trajectory designs over TX k-space are shown in rows two to four, i.e. the spiral turn distribution, the sampling distribution histogram and the slew-rate course. Clearly, the  $\text{TD}_{\text{traj}}$  and  $\text{TD}_{\text{traj+samp}}$  design align well with the local energy elevations of  $E(\mathbf{k})$ . The  $\text{TD}_{\text{traj+samp}}$  design also offers the optimized sampling points distribution of  $\text{TD}_{\text{samp}}$ .

the medium (heart) and small (scalp) sized target pattern, which can be clearly noticed by the right shift of the whole L-curve (scalp target, *Figure 5.5*) compared to the others. As stated above the  $\text{TD}_{\text{traj+samp}}$  k-space trajectory shows in no case significant limitations in the spatial fidelity, i.e. no noteworthy right shift of the L-curve. The  $\text{TD}_{\text{traj+samp}}$  design outperforms the other trajectory designs in the resulting RF hardware efficiency, which is most often accompanied with a lower global and local SAR. Only for the scalp target pattern, higher global and local SAR values can be observed compared to the VD design despite the lower RF power and voltage metrics. However, note that the achievable excitation accuracy of the VD design lies far beyond that of the other two designs.

Exemplary Bloch simulation results of *Figure 5.5* were selected in *Figure 5.6* for a more detailed analysis in image space. In each target pattern scenario the RF pulse designs were matched to have an identical RMSE level at  $R = 3$ . Although the RMSE metrics are numerically equal, noticeable differences in their spatial response can be observed: For both ED- and VD-based RF pulses ‘bumpy’ aliasing artifacts occur in the outer volume of the scalp- and heart-shaped pattern (*Figure 5.6b*). Moreover, stripe artifacts are visible for the spine target pattern. In contrast, the  $\text{TD}_{\text{traj+samp}}$  RF pulses show a quite smooth and less noisy magnetization profile. When analyzing the RMSE metrics for the inner- and outer-volume separately, it can be generally observed that ED offers numerically the best outer-volume suppression, but worst magnetization performance. The VD RF pulses typically show the smallest error in the inner-volume, but at cost of increased signals in the outer-volume. The

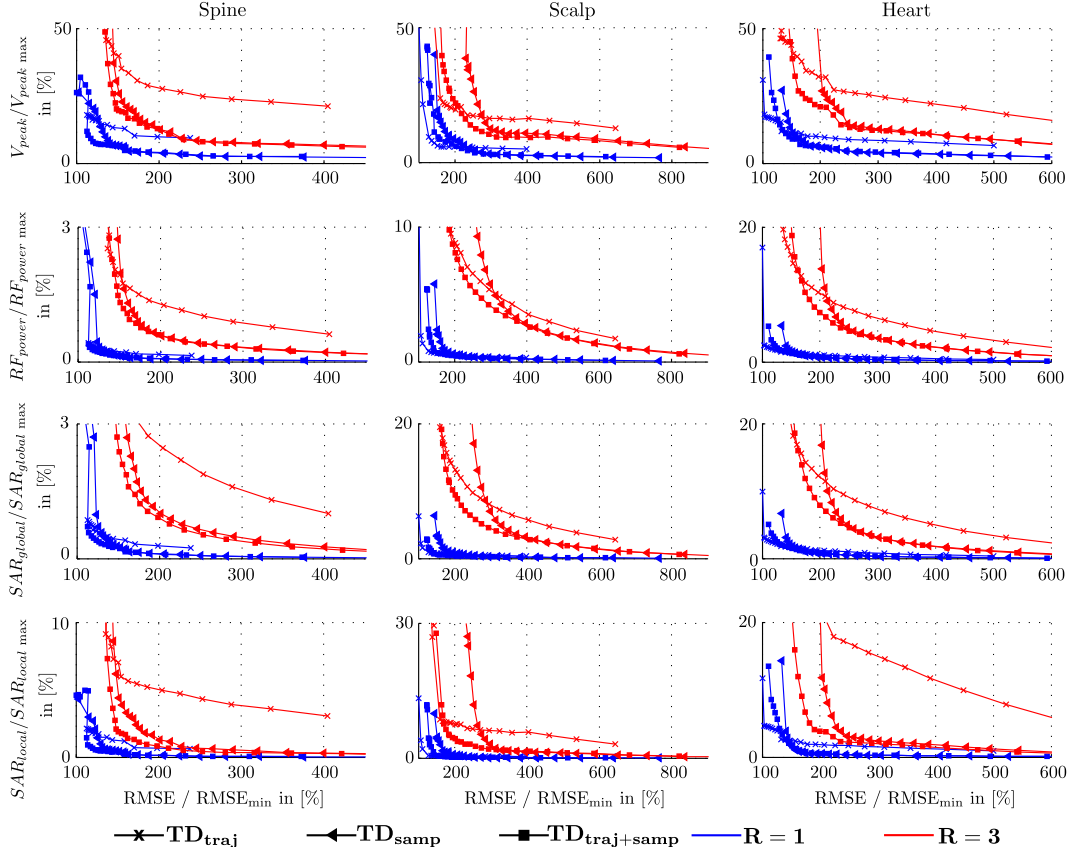


**Fig. 5.4:** Comparison of the proposed TD designs (cross, left-pointing triangle and square symbol) at different spatial fidelities and TX acceleration factors (blue and red color). The RF pulses were evaluated for different target patterns for spine, scalp and heart shown in the different columns. All assessed performance metrics were normalized to the respective highest ( $V_{peak}$ ,  $RF_{power}$ ,  $SAR_{global}$ ,  $SAR_{local}$ ) or smallest value ( $RMSE$ ) of all simulations per target pattern. Note that the L-curve plots were limited to the ROI and have different scaling.

proposed TD<sub>traj+samp</sub> trajectory offers more-or-less a mid-way solution, but with an overall balanced and smooth excitation response, while requiring significant less RF power and lower peak voltages. As stated above, similar reductions can be observed regarding the SAR performance, except for the scalp shaped pattern.

In Figure 5.7 the effect of a sub-optimal calibration of  $\beta$  and  $\gamma$  and thus, a sub-optimal choice of the weighting window width  $\alpha$  is shown. In both cases, an over- or under-estimation of  $\alpha$  relative to the optimal chosen value results in increased RF peak voltage, RF power and SAR values at same spatial accuracy. Furthermore, prominent differences in the spatial response are visible. The characteristics of the spatial response are either similar to the VD design (under-estimated  $\alpha$ ) or to the ED design (over-estimated  $\alpha$ ).

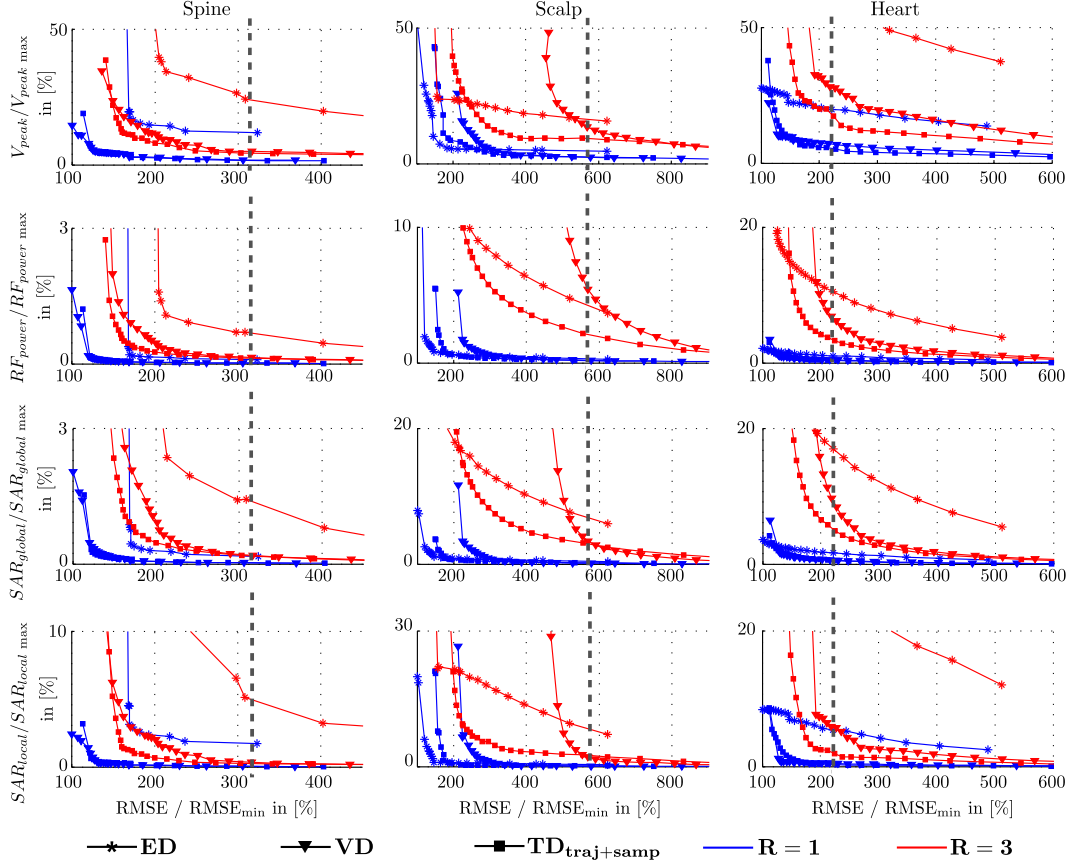


**Fig. 5.5:** Plot similar to *Figure 5.4*. Comparison of the proposed TD<sub>traj+samp</sub> design (squares) with other two state-of-the-art spiral designs, i.e. ED (asterisks) and VD (downward-pointing triangles). Detailed simulation results for an equal RMSE (grey dashed lines) were depicted in *Figure 5.6*.

### 2-Channel TX Experiments

The results of the human in-vivo experiments are shown in *Figure 5.8*. Note that the image window was adjusted to highlight the saturation performance, which is associated with an increased emphasis of the present noise. Imaging artifacts along the phase encoding direction can be seen in the heart (*Figure 5.8b*) and spine experiments (*Figure 5.8c*) due to flow/pulsation and moving of the inner organs. Generally, Bloch simulations of the different 2-D RF spiral saturation pulses align very well with the experimental results except for fat-signal containing areas (see e.g. scalp fat in *Figure 5.8a* or residual anterior wall fat signal in *Figure 5.8c*). The signal of all areas is successfully suppressed where the desired FA level of 90° has been achieved. The saturation performance of the RF pulses based on the different trajectory designs reflects the observations of the simulation study above: The ED RF pulses generally fail to fully saturate the signal within RF hardware limits due to insufficient magnetization level. However, the spatial response of the pulse is quite accurate, e.g. see ED experiment in *Figure 5.8a*. In contrast, the VD trajectory design ensures a proper

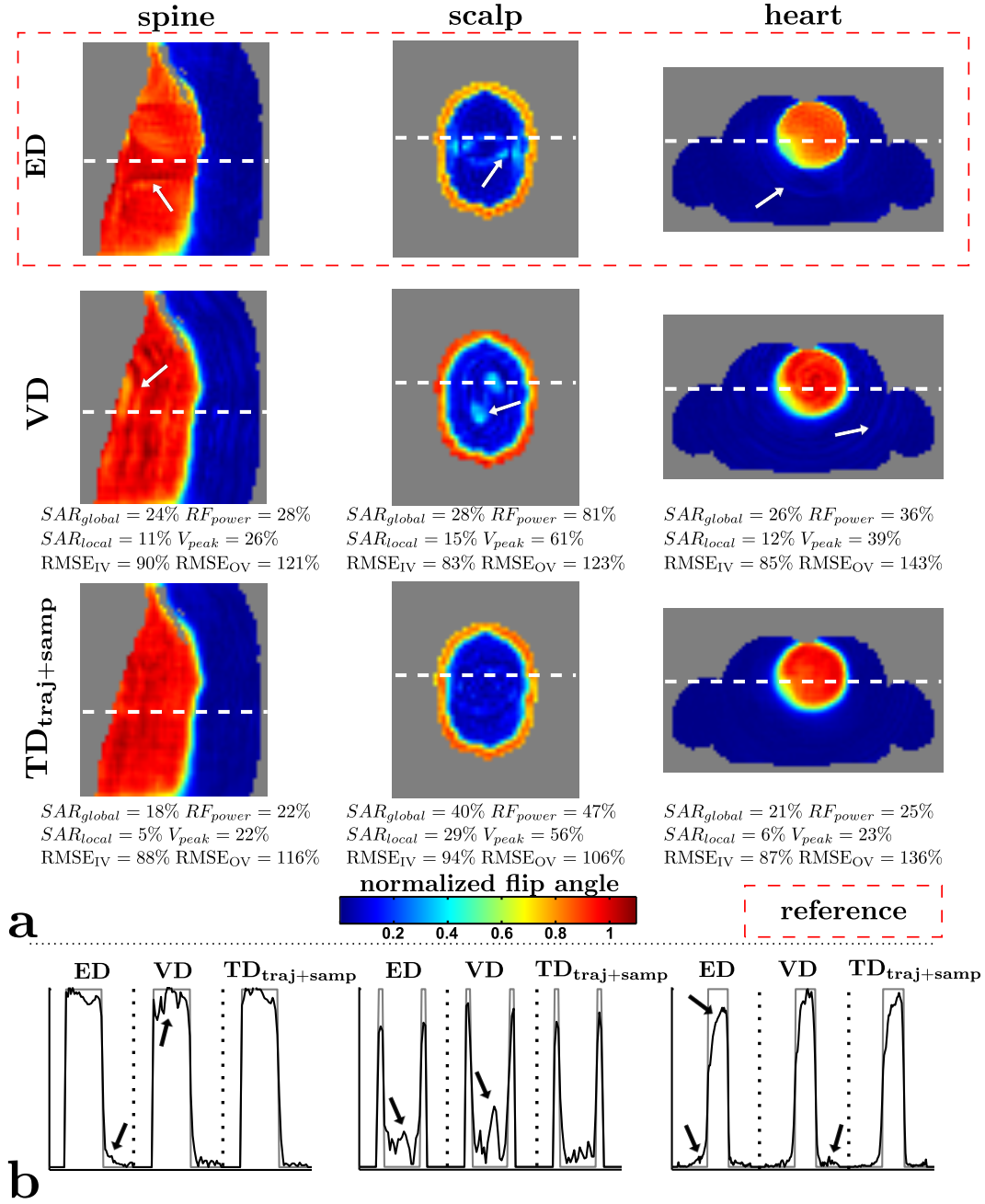


**Fig. 5.6:** Detailed simulation results of Figure 5.5 with  $R = 3$ . In each case, the designed RF pulses were matched to an identical overall numerical spatial fidelity RMSE. **a** Numerical Bloch simulations. All performance metrics were stated relative to ED trajectory based results (framed with red dashed lines). RMSE values were further separately analyzed for the inner- ( $RMSE_{IV}$ ) and outer-volume ( $RMSE_{OV}$ ). Prominent aliasing artifacts of the ED and VD design are indicated by white arrows. **b** 1-D profiles of the Bloch simulations (white dashed lines in **a**). Next to increased RF hardware efficiency, the beneficial effect of the  $TD_{traj+samp}$  design is also visible in an improved spatial response, i.e. reduced prominent aliasing and a smoother excitation profile.

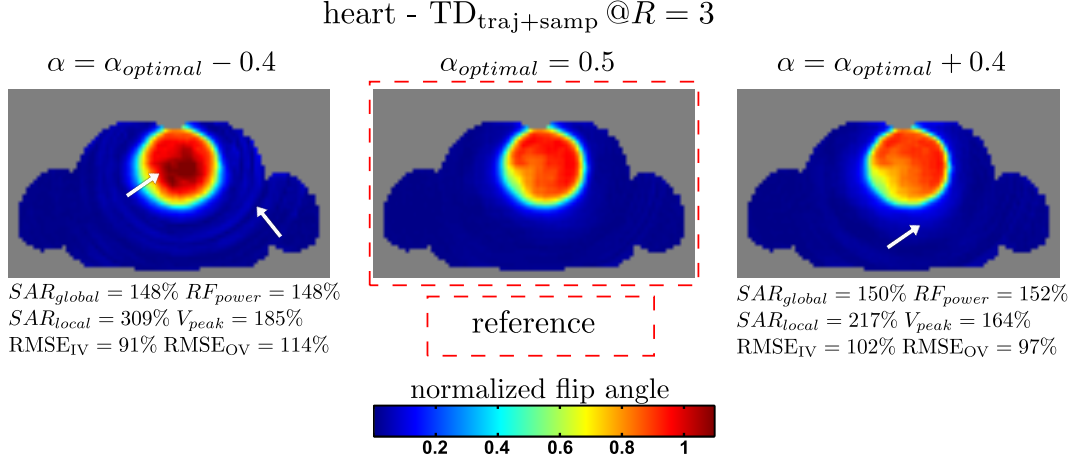


**Fig. 5.7:** Simulation results demonstrating a suboptimal calibration and thus suboptimal weighting window width  $\alpha$ . The simulations were matched to the same spatial accuracy with  $R = 3$ . All performance metrics were stated relative to TD trajectory design result with the optimal chosen  $\alpha$  value (framed with red dashed lines). A non-optimal choice of  $\alpha$  clearly results in decreased RF power efficiency and reduced goodness of the spatial response.

FA level except for the t-spine experiment, where residual signal can be found towards the frontal line of the spine (*Figure 5.8c*). Further, prominent spatial inaccuracies can be observed saturating the checkerboard pattern. Here, the VD approach fails to map the sharp edges of the pattern. Finally, the  $\text{TD}_{\text{traj+samp}}$  based RF pulses show again superior results: The proposed trajectory design offers both satisfactory spatial accuracy and average FA levels, which results in visibly improved saturation of the desired target patterns.

### 5.1.5 Discussion

In this work, spatially selective saturation RF pulses with parallel transmission were realized. Due to the required high flip angle level of the RF pulse, the design of spatially selective saturation pulses within RF hardware limits can be very challenging. Thus, a k-space trajectory method was proposed, which directly considers the target pattern information and  $B_1$  magnitude available to offer an inherent power-efficient RF pulse design. An analytically calculated metric was introduced to represent an optimized k-space sampling density function. The metric is principally based on the Fourier representation of the pattern, but is further adapted to locally match a spectral-spatial window function considering the pattern size and average  $B_1$  magnitude. The usage of the pure pattern Fourier representation has been reported independently as non-optimal for determining suitable k-space positions [60, 124]. Finally, the metric proposes a denser sampling ( $\text{TD}_{\text{samp}}$ ), a denser coverage ( $\text{TD}_{\text{traj}}$ ) or a combination of both ( $\text{TD}_{\text{traj+samp}}$ ) in k-space regions, where most of the target pattern information lies. In contrast to other methods, which time-dilate [85, 163] or optimize [4, 15, 53, 128] the critical RF pulse sections a-posteriori, the TD metric can be calculated directly without any additional computational optimizations or iterations. However, methods optimizing both the RF waveforms and k-space sampling positions [62, 63] can offer superior and a more complete solution by implicitly considering additional factors for optimal k-space sampling. On the



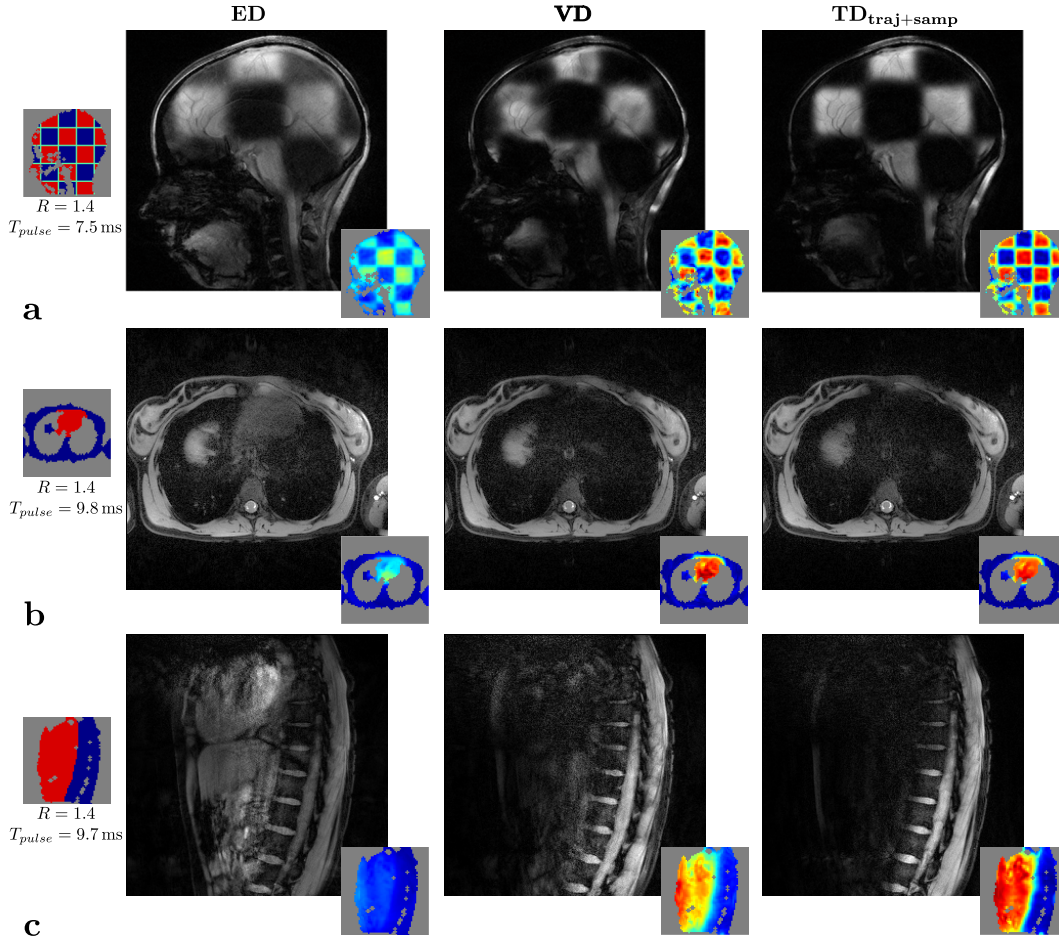


**Fig. 5.8:** Human in-vivo experiments. Shaped saturation RF pulses on the basis of the ED, VD and TD<sub>traj+samp</sub> trajectory designs were applied to different anatomical locations. **a** A checkerboard target pattern was saturated in a sagittal slice of the head. **b** The heart signal was suppressed in an abdominal transversal slice. **c** A sagittal spine-shaped target pattern was used to saturate the inner organs right next to the t-spine. Pictograms of the respective target patterns and the TX acceleration factor  $R$  with resulting saturation pulse length can be found at the very left of each scenario. Corresponding Bloch simulations of the 2-D RF spiral saturation pulse are attached at the right corner of each MR-image. Note that the contrast of the images was adjusted to highlight the differences.

other hand, these mostly iterative approaches require high calculation demands and are thus quite time inefficient with limited feasibility in clinical routine for such highly parameterized RF pulses as used in this study. The approach was further specified and discussed for 2-D spiral trajectories. The new trajectory design was evaluated with both an extensive simulation study and human in-vivo shaped-saturation experiments.

In the simulation study the three proposed TD designs were systematically analyzed for a 3 T 8-channel transmit whole body coil. 2-D RF spiral saturation pulses were calculated for three different anatomical positions and target patterns. All RF pulses were evaluated



with respect to their RF hardware and SAR efficiency at different TX acceleration levels and spatial fidelities. The simulations revealed that the distribution of the sampling points according to the proposed target-pattern-driven metric ( $TD_{\text{samp}}$ ) is sufficient to propose an RF-power-efficient pulse design. However, this design typically neglects the coverage of higher spatial frequencies (*Figure 5.3*), which results in a limited spatial fidelity (*Figure 5.4*). The adaption of both the spatial distribution of the spiral turns and k-space sampling points to the predefined target pattern ( $TD_{\text{traj+samp}}$ ) turned out to be the optimal combination without any spatial penalties. The  $TD_{\text{traj+samp}}$  k-space trajectory based RF pulses were further compared with two state-of-the-art spiral designs, i.e. a variable-slew-rate spiral design [70] with equally distributed spiral turns (ED) and a variable-density (VD) spiral design [71, 87, 165]. Generally, the ED design was observed to be associated with relatively high RF power, voltage and global / local SAR values. The VD spiral RF pulses provide means to significantly decrease these demands, but can also reduce the spatial accuracy (*Figure 5.5*). Similar observations have been already presented in [71]. The loss in spatial performance becomes more prominent, where the ratio of the spatial details versus the required RF power deposition at k-space center increases; see e.g. the relative right shift of the L-curve in the scalp pattern simulations in *Figure 5.5*. Here, the VD approach suffers from the low coverage of higher spatial frequencies, where structural details of the target pattern are encoded. In contrast to this fixed variable-density scheme, the  $TD_{\text{traj+samp}}$  offers a dynamic fit to the target pattern's implications to the energy and spatial details. As a consequence, the required RF power but also the spatial accuracy can be significantly improved compared to ED and VD RF pulses. This is also mostly accompanied with a considerable reduction of SAR. However, it was observed that the reduction of the RF power is not necessarily proportional to the SAR behavior: In the case of the scalp pattern simulations (*Figure 5.6*) the  $TD_{\text{traj+samp}}$  pulse showed an RF power decrease of another 34% compared to the VD pulse, but a relative global (local) SAR increase of 12% (14%). The non-trivial relationship between SAR and RF power in pTx has been frequently reported and requires explicit SAR constraints during RF pulse optimization. Further note that there might be some deviations in the local-SAR computation, when evaluated on the basis of 10 g regions instead of 10 cc regions. However, we always compared the relative improvement versus the overall maximum local SAR value of all simulation cases. Hence, this effect could be neglected.

The beneficial effects of the TD design were further confirmed in shaped saturation human in-vivo experiments on a 2-channel whole body transmit 3 T scanner. The advantages of the custom TD trajectory design are clearly visible in the different experiments under the restriction of the system RF hardware limits. Like in the simulation study, the target patterns were intentionally chosen to differ in their characteristics. The checkerboard pattern is rich in spatial details and structures and consequently requires sufficient encoding of higher spatial frequencies in k-space. In contrast to that the spine-shaped target is rather large and uniform and is expected to need high RF energy in the k-space center. In all cases, the  $TD_{\text{traj+samp}}$  approach clearly outperforms the other designs with static sampling strategies in the saturation performance, but also in the spatial accuracy. Again, the  $TD_{\text{traj+samp}}$  RF pulses benefit from the tailored placement of the sampling density and spiral turns. Still, some residual signals were observed: In the checkerboard experiment (*Figure 5.8a*) all designed pulses failed to saturate fat signals. In this study, the fat signal response was left uncontrolled by using solely a single-band RF optimization strategy. Therefore, the optimized RF pulses are expected not to cover the fat containing areas at all due to their known narrow bandwidth characteristic [15, 62]. To design proper fat-selective or other frequency selective shaped saturation pulses, e.g. for saturating the simulated rim-shaped fat ring,

the frequency response must be also taken into account in the RF design process. For this purpose, dual- or multi-band optimization strategies [7, 16, 62] have been established and would be suitable for this application. If the fat signal is not of interest the single-band designed pulses can be combined with common fat saturation pulses as an alternative to control the fat response. This combination includes a spatially tailored local saturation of water signals, but a global saturation of fat signals as applied in the heart (*Figure 5.8b*) and spine (*Figure 5.8c*) experiments. However, in the latter case still some residual fat signals remain due to strong off-resonance. Other residual signals in the body related experiments are likely due to inaccurate  $B_1$  and  $B_0$  maps being compromised from physiological movements during their acquisition.

It has to be noted that solely a small tip angle approximation based RF pulse optimization procedure [15] was used to design the large flip angle saturation pulses. Indeed, only subtle differences between the small tip angle approximation and Bloch simulations were observed. High RF voltages mainly cause artifacts due to non-linear evolutions of the magnetization. Those high RF values are likely to be sufficiently damped by the required Tikhonov regularization. The good performance of the small tip angle approximation in simulation as well as experiments for saturation flip angles of 90 degrees within the parallel transmit regime are in line with the early observations of Ref. [42].

The general robustness of the proposed TD approach relies on the detection of the local energy elevations in k-space. Especially if local energy hotspots at lower spatial frequencies are partially or fully omitted, the resulting k-space trajectory can be obstructive for an RF-power- and SAR-efficient design. Nevertheless, the local energy maxima can be analytically determined for standardized patterns, such as circles and squares. Furthermore, there are many well-established methods to identify local elevations of arbitrarily shaped patterns. In case of target patterns, which do not offer any local minimal / maximal in k-space, e.g., a 2D Gaussian shaped pattern, the TX k-space sampling density should be limited to the chosen weighting window. Here the excitation performance is expected similar to the VD approach, except that in addition the average  $B_1$  magnitude within the ROI and spatial size of the target pattern are considered. This adaption can still help to optimize the k-space sampling near the k-space center. A potential drawback might be the robustness of the empirically calibrated parameters for calculating the width of the weighting window (*Equation 5.4*). The linear approximation of the complex interaction of the chosen target pattern and the prevailing  $B_1$  fields might be insufficient. Other reports have already stated a non-deterministic and complex interaction between the target pattern and SAR related quantities [67, 68]. However, the proposed functional relation primarily attempts to capture target pattern associated fluctuations with respect to the required RF power deposition. No problems with the suggested parameter set were experienced, which were calibrated once with described calibration procedure. This observation is supported by the fact that the same values were used in the simulations and experiments. However, they were based on completely different system configurations and subjects. Nevertheless, a non-linear functional relationship incorporating further quantities or a more elaborate calibration procedure can be more accurate and reliable. Further research and validation is required, due to its' central impact. A sub-optimal calibration of the functional parameters results in reduced RF power efficiency and goodness of the spatial response (*Figure 5.7*) due to the inappropriate weighting of the local energy elevations. Particularly, the wrong choice of the weighting window width involves an insufficient sampling focus of either the k-space center or the outer k-space regions. Clearly, other weighting window types, e.g. Gaussian or Hamming, can also be used for weighting the local energy hotspots of the target pattern. A potential shortcoming regarding

the  $\text{TD}_{\text{traj+samp}}$  design in particular can be the elongation of the gradient waveforms due to the dynamic slew-rate slow-down, which affects the time efficiency of the trajectory design. Yet, from our experience the design of RF pulses with higher flip angle levels on the basis of time optimal gradient waveforms can be hardly realized within RF hardware limits. To stay within those limits, the dilatation of the gradient waveforms is necessary. Similar experiences were presented in [163]. It is likely that in presence of strong off-resonance a further gain in RF power efficiency can be realized, when also the  $B_0$  map information is included in the variable-density metric as previously described in [25]. A combination of the TD metric with more sophisticated RF pulses, such as 3-D selective stack of spirals, has been shown to be even more advantageous [30].

In conclusion, a new k-space trajectory design was proposed for efficiently designing spatially selective saturation pulses with pTx. The design takes advantage from the a-priori knowledge of the pre-defined target pattern and available  $B_1$  magnitude. The new design was specified for 2-D RF spiral pulses and evaluated in a simulation study. Based on these spatially selective RF pulses, anatomically shaped saturation human in-vivo experiments were realized for the first time to further investigate their performance. The proposed method was shown to offer superior RF hardware efficiency and spatial fidelity compared to two other state-of-the-art spiral trajectory designs. Thus, the TD design enables a more efficient RF pulse design or further TX acceleration. In most cases, a decrease of the corresponding global and local SAR values was observed, but is not generally guaranteed due to the complex nature of SAR. Therefore, a combination of TD-trajectory-based RF pulses with SAR constraint optimization is of high interest.

## 5.2 Shaped Fat-Saturation with Multi-Frequency Design

This section contains methods & principles that were accepted for publication in:

R. Schneider, J. Haueisen, and J. Pfeuffer. Shaped fat saturation with 2d spatially selective multi-frequency rf pulse design in parallel transmission. In *Proceedings of the 22nd Annual Meeting of the ISMRM, Milan, Italy*, page 1650, 2014.

### 5.2.1 Introduction

To avoid interference of unwanted signals with the region of interest, a localized suppression is often necessary. Typical examples in spectroscopy are the fat signal suppression in the vicinity of the prostate [161] or the suppression of the scalp cap [162]. To date the localized signal suppression is realized by the manual arrangement of multiple saturation slabs, which can be time consuming and anatomically inaccurate. The application of multi-frequency 2-D spatially selective RF pulse (MF-2DRF) would overcome this issue enabling the saturation of arbitrarily shaped patterns. However, due to their long pulse durations, sensitivity to off-resonance effects and other practical limitations, they have not been realized, yet.

In this work, multi-frequency shaped saturation pulses with pTx on a commercially available 3 T scanner are introduced. The MF-2DRF pulses based on a variable-density 2-D spiral trajectory were evaluated in phantom and human in-vivo experiments, saturating the fat signal in the scalp cap. The performance of the MF-2DRF pulses was further compared to a non-selective Gaussian fat saturation pulse.

### 5.2.2 Methods

To overcome the practical limitations of MF-2DRF saturation pulses, the combination of several approaches is necessary: First, with the usage of multiple transmit channels (pTx) MF-2DRF pulses can be undersampled/accelerated without aliasing artifacts. Furthermore, by incorporating the prevailing  $B_1$  and  $B_0$  maps into the pulse design, pTx allows for mitigation of off-resonance effects and flip angle non-uniformity. Second, the design of MF-2DRF pulses with higher flip-angle levels as required for saturation still remained challenging within given RF hardware and SAR limits. To tackle this problem, a variable density trajectory design, which inherently offers an RF-power-efficient pulse design [30–32] was proposed. The approach takes advantage of the a-priori knowledge of the desired target pattern and available  $B_1$  magnitude to adjust the sampling density in k-space and has been shown to be superior to common variable or equal-density sampling strategies [30–32]. Finally, to control the frequency response of MF-2DRF pulses, the RF pulse optimization was extended by the frequency dimension [7]:

$$\begin{bmatrix} \mathbf{m}_{Freq\ 1} \\ \mathbf{m}_{Freq\ 2} \\ \vdots \\ \mathbf{m}_{Freq\ N_f} \end{bmatrix} = \begin{bmatrix} \mathbf{A}_{Freq\ 1} \\ \mathbf{A}_{Freq\ 2} \\ \vdots \\ \mathbf{A}_{Freq\ N_f} \end{bmatrix} \mathbf{b}_{full}, \quad (5.12)$$

where  $\mathbf{m}_{Freq\ n}$  and  $\mathbf{A}_{Freq\ n}$  are the individual target magnetization pattern and system matrix, respectively,  $\mathbf{b}_{full}$  the vector containing the discretized RF waveforms to be optimized and  $N_f$  the number of design frequencies. In this particular case, the MF-2DRF pulse has to be designed to saturate the fat signal only and not the water signal.

To evaluate the performance of the proposed MF-2DRF fat saturation pulse optimization, phantom and human in-vivo experiments were pursued. In the phantom study, a fat-water phantom setup (FOV  $240 \times 240 \text{ mm}^2$ ) was used to analyze the frequency response of the localized suppression. MF-2DRF pulses were designed to saturate a rectangular shaped pattern for *a)* solely the fat signal and *b)* both fat-and-water containing areas. In the human experiments (FOV  $220 \times 220 \text{ mm}^2$ ), a rim-shaped pattern was chosen to saturate the fat signal in the scalp cap as often required in spectroscopy. In both scenarios, the fat saturation performance was further compared with a Gaussian FATSAT pulse, which globally saturates the fat signal over the whole FOV. Images were acquired on a 3 T MAGNETOM Skyra (Siemens, Erlangen, Germany) equipped with two transmit channels, using a prototype GRE sequence with matrix  $256 \times 256$  and TR/TE 50/10 ms. MF-2DRF pulses were optimized according to the multi-frequency small-tip-angle optimization approach proposed in [7], using the target-driven variable-density 2-D spiral trajectory of [31, 32]. In all experiments, the frequency response was defined only for two discrete design frequencies ( $N_f = 2$ ), i.e. for  $Freq\ 1 = 0 \text{ Hz}$  (water) and  $Freq\ 1 = -420 \text{ Hz}$  (fat). MF-2DRF pulse durations were 10 ms. No additional high-flip optimization strategy was applied. RF pulses were further regulated to stay within RF hardware and SAR constraints.

### 5.2.3 Results

Phantom and human results are shown in *Figure 5.9* and *Figure 5.10*. The phantom study (*Figure 5.9*) reveals that the MF-2DRF pulses can achieve similar fat saturation performance

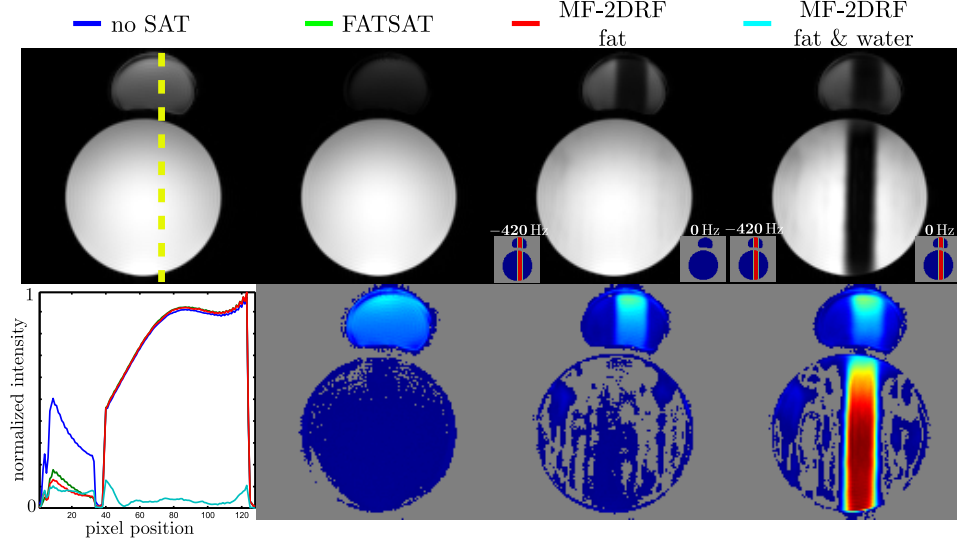


**Fig. 5.9:** Top row shows MR images with different fat saturation techniques: no saturation, non-selective Gaussian FATSAT, 2-D spatially selective MF-2DRF pulse saturating either just fat or both, fat and water signals. Bottom row shows respective 1-D profiles (dashed yellow line from top to bottom) and the difference to the non-saturated image. Defined target patterns for the individual design frequencies of the MF-2DRF pulses are attached at the lower corners of the corresponding MR images.

as the commonly used FATSAT and does not show any visible artifacts in the water band. In addition to the localized saturation, the proposed MF-2DRF pulse also includes the saturation of multiple frequency bands at once with satisfying performance (*Figure 5.9*, top right). The results were further confirmed in human in-vivo experiments (*Figure 5.10*). The fat signal was completely saturated in the neck by both the FATSAT and MF-2DRF fat saturation pulse. However, in the MF-2DRF experiment residual fat signal could be observed towards the forehead. On the other hand, the difference images reveal that the MF-2DRF pulses generally affect the water band signal less than the FATSAT.

#### 5.2.4 Discussion

The proposed MF-2DRF pulse design enables the saturation of multiple frequency bands at the same time. The proposed approach was successfully evaluated with the shaped saturation of the fat signal in phantom and human in-vivo experiments. The designed pulses offer comparable saturation performance as the commonly used global FATSAT pulse and showed less interference with the water band. The performance generally relies on the sufficient coverage of the  $B_1$  and  $B_0$  data, which can be challenging in low SNR areas as indicated by the residual fat-signals in the forehead. The extrapolation of the  $B_1$  and  $B_0$  data can help to overcome this problem. Further improvement and more accurate results can be expected, when more design frequencies are defined within the RF optimization process, but at cost of increased computational demands.

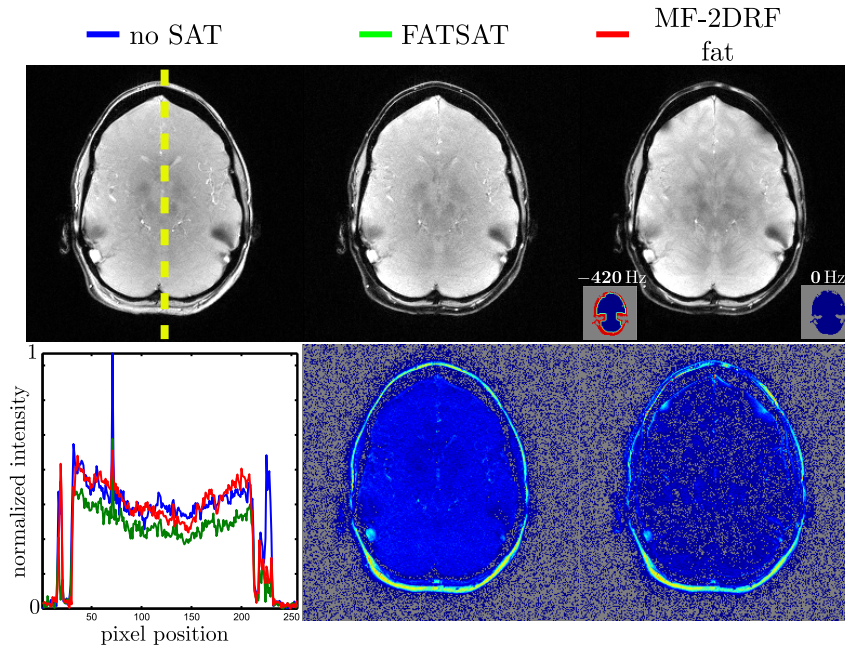


**Fig. 5.10:** Same as *Figure 5.9*, but without MF-2DRF saturating water and fat signal simultaneously. The MF-2DRF was designed to saturate the subcutaneous fat of the head in a rim-shaped pattern.

## Summary and Outlook

In MRI the continuous increase of the main magnetic field strength is pursued to facilitate ever higher resolved images of the human body. However, the higher field strengths are also accompanied with an increased potential for severe image artifacts caused by the inhomogeneity of the  $B_0$  static field and the spatial variation of the  $B_1$  transmit field. The parallel transmission (pTx) technology showed to be promising to counteract these problems. The multiple (localized) independent RF transmit coils provide increased flexibility in shaping the RF excitation field and can be thus utilized to mitigate the field inhomogeneities more efficiently.

The majority of current pTx-related work is still based on a custom hardware basis in the area of ultra-high-field systems. Although different vendors have introduced commercially available 3 T scanner systems equipped with two channel RF transmit body arrays, only little work has been transferred into clinical practice.

This work was motivated by the demand to integrate the pTx technology further into clinical applications on the basis of a commercially available clinical pTx scanner. The application focus of the work is the design of tailored RF pulses to dampen off-resonance related artifacts or undesired signal sources. The general RF pulse design framework was developed under the aim of considering all practical hardware and SAR constraints, so that the proposed methods were always evaluated in human in-vivo experiments for various flip angle levels. To improve the pTx workflow for clinical routine, care has been taken to limit the computational complexity of the introduced approaches. The following original contributions were made in this thesis.

- **Advanced off-resonance correction in slice-selective EP-2DRF pulses:** Spokes based EP-2DRF pulses are commonly used to realize reduced FOV imaging, which greatly reduce the impact of off-resonance effects in EPI acquisition schemes. The EP-2DRF pulse duration and excitation fidelity could be remarkably reduced by the integration into the pTx framework and by the introduction of a variable-density sampling scheme of the underlying TX k-space trajectory. In particular, the new trajectory design is directly calculated from a  $B_0$  map driven metric and was shown to offer up to 43% improved correction for off-resonance related distortions during excitation. At the same time the required RF power demands could be reduced up to 50% compared to the conventional design. However, higher TX acceleration factors or higher flip angle levels were observed to be less stable in conjunction with the variable-density method due to strong undersampling of the k-space center.

- **Asymmetric TX k-space trajectory design:** A more robust and pTx independent way to enhance the image quality in rFOV imaging was introduced by the asymmetric design of the EP-2DRF pulses. Considerable reductions of pulse durations by 25% were achieved while maintaining the excitation quality. The shortening of the RF excitation time can be linked to TE savings in EPI resulting in SNR gains of up to 25% compared to the conventional EP-2DRF designs. In combination with the proposed EP-2DRF pTx framework, the beneficial effect adds up to 40% increase of SNR.
- **Signal recovery in GRE-based image acquisitions with automated tailored RF excitations:** The pTx capability was used to compensate for off-resonance induced signal loss in  $T_2^*$ -weighted GRE acquisition sequences. A fully automated simultaneous z-shim approach was proposed on the basis of the prevailing  $B_0$  and  $B_1$  spatial information. The method applies subject-, slice- and RF transmit coil-specific time-delayed excitations to impose a z-shim phase to reduce those signal dropouts. The computationally fast and robust RF pulse design was proven to recover 47% of brain areas affected by signal loss in standard excitation images across 3 subjects. In these areas BOLD activation coverage could be also increased by approximately 57%.
- **Introduction of arbitrary 2-D shaped pTx RF saturation in-vivo:** Anatomically shaped saturation was realized for the first time in-vivo on the basis of pTx 2DRF spiral pulses. The practical design of such high-flip angle pulses is mainly hampered by the given RF hardware and SAR constraints. For this purpose, a novel spiral sampling scheme with inherent RF power efficiency was introduced, which is directly determined from the a-priori knowledge of the target pattern and  $B_1$  maps. The new design was shown to offer an optimized balance between its spatial response and RF power expense. Shaped saturation pulses were successfully applied to the human brain, heart and thoracic-spine with satisfying performance. The approach was further extended to enable frequency-specific 2DRF saturations. Exemplary designed shaped fat-saturation pulses were shown to offer comparable saturation performance as conventional non-selective fat saturation pulses.

The work done in this thesis demonstrated novel excitation techniques for three different application fields. The proposed techniques add clinical value in diagnosis and workflow, but have to be explored in more detail in elaborate studies. Clearly, the benefit of improved EP-2DRF excitations can be directly assessed by the gain in SNR and reduced image distortions in EPI [26, 27]. The robustness and reliability of EP-2DRF based rFOV imaging methods have to be further investigated in body imaging, where susceptibility effects, fat and other off-resonance effects are more challenging issues. Regarding the presented pTx z-shim approach, the benefit of the local signal recovery can be further evaluated in the scope of a specific clinical question, e.g. the detection of tumors and hemorrhage in the frontal orbital cortex. The approach can be also a valuable tool for resting state fMRI studies, where the sensitivity in several cortical structures can be increased. The shaped saturation pulses can be very useful for suppressing motion artifacts with anatomical accuracy. However, further work has to be done to integrate this approach efficiently into the clinical workflow. Ideally no further user interaction is required, e.g. in case of spine imaging, a spine-shaped saturation pattern is automatically determined from preceding acquisitions and needs no manual adjustment. The underlying RF power efficient trajectory design, which was developed for this purpose, can be also used for standard excitation pulses with lower flip angle, but with higher TX acceleration factors. The short 2DRF pulses can be used straight-forwardly for other applications, such as rFOV 3-D cardiac imaging.



Besides further clinical evaluation of the methods, their transfer to more advanced technical pTx setups has to be explored. RF transmit arrays with more TX channels, but also more sophisticated coil geometries have been shown beneficial for improved  $B_1$  shimming, spatially-selective excitation, RF power and SAR performance [168, 169]. Thus, 2DRF pulses can be designed more efficiently and further gains in rFOV imaging quality or shaped saturation performance can be expected. Similarly, the increased spatial degrees of freedom offer the potential for more distinct and tailored pTx z-shimming performance, which is likely to provide advanced in-plane signal recovery performance. However, a higher number of TX channels comes also with higher hardware costs and more complex RF interactions that ask for sophisticated safety monitoring functions and additional expenses. Before more advanced pTx technology can enter the clinical routine, further assessment of the general advantages of pTx is still required in this field. This work contributed several methods, which significantly support pTx to become an approved technology within clinically established applications.



---

## References

- [1] O. Kraff, A. Fischer, A. M. Nagel, C. Mönninghoff, and M. E. Ladd. Mri at 7 tesla and above: Demonstrated and potential capabilities. *J Magn Reson Imaging*, 2014.
- [2] U. Katscher, P. Boernert, C. Leussler, and J. S. van den Brink. Transmit sense. *Magn Reson Med*, 49(1):144–150, 2003. ISSN 1522-2594. URL <http://dx.doi.org/10.1002/mrm.10353>.
- [3] Y. Zhu. Parallel excitation with an array of transmit coils. *Magn Reson Med*, 51(4):775–784, 2004. ISSN 1522-2594. URL <http://dx.doi.org/10.1002/mrm.20011>.
- [4] W. Grissom, C.-y. Yip, Z. Zhang, V. A. Stenger, J. A. Fessler, and D. C. Noll. Spatial domain method for the design of rf pulses in multicoil parallel excitation. *Magn Reson Med*, 56(3):620–629, 2006. ISSN 1522-2594. URL <http://dx.doi.org/10.1002/mrm.20978>.
- [5] I. Graesslin, K. Falaggis, S. Biederer, D. Glaesel, P. Vernickel, P. Roeschmann, C. Leussler, A. Thran, Z. Zhai, M. Morich, et al. Sar simulations and experiments for parallel transmission. In *Proceedings of the Joint Annual Meeting of ISMRM-ESMRMB, Berlin, Germany*, page 1090, 2007.
- [6] A. Zelinski, L. Wald, K. Setsompop, V. Alagappan, B. Gagoski, V. Goyal, and E. Adalsteinsson. Fast slice-selective radio-frequency excitation pulses for mitigating b+ 1 inhomogeneity in the human brain at 7 tesla. *Magn Reson Med*, 59(6):1355–1364, 2008.
- [7] K. Setsompop, V. Alagappan, B. Gagoski, A. Potthast, F. Hebrank, U. Fontius, F. Schmitt, L. Wald, and E. Adalsteinsson. Broadband slab selection with b 1+ mitigation at 7t via parallel spectral-spatial excitation. *Magn Reson Med*, 61(2):493–500, 2009.
- [8] W. Deng, C. Yang, V. Alagappan, L. L. Wald, F. E. Boada, and V. A. Stenger. Simultaneous z-shim method for reducing susceptibility artifacts with multiple transmitters. *Magn Reson Med*, 61(2):255–259, 2009. ISSN 1522-2594. doi: 10.1002/mrm.21870. URL <http://dx.doi.org/10.1002/mrm.21870>.
- [9] D. Brunner and K. Pruessmann. Optimal design of multiple-channel rf pulses under strict power and sar constraints. *Magn Reson Med*, 63(5):1280–1291, 2010.
- [10] M. Nelles, R. S. Koenig, J. Gieseke, M. M. Guerand-van Battum, G. M. Kukuk, H. H. Schild, and W. A. Willinek. Dual-source parallel rf transmission for clinical

- mr imaging of the spine at 3.0 t: Intraindividual comparison with conventional single-source transmission. *Radiology*, 257(3):743–753, December 1, 2010 2010. URL <http://radiology.rsna.org/content/257/3/743.abstract>.
- [11] J. Bouvier, I. Troprès, L. Lamalle, S. Grand, S. Breil, J. Le Bas, and A. Krainik. Evaluation of dual-source parallel rf excitation technology in mri of thoraco-lumbar spine at 3.0 t. *J Neuroradiol*, 2012.
  - [12] M. Cloos, N. Boulant, M. Luong, G. Ferrand, E. Giacomini, D. Le Bihan, and A. Amadon. kt-points: Short three-dimensional tailored rf pulses for flip-angle homogenization over an extended volume. *Magn Reson Med*, 67:72–80, 2012.
  - [13] B. Guerin, M. Gebhardt, S. Cauley, E. Adalsteinsson, and L. L. Wald. Local specific absorption rate (sar), global sar, transmitter power, and excitation accuracy trade-offs in low flip-angle parallel transmit pulse design. *Magn Reson Med*, pages n/a–n/a, 2013. ISSN 1522-2594. doi: 10.1002/mrm.24800. URL <http://dx.doi.org/10.1002/mrm.24800>.
  - [14] H. Zheng, T. Zhao, Y. Qian, C. Schirda, T. S. Ibrahim, and F. E. Boada. Multi-slice parallel transmission three-dimensional tailored rf (ptx 3dtrf) pulse design for signal recovery in ultra high field functional mri. *J Magn Reson*, 228(0):37 – 44, 2013. ISSN 1090-7807. doi: 10.1016/j.jmr.2012.12.021. URL <http://www.sciencedirect.com/science/article/pii/S1090780713000062>.
  - [15] K. Setsompop, L. L. Wald, V. Alagappan, B. A. Gagoski, and E. Adalsteinsson. Magnitude least squares optimization for parallel radio frequency excitation design demonstrated at 7 tesla with eight channels. *Magn Reson Med*, 59(4):908–915, 2008. ISSN 1522-2594. URL <http://dx.doi.org/10.1002/mrm.21513>.
  - [16] S. Malik, S. Keihaninejad, A. Hammers, and J. Hajnal. Tailored excitation in 3d with spiral nonselective (spins) rf pulses. *Magn Reson Med*, 67:1303–1315, 2012. doi: 10.1002/mrm.23118.
  - [17] J. T. Schneider, R. Kalayciyan, M. Haas, S. R. Herrmann, W. Ruhm, J. Hennig, and P. Ullmann. Inner-volume imaging in vivo using three-dimensional parallel spatially selective excitation. *Magn Reson Med*, pages n/a–n/a, 2012. ISSN 1522-2594. doi: 10.1002/mrm.24381. URL <http://dx.doi.org/10.1002/mrm.24381>.
  - [18] B. A. Poser, R. J. Anderson, B. Guerin, K. Setsompop, W. Deng, A. Mareyam, P. Serano, L. L. Wald, and V. A. Stenger. Simultaneous multislice excitation by parallel transmission. *Magn Reson Med*, pages n/a–n/a, 2013. ISSN 1522-2594. doi: 10.1002/mrm.24791. URL <http://dx.doi.org/10.1002/mrm.24791>.
  - [19] Philips Healthcare. *Philips Achieva 3.0T TX. Make a leap in performance*. Koninklijke Philips Electronics N.V., P.O. Box 1286, 5602 EG Eindhoven, The Netherlands, May 2009.
  - [20] Siemens Healthcare. *Siemens MAGNETOM Skyra. Maximize 3T. Every case. Every day*. Siemens AG, Wittelsbacherplatz 2, DE-80333 Muenchen, Germany, December 2013.
  - [21] Siemens Healthcare. *Siemens MAGNETOM Prisma. The 3T PowerPack for exploration*. Siemens AG, Wittelsbacherplatz 2, DE-80333 Muenchen, Germany, December 2013.

- [22] OECD. *Health at a Glance 2013 OECD Indicators: OECD Indicators*. OECD Publishing, 2013. ISBN 9789264205024. URL [http://dx.doi.org/10.1787/health\\_glance-2013-en](http://dx.doi.org/10.1787/health_glance-2013-en).
- [23] R. Schneider, D. Ritter, J. Haueisen, and J. Pfeuffer. Novel 2drf optimization framework for spatially selective rf pulses incorporating b1, b0 and variable-density trajectory design. In *Proceedings of the 20th Annual Meeting of the ISMRM, Melbourne, Australia*, page 3454, 2012.
- [24] R. Schneider, D. Ritter, J. Haueisen, and J. Pfeuffer. Evaluation of 2drf echo-planar pulse designs for parallel transmission. In *Proceedings of the 20th Annual Meeting of the ISMRM, Melbourne, Australia*, page 3459, 2012.
- [25] R. Schneider, D. Ritter, J. Haueisen, and J. Pfeuffer. B0-informed variable density trajectory design for enhanced correction of off-resonance effects in parallel transmission. *Magn Reson Med*, 71:1381–1393, 2014. ISSN 1522-2594. doi: 10.1002/mrm.24780. URL <http://dx.doi.org/10.1002/mrm.24780>.
- [26] R. Schneider, J. Haueisen, and J. Pfeuffer. Asymmetric two-dimensional spatially selective excitation in echo-planar imaging. In *Proceedings of the 22nd Annual Meeting of the ISMRM, Milan, Italy*, page 4436, 2014.
- [27] J. Ream, C. Gliemli, M. Lazar, N. Campbell, J. Pfeuffer, R. Schneider, and A. Rosenkrantz. Zoomed epi using parallel transmission for tractography of the prostate gland with an endorectal coil:a feasibility study. In *Proceedings of the 22nd Annual Meeting of the ISMRM, Milan, Italy*, page 2179, 2014.
- [28] R. Schneider, C. Gliemli, C. Geppert, J. Haueisen, F. Boada, and J. Pfeuffer. Local signal recovery in clinical flash imaging with parallel transmission. In *Proceedings of the 22nd Annual Meeting of the ISMRM, Milan, Italy*, page 4777, 2014.
- [29] R. Schneider, F. Boada, J. Haueisen, and J. Pfeuffer. Automated slice-specific simultaneous z-shim method for reducing b1 inhomogeneity and susceptibility-induced signal loss with parallel transmission at 3t. *Magn Reson Med*, page in press, 2014. ISSN 1522-2594.
- [30] R. Schneider, M. Gebhardt, J. Haueisen, and J. Pfeuffer. Target-pattern-informed variable-density trajectory design for low-sar pulse design in parallel transmission. In *Proceedings of the 21st Annual Meeting of the ISMRM, Salt Lake City, USA*, page 4261, 2013.
- [31] R. Schneider, J. Haueisen, and J. Pfeuffer. Shaped saturation with inherent radiofrequency-power-efficient trajectory design in parallel transmission. *Magn Reson Med*, 72:1015–1027, 2014. ISSN 1522-2594. doi: 10.1002/mrm.25016. URL <http://dx.doi.org/10.1002/mrm.25016>.
- [32] R. Schneider, J. Haueisen, and J. Pfeuffer. Shaped saturation with rf power efficient 2d spatially selective spiral design in parallel transmission. In *Proceedings of the 22nd Annual Meeting of the ISMRM, Milan, Italy*, page 1463, 2014.
- [33] R. Schneider, J. Haueisen, and J. Pfeuffer. Shaped fat saturation with 2d spatially selective multi-frequency rf pulse design in parallel transmission. In *Proceedings of the 22nd Annual Meeting of the ISMRM, Milan, Italy*, page 1650, 2014.

- [34] E. Haacke. *Magnetic resonance imaging: physical principles and sequence design*. J. Wiley & Sons, 1999. ISBN 9780471351283. URL <http://books.google.de/books?id=Bn0vQgAACAAJ>.
- [35] M. Bernstein, K. King, and X. Zhou. *Handbook of MRI pulse sequences*. Elsevier Academic Press, 2004. ISBN 9780120928613. URL <http://books.google.de/books?id=d6PLHcyejEIC>.
- [36] M. Reiser, W. Semmler, and H. Hricak. *Magnetic Resonance Tomography*. Springer, 2007. ISBN 9783540293545. URL <http://books.google.de/books?id=C4Tuzckp3oQC>.
- [37] R. Graaf. *In vivo NMR spectroscopy: principles and techniques*. John Wiley & Sons, 2008. ISBN 9780470026700. URL <http://books.google.de/books?id=048W3-pd3TEC>.
- [38] M. H. Levitt. *Spin dynamics: basics of nuclear magnetic resonance*. John Wiley & Sons, 2008.
- [39] K. Ugurbil, G. Adriany, P. Andersen, W. Chen, M. Garwood, R. Gruetter, P.-G. Henry, S.-G. Kim, H. Lieu, I. Tkac, et al. Ultrahigh field magnetic resonance imaging and spectroscopy. *Magn Reson Imaging*, 21(10):1263–1281, 2003.
- [40] F. Bloch. Nuclear induction. *Phys Rev*, 70(7-8):460, 1946.
- [41] R. K. Wangsness and F. Bloch. The dynamical theory of nuclear induction. *Phys Rev*, 89(4):728, 1953.
- [42] J. Pauly, D. Nishimura, and A. Macovski. A k-space analysis of small-tip-angle excitation. *J Magn Reson*, 81(1):43–56, 1989. ISSN 0022-2364. URL <http://www.sciencedirect.com/science/article/pii/0022236489902655>.
- [43] C. J. Hardy, H. E. Cline, and P. A. Bottomley. Correcting for nonuniform k-space sampling in two-dimensional nmr selective excitation. *J Magn Reson*, 87(3):639–645, 1990.
- [44] P. Börnert and B. Aldefeld. On spatially selective rf excitation and its analogy with spiral mr image acquisition. *Magn Reson Mater Phy*, 7(3):166–178, 1998. ISSN 0968-5243. doi: 10.1007/BF02591334. URL <http://dx.doi.org/10.1007/BF02591334>.
- [45] M. T. Alley, J. M. Pauly, F. G. Sommer, and N. J. Pelc. Angiographic imaging with 2d rf pulses. *Magn Reson Med*, 37(2):260–267, 1997. ISSN 1522-2594. URL <http://dx.doi.org/10.1002/mrm.1910370220>.
- [46] S. Rieseberg, J. Frahm, and J. Finsterbusch. Two-dimensional spatially-selective rf excitation pulses in echo-planar imaging. *Magn Reson Med*, 47(6):1186–1193, 2002. ISSN 1522-2594. URL <http://dx.doi.org/10.1002/mrm.10157>.
- [47] C. Schröder, P. Börnert, and B. Aldefeld. Spatial excitation using variable-density spiral trajectories. *J Magn Reson Imaging*, 18(1):136–141, 2003.
- [48] C. Yip, J. Fessler, and D. Noll. Iterative rf pulse design for multidimensional, small tip angle selective excitation. *Magn Reson Med*, 54(4):908–917, 2005. ISSN 1522-2594.
- [49] J. M. Pauly, B. S. Hu, S. J. Wang, D. G. Nishimura, and A. Macovski. A three-dimensional spin-echo or inversion pulse. *Magn Reson Med*, 29(1):2–6, 1993. ISSN

- 1522-2594. doi: 10.1002/mrm.1910290103. URL <http://dx.doi.org/10.1002/mrm.1910290103>.
- [50] K. Pruessmann, M. Weiger, M. Scheidegger, and P. Boesiger. Sense: sensitivity encoding for fast mri. *Magn Reson Med*, 42(5):952–962, 1999. ISSN 0740-3194.
  - [51] K. Setsompop, L. L. Wald, V. Alagappan, B. Gagoski, F. Hebrank, U. Fontius, F. Schmitt, and E. Adalsteinsson. Parallel rf transmission with eight channels at 3 tesla. *Magn Reson Med*, 56(5):1163–1171, 2006. ISSN 1522-2594. doi: 10.1002/mrm.21042. URL <http://dx.doi.org/10.1002/mrm.21042>.
  - [52] M. Jankiewicz, H. Zeng, J. Moore, A. Anderson, M. Avison, E. Welch, and J. Gore. Practical considerations for the design of sparse-spokes pulses. *J Magn Reson*, 203(2):294–304, 2010.
  - [53] J. Lee, M. Gebhardt, L. Wald, and E. Adalsteinsson. Local sar in parallel transmission pulse design. *Magn Reson Med*, 67:1566–1578, 2012.
  - [54] X. Wu, C. Akgün, J. Vaughan, P. Andersen, J. Strupp, K. Ugurbil, and P. Moortele. Adapted rf pulse design for sar reduction in parallel excitation with experimental verification at 9.4 t. *J Magn Reson*, 205(1):161–170, 2010.
  - [55] A. C. Zelinski, L. L. Wald, K. Setsompop, V. Alagappan, B. A. Gagoski, V. K. Goyal, F. Hebrank, U. Fontius, F. Schmitt, and E. Adalsteinsson. Comparison of three algorithms for solving linearized systems of parallel excitation rf waveform design equations: Experiments on an eight-channel system at 3 tesla. *Concept Magn Reso B*, 31(3):176–190, 2007. ISSN 1552-504X.
  - [56] K. Miller. Least squares methods for ill-posed problems with a prescribed bound. *SIAM J Math Anal*, 1(1):52–74, 1970.
  - [57] C. L. Lawson and R. J. Hanson. *Solving least squares problems*, volume 161. SIAM, 1974.
  - [58] M. A. Cloos, M. Luong, G. Ferrand, A. Amadon, D. Le Bihan, and N. Boulant. Local sar reduction in parallel excitation based on channel-dependent tikhonov parameters. *J Magn Reson Imaging*, 32(5):1209–1216, 2010.
  - [59] C. Yip, J. Fessler, and D. Noll. Advanced three-dimensional tailored rf pulse for signal recovery in  $t_2^*$ -weighted functional magnetic resonance imaging. *Magn Reson Med*, 56(5):1050–1059, 2006.
  - [60] C. Ma, D. Xu, K. F. King, and Z.-P. Liang. Joint design of spoke trajectories and rf pulses for parallel excitation. *Magn Reson Med*, 65(4):973–985, 2011. ISSN 1522-2594. doi: 10.1002/mrm.22676. URL <http://dx.doi.org/10.1002/mrm.22676>.
  - [61] D. Yoon, J. A. Fessler, A. C. Gilbert, and D. C. Noll. Fast joint design method for parallel excitation radiofrequency pulse and gradient waveforms considering off-resonance. *Magn Reson Med*, 68(1):278–285, 2012. ISSN 1522-2594. doi: 10.1002/mrm.24311. URL <http://dx.doi.org/10.1002/mrm.24311>.
  - [62] W. A. Grissom, M.-M. Khalighi, L. I. Sacolick, B. K. Rutt, and M. W. Vogel. Small-tip-angle spokes pulse design using interleaved greedy and local optimization methods. *Magn Reson Med*, 68(5):1553–1562, 2012. ISSN 1522-2594. doi: 10.1002/mrm.24165. URL <http://dx.doi.org/10.1002/mrm.24165>.

- [63] C. Yip, W. Grissom, J. Fessler, and D. Noll. Joint design of trajectory and rf pulses for parallel excitation. *Magn Reson Med*, 58(3):598–604, 2007.
- [64] D. Chen, F. Bornemann, M. W. Vogel, L. I. Sacolick, G. Kudiella, and Y. Zhu. Sparse parallel transmit pulse design using orthogonal matching pursuit method. In *Proceedings of the 17th Annual Meeting of the ISMRM, Honolulu, USA*, page 171, 2009.
- [65] I. E. C. IEC. International standard, medical electrical equipment. part 2. particular requirements for the safety of magnetic resonance equipment for medical diagnosis, 3rd edition., March 2010.
- [66] D. Xu, K. F. King, Y. Zhu, G. C. McKinnon, and Z.-P. Liang. A noniterative method to design large-tip-angle multidimensional spatially-selective radio frequency pulses for parallel transmission. *Magn Reson Med*, 58(2):326–334, 2007. ISSN 1522-2594. URL <http://dx.doi.org/10.1002/mrm.21314>.
- [67] P. Ullmann, G. Wuebbeler, S. Junge, F. Seifert, W. Ruhm, and J. Hennig. Sar-analysis for transmit sense with a 4-channel head array at 3 t. In *Proceedings of the 14th Annual Meeting of the ISMRM, Seattle, WA, USA*, page 601, 2006.
- [68] A. C. Zelinski, L. M. Angelone, V. K. Goyal, G. Bonmassar, E. Adalsteinsson, and L. L. Wald. Specific absorption rate studies of the parallel transmission of inner-volume excitations at 7t. *J Magn Reson Imaging*, 28(4):1005–1018, 2008. ISSN 1522-2586. doi: 10.1002/jmri.21548. URL <http://dx.doi.org/10.1002/jmri.21548>.
- [69] I. Graesslin, S. Biederer, F. Schweser, K. Zimmermann, U. Katscher, and P. Börner. Sar reduction for parallel transmission using verse and k-space filtering. In *Proceedings 15th Scientific Meeting, International Society for Magnetic Resonance in Medicine, Berlin*, page 674, 2007.
- [70] D. Xu, K. King, and Z. Liang. Variable slew-rate spiral design: Theory and application to peak b1 amplitude reduction in 2d rf pulse design. *Magn Reson Med*, 58(4):835–842, 2007.
- [71] Y. Liu, K. Feng, M. McDougall, S. Wright, and J. Ji. Reducing sar in parallel excitation using variable-density spirals: a simulation-based study. *Magn Reson Imaging*, 26(8): 1122–1132, 2008.
- [72] G. Eichfelder and M. Gebhardt. Local specific absorption rate control for parallel transmission by virtual observation points. *Magn Reson Med*, 66(5):1468–1476, 2011. ISSN 1522-2594. doi: 10.1002/mrm.22927. URL <http://dx.doi.org/10.1002/mrm.22927>.
- [73] A. Sbrizzi, H. Hoogduin, J. J. Lagendijk, P. Luijten, G. L. G. Sleijpen, and C. A. T. van den Berg. Fast design of local n-gram-specific absorption rate-optimized radiofrequency pulses for parallel transmit systems. *Magn Reson Med*, 67(3):824–834, 2012. ISSN 1522-2594. doi: 10.1002/mrm.23049. URL <http://dx.doi.org/10.1002/mrm.23049>.
- [74] J. Pauly, D. Nishimura, and A. Macovski. A linear class of large-tip-angle selective excitation pulses. *J Magn Reson*, 82(3):571–587, 1989. ISSN 0022-2364. URL <http://www.sciencedirect.com/science/article/pii/0022236489902199>.



- [75] K. Setsompop, V. Alagappan, A. C. Zelinski, A. Potthast, U. Fontius, F. Hebrank, F. Schmitt, L. L. Wald, and E. Adalsteinsson. High-flip-angle slice-selective parallel rf transmission with 8 channels at 7t. *J Magn Reson*, 195(1):76–84, 2008.
- [76] W. A. Grissom, C.-Y. Yip, S. M. Wright, J. A. Fessler, and D. C. Noll. Additive angle method for fast large-tip-angle rf pulse design in parallel excitation. *Magn Reson Med*, 59(4):779–787, 2008.
- [77] H. Zheng, T. Zhao, Y. Qian, T. S. Ibrahim, and F. E. Boada. Improved large tip angle parallel transmission pulse design through a perturbation analysis of the bloch equation. *Magn Reson Med*, 66(3):687–696, 2011.
- [78] D. Xu, K. F. King, Y. Zhu, G. C. McKinnon, and Z.-P. Liang. Designing multichannel, multidimensional, arbitrary flip angle rf pulses using an optimal control approach. *Magn Reson Med*, 59(3):547–560, 2008.
- [79] W. A. Grissom, D. Xu, A. B. Kerr, J. A. Fessler, and D. C. Noll. Fast large-tip-angle multidimensional and parallel rf pulse design in mri. *IEEE T Med Imaging*, 28(10):1548–1559, 2009.
- [80] A. Massire, M. A. Cloos, A. Vignaud, D. L. Bihan, A. Amadon, and N. Boulant. Design of non-selective refocusing pulses with phase-free rotation axis by gradient ascent pulse engineering algorithm in parallel transmission at 7t. *J Magn Reson*, 230(0):76 – 83, 2013. ISSN 1090-7807. doi: 10.1016/j.jmr.2013.01.005. URL <http://www.sciencedirect.com/science/article/pii/S1090780713000190>.
- [81] C. Yip, D. Yoon, V. Olafsson, S. Lee, W. Grissom, J. Fessler, and D. Noll. Spectral-spatial pulse design for through-plane phase precompensatory slice selection in t<sub>2</sub>\*-weighted functional mri. *Magn Reson Med*, 61(5):1137–1147, 2009.
- [82] C. Yang, W. Deng, V. Alagappan, L. L. Wald, and V. A. Stenger. Four-dimensional spectral-spatial rf pulses for simultaneous correction of b1+ inhomogeneity and susceptibility artifacts in t<sub>2</sub>\*-weighted mri. *Magn Reson Med*, 64(1):1–8, 2010.
- [83] J. Finsterbusch. Fast-spin-echo imaging of inner fields-of-view with 2d-selective rf excitations. *J Magn Reson Imaging*, 31(6):1530–1537, 2010. ISSN 1522-2586. URL <http://dx.doi.org/10.1002/jmri.22196>.
- [84] U. Katscher and P. Boernert. Parallel rf transmission in mri. *NMR Biomed*, 19(3):393–400, 2006. ISSN 1099-1492. URL <http://dx.doi.org/10.1002/nbm.1049>.
- [85] D. Lee, M. Lustig, W. Grissom, and J. Pauly. Time-optimal design for multidimensional and parallel transmit variable-rate selective excitation. *Magn Reson Med*, 61(6):1471–1479, 2009.
- [86] S. Saekho, F. E. Boada, D. C. Noll, and V. A. Stenger. Small tip angle three-dimensional tailored radiofrequency slab-select pulse for reduced b1 inhomogeneity at 3 t. *Magn Reson Med*, 53(2):479–484, 2005.
- [87] D.-h. Kim, E. Adalsteinsson, and D. M. Spielman. Simple analytic variable density spiral design. *Magn Reson Med*, 50(1):214–219, 2003. ISSN 1522-2594. doi: 10.1002/mrm.10493. URL <http://dx.doi.org/10.1002/mrm.10493>.

- [88] J. G. Pipe and N. R. Zwart. Spiral trajectory design: A flexible numerical algorithm and base analytical equations. *Magn Reson Med*, pages n/a–n/a, 2013. ISSN 1522-2594. doi: 10.1002/mrm.24675. URL <http://dx.doi.org/10.1002/mrm.24675>.
- [89] D. C. Turley and J. G. Pipe. Distributed spirals: A new class of three-dimensional k-space trajectories. *Magn Reson Med*, pages n/a–n/a, 2012. ISSN 1522-2594. doi: 10.1002/mrm.24475. URL <http://dx.doi.org/10.1002/mrm.24475>.
- [90] S. Wong and M. Roos. A strategy for sampling on a sphere applied to 3d selective rf pulse design. *Magn Reson Med*, 32(6):778–784, 1994.
- [91] M. Lustig, S.-J. Kim, and J. Pauly. A fast method for designing time-optimal gradient waveforms for arbitrary -space trajectories. *IEEE T Med Imaging*, 27(6):866–873, 2008. ISSN 0278-0062. doi: 10.1109/TMI.2008.922699.
- [92] X. Wu, J. Vaughan, K. Ugurbil, and P. Van de Moortele. Parallel excitation in the human brain at 9.4 t counteracting k-space errors with rf pulse design. *Magn Reson Med*, 63(2):524–529, 2010.
- [93] J. Schneider, M. Haas, W. Ruhm, J. Hennig, and P. Ullmann. Robust spatially selective excitation using radiofrequency pulses adapted to the effective spatially encoding magnetic fields. *Magn Reson Med*, 65(2):409–421, 2011. ISSN 1522-2594.
- [94] M. Jenkinson. Fast, automated, n-dimensional phase-unwrapping algorithm. *Magn Reson Med*, 49(1):193–197, 2003.
- [95] R. Stollberger and P. Wach. Imaging of the active b1 field in vivo. *Magn Reson Med*, 35(2):246–251, 1996. ISSN 1522-2594. doi: 10.1002/mrm.1910350217. URL <http://dx.doi.org/10.1002/mrm.1910350217>.
- [96] C. H. Cunningham, J. M. Pauly, and K. S. Nayak. Saturated double-angle method for rapid b1+ mapping. *Magn Reson Med*, 55(6):1326–1333, 2006. ISSN 1522-2594. doi: 10.1002/mrm.20896. URL <http://dx.doi.org/10.1002/mrm.20896>.
- [97] F. Jiru and U. Klose. Fast 3d radiofrequency field mapping using echo-planar imaging. *Magn Reson Med*, 56(6):1375–1379, 2006. ISSN 1522-2594. doi: 10.1002/mrm.21083. URL <http://dx.doi.org/10.1002/mrm.21083>.
- [98] V. L. Yarnykh. Actual flip-angle imaging in the pulsed steady state: a method for rapid three-dimensional mapping of the transmitted radiofrequency field. *Magn Reson Med*, 57(1):192–200, 2007.
- [99] H. P. Fautz, M. Vogel, P. Gross, A. Kerr, and Y. Zhu. B1 mapping of coil arrays for parallel transmission. In *Proceedings of the 16th Annual Meeting of the ISMRM, Toronto, Canada*, page 1247, 2008.
- [100] L. I. Sacolick, F. Wiesinger, I. Hancu, and M. W. Vogel. B1 mapping by bloch-siegert shift. *Magn Reson Med*, 63(5):1315–1322, 2010. ISSN 1522-2594. doi: 10.1002/mrm.22357. URL <http://dx.doi.org/10.1002/mrm.22357>.
- [101] K. Nehrke, M. J. Versluis, A. Webb, and P. Boernert. Volumetric b1+ mapping of the brain at 7t using dream. *Magn Reson Med*, pages n/a–n/a, 2013. ISSN 1522-2594. doi: 10.1002/mrm.24667. URL <http://dx.doi.org/10.1002/mrm.24667>.
- [102] A. K. Funai, J. A. Fessler, D. Yeo, V. T. Olafsson, and D. C. Noll. Regularized field map estimation in mri. *IEEE T Med Imaging*, 27(10):1484–1494, 5 2008. ISSN 0278-0062.

- [103] S. Witoszynskyj, A. Rauscher, M. Barth, et al. Phase unwrapping of mr images using [phi] un-a fast and robust region growing algorithm. *Med Image Anal*, 13(2):257–268, 2009.
- [104] K. Zhou, M. Zaitsev, and S. Bao. Reliable two-dimensional phase unwrapping method using region growing and local linear estimation. *Magn Reson Med*, 62(4):1085–1090, 2009.
- [105] S. Robinson and J. Jovicich. B0 mapping with multi-channel rf coils at high field. *Magn Reson Med*, 2011.
- [106] J. Dagher, T. Reese, and A. Bilgin. High-resolution, large dynamic range field map estimation. *Magn Reson Med*, 71:105–117, 2014. ISSN 1522-2594. doi: 10.1002/mrm.24636. URL <http://dx.doi.org/10.1002/mrm.24636>.
- [107] N. Purchasing and S. Agency. Report 06006 3t mri systems. Technical Report 4, NHS Purchasing and Supply Agency, May 2007.
- [108] N. Purchasing and S. Agency. Report 06005 1.5t mri systems. Technical Report 7, NHS Purchasing and Supply Agency, May 2007.
- [109] J. F. Schenck. The role of magnetic susceptibility in magnetic resonance imaging: Mri magnetic compatibility of the first and second kinds. *Med Phys*, 23(6):815–850, 1996.
- [110] M. A. Bernstein, X. J. Zhou, J. A. Polzin, K. F. King, A. Ganin, N. J. Pelc, and G. H. Glover. Concomitant gradient terms in phase contrast mr: analysis and correction. *Magn Reson Med*, 39(2):300–308, 1998.
- [111] J. Van Vaals and A. Bergman. Optimization of eddy-current compensation. *J Magn Reson*, 90(1):52–70, 1990.
- [112] P. Jezzard, A. S. Barnett, and C. Pierpaoli. Characterization of and correction for eddy current artifacts in echo planar diffusion imaging. *Magn Reson Med*, 39(5):801–812, 1998.
- [113] H. Kim, S.-Y. Zho, and D.-H. Kim. Respiration-induced b0 fluctuation of spine. In *Proceedings of the 17th Annual Meeting of the ISMRM, Honolulu, USA*, page 1301, 2009.
- [114] D. Raj, A. W. Anderson, and J. C. Gore. Respiratory effects in human functional magnetic resonance imaging due to bulk susceptibility changes. *Phys Med Biol*, 46(12):3331, 2001.
- [115] A. M. El-Sharkawy, M. Schaer, P. A. Bottomley, and E. Atalar. Monitoring and correcting spatio-temporal variations of the mr scanner’s static magnetic field. *Magn Reson Mater Phy*, 19(5):223–236, 2006.
- [116] B. U. Foerster, D. Tomasi, and E. C. Caparelli. Magnetic field shift due to mechanical vibration in functional magnetic resonance imaging. *Magn Reson Med*, 54(5):1261–1267, 2005.
- [117] F. Farzaneh, S. J. Riederer, and N. J. Pelc. Analysis of t2 limitations and off-resonance effects on spatial resolution and artifacts in echo-planar imaging. *Magn Reson Med*, 14(1):123–139, 1990. ISSN 1522-2594. URL <http://dx.doi.org/10.1002/mrm.1910140112>.

- [118] M. A. Bernstein, J. Huston, and H. A. Ward. Imaging artifacts at 3.0 t. *J Magn Reson Imaging*, 24(4):735–746, 2006.
- [119] O. Dietrich, M. F. Reiser, and S. O. Schoenberg. Artifacts in 3-t mri: physical background and reduction strategies. *Eur J Radiol*, 65(1):29–35, 2008.
- [120] E. U. Saritas, C. H. Cunningham, J. H. Lee, E. T. Han, and D. G. Nishimura. Dwi of the spinal cord with reduced fov single-shot epi. *Magn Reson Med*, 60(2):468–473, 2008. ISSN 1522-2594. URL <http://dx.doi.org/10.1002/mrm.21640>.
- [121] B. M. Ellingson, J. Grinstead, J. Pfeuffer, T. Feiweier, L. Holly, and N. Salamon. Diffusion tensor imaging in human spondylotic myelopathy using a 2d rf excitation pulse combined with a reduced field-of-view single-shot echoplanar readout (zoomed epi). In *Proceedings of the 19th Annual Meeting of the ISMRM, Montreal, Canada*, page 4358, 2011.
- [122] G. Zaharchuk, E. U. Saritas, J. B. Andre, C. T. Chin, J. Rosenberg, T. J. Brosnan, A. Shankaranarayan, D. G. Nishimura, and N. J. Fischbein. Reduced field-of-view diffusion imaging of the human spinal cord: Comparison with conventional single-shot echo-planar imaging. *Am J Neuroradiol*, 32(5):813–820, 2011. ISSN 0195-6108.
- [123] D. Yoon. *Fast Joint design of RF and Gradient waveforms for MRI parallel excitation*. PhD thesis, The University of Michigan, 2012.
- [124] A. C. Zelinski, L. L. Wald, K. Setsompop, V. K. Goyal, and E. Adalsteinsson. Sparsity-enforced slice-selective mri rf excitation pulse design. *IEEE T Med Imaging*, 27(9):1213–1229, 2008.
- [125] W. Deng, B. Poser, and A. Stenger. Optimal control joint design of large-tip-angle rf pulses and gradient waveforms for parallel transmission. In *Proceedings of the 20th Annual Meeting of the ISMRM, Melbourne, Australia*, page 3463, 2012.
- [126] W. Feng and E. Haacke. Joint rf pulse and gradient design for 2d spatially selective excitation using optimal control and b-spline waveform model: initial experience. In *Proceedings of the 20th Annual Meeting of the ISMRM, Melbourne, Australia*, page 2210, 2012.
- [127] A. Greiser and M. von Kienlin. Efficient k-space sampling by density-weighted phase-encoding. *Magn Reson Med*, 50(6):1266–1275, 2003. ISSN 1522-2594. doi: 10.1002/mrm.10647. URL <http://dx.doi.org/10.1002/mrm.10647>.
- [128] B. Guérin, M. Gebhardt, E. Adalsteinsson, and L. Wald. Ptx pulse design with explicit hard constraints on local and global sar and maximum and average forward power. In *Proceedings of the 20th Annual Meeting of the ISMRM, Melbourne, Australia*, page 2215, 2012.
- [129] C. H. Meyer, J. M. Pauly, A. Macovskiand, and D. G. Nishimura. Simultaneous spatial and spectral selective excitation. *Magn Reson Med*, 15(2):287–304, 1990. ISSN 1522-2594. doi: 10.1002/mrm.1910150211. URL <http://dx.doi.org/10.1002/mrm.1910150211>.
- [130] D. M. Spielman, J. M. Pauly, and C. H. Meyer. Magnetic resonance fluoroscopy using spirals with variable sampling densities. *Magn Reson Med*, 34(3):388–394, 1995. ISSN 1522-2594. doi: 10.1002/mrm.1910340316. URL <http://dx.doi.org/10.1002/mrm.1910340316>.

- [131] V. Stenger, F. Boada, and D. Noll. Variable-density spiral 3d tailored rf pulses. *Magn Reson Med*, 50(5):1100–1106, 2003.
- [132] J. Lee, B. Hargreaves, B. Hu, and D. Nishimura. Fast 3d imaging using variable-density spiral trajectories with applications to limb perfusion. *Magn Reson Med*, 50(6):1276–1285, 2003.
- [133] C. Tsai and D. Nishimura. Reduced aliasing artifacts using variable-density k-space sampling trajectories. *Magn Reson Med*, 43(3):452–458, 2000. ISSN 1522-2594.
- [134] H. Tan and C. Meyer. Estimation of k-space trajectories in spiral mri. *Magn Reson Med*, 61(6):1396–1404, 2009.
- [135] J. Nistler, R. Kurth, R. Lazar, M. Vester, and W. Renz. A degenerate bandpass birdcage as antenna for a 3t wholebody transmit array. In *Proceedings of the 14th Annual Meeting of the ISMRM, Seattle, WA, USA*, page 2566, 2006.
- [136] P. Vernickel, P. Röschmann, C. Findeklee, K. Lüdeke, C. Leussler, J. Overweg, U. Katscher, I. Graesslin, and K. Schuenemann. Eight-channel transmit/receive body mri coil at 3t. *Magn Reson Med*, 58(2):381–389, 2007.
- [137] Y. Zhu, X. Chu, C. Cao, E. Fiveland, R. Giaquinto, T. Song, X. Yang, C. Zhang, J. Piel, and K. Park. Highly distributed rf transmission with a 32-channel parallel transmit system. In *Proceedings of the 17th Annual Meeting of the ISMRM, Honolulu, USA*, page 3020, 2009.
- [138] J. Vaughan, C. Snyder, L. DelaBarre, P. Bolan, J. Tian, L. Bolinger, G. Adriany, P. Andersen, J. Strupp, and K. Ugurbil. Whole-body imaging at 7t: Preliminary results. *Magn Reson Med*, 61(1):244–248, 2009.
- [139] S. Orzada, S. Maderwald, O. Kraff, I. Brote, M. Ladd, K. Solbach, P. Yazdanbakhsh, A. Bahr, H. Fautz, and A. Bitz. 16-channel tx/rx body coil for rf shimming with selected cp modes at 7t. In *Proceedings of the 18th Annual Meeting of the ISMRM, Stockholm, Sweden*, page 50, 2010.
- [140] G. Adriany, P.-F. Van de Moortele, J. Ritter, S. Moeller, E. J. Auerbach, C. Akgün, C. J. Snyder, T. Vaughan, and K. Ugurbil. A geometrically adjustable 16-channel transmit/receive transmission line array for improved rf efficiency and parallel imaging performance at 7 tesla. *Magn Reson Med*, 59(3):590–597, 2008. ISSN 1522-2594. doi: 10.1002/mrm.21488. URL <http://dx.doi.org/10.1002/mrm.21488>.
- [141] V. Stenger, F. Boada, and D. Noll. Three-dimensional tailored rf pulses for the reduction of susceptibility artifacts in  $t^*$  2-weighted functional mri. *Magn Reson Med*, 44(4):525–531, 2000.
- [142] S. Saekho, C. Yip, D. Noll, F. Boada, and V. Stenger. Fast-kz three-dimensional tailored radiofrequency pulse for reduced b1 inhomogeneity. *Magn Reson Med*, 55(4):719–724, 2006.
- [143] J. Frahm, K.-D. Merboldt, and W. Hänicke. Direct flash mr imaging of magnetic field inhomogeneities by gradient compensation. *Magn Reson Med*, 6(4):474–480, 1988.
- [144] R. Constable and D. Spencer. Composite image formation in z-shimmed functional mr imaging. *Magn Reson Med*, 42(1):110–117, 1999. ISSN 1522-2594. doi: 10.1002/(SICI)

- 1522-2594(199907)42:1<110::AID-MRM15>3.0.CO;2-3. URL [http://dx.doi.org/10.1002/\(SICI\)1522-2594\(199907\)42:1<110::AID-MRM15>3.0.CO;2-3](http://dx.doi.org/10.1002/(SICI)1522-2594(199907)42:1<110::AID-MRM15>3.0.CO;2-3).
- [145] G. H. Glover. 3d z-shim method for reduction of susceptibility effects in bold fmri. *Magn Reson Med*, 42(2):290–299, 1999. ISSN 1522-2594. doi: 10.1002/(SICI)1522-2594(199908)42:2<290::AID-MRM11>3.0.CO;2-N. URL [http://dx.doi.org/10.1002/\(SICI\)1522-2594\(199908\)42:2<290::AID-MRM11>3.0.CO;2-N](http://dx.doi.org/10.1002/(SICI)1522-2594(199908)42:2<290::AID-MRM11>3.0.CO;2-N).
- [146] A. W. Song. Single-shot epi with signal recovery from the susceptibility-induced losses. *Magn Reson Med*, 46(2):407–411, 2001. ISSN 1522-2594. doi: 10.1002/mrm.1205. URL <http://dx.doi.org/10.1002/mrm.1205>.
- [147] K. A. Heberlein and X. Hu. Simultaneous acquisition of gradient-echo and asymmetric spin-echo for single-shot z-shim: Z-saga. *Magn Reson Med*, 51(1):212–216, 2004. ISSN 1522-2594. doi: 10.1002/mrm.10680. URL <http://dx.doi.org/10.1002/mrm.10680>.
- [148] E. Haacke, J. Tkach, and T. Parrish. Reduction of  $t_2^*$  dephasing in gradient field-echo imaging. *Radiology*, 170(2):457–462, 1989.
- [149] N.-K. Chen, C. C. Dickey, S.-S. Yoo, C. R. Guttmann, and L. P. Panych. Selection of voxel size and slice orientation for fmri in the presence of susceptibility field gradients: application to imaging of the amygdala. *Neuroimage*, 19(3):817–825, 2003.
- [150] J.-J. Hsu and G. H. Glover. Mitigation of susceptibility-induced signal loss in neuroimaging using localized shim coils. *Magn Reson Med*, 53(2):243–248, 2005.
- [151] C. Juchem, T. W. Nixon, S. McIntyre, D. L. Rothman, and R. A. de Graaf. Magnetic field homogenization of the human prefrontal cortex with a set of localized electrical coils. *Magn Reson Med*, 63(1):171–180, 2010.
- [152] J. L. Wilson and P. Jezard. Utilization of an intra-oral diamagnetic passive shim in functional mri of the inferior frontal cortex. *Magn Reson Med*, 50(5):1089–1094, 2003.
- [153] R. Cusack, B. Russell, S. M. Cox, C. De Panfilis, C. Schwarzbauer, and R. Ansorge. An evaluation of the use of passive shimming to improve frontal sensitivity in fmri. *Neuroimage*, 24(1):82–91, 2005.
- [154] S. Yang, H. Kim, M.-O. Ghim, B.-U. Lee, and D.-H. Kim. Local in vivo shimming using adaptive passive shim positioning. *Magn Reson Imaging*, 29(3):401–407, 2011.
- [155] C. Yang, W. Deng, and V. Stenger. Simple analytical dual-band spectral-spatial rf pulses for b1+ and susceptibility artifact reduction in gradient echo mri. *Magn Reson Med*, 65(2):370–376, 2011.
- [156] R. J. Anderson, B. A. Poser, and V. A. Stenger. Simultaneous multislice spectral-spatial excitations for reduced signal loss susceptibility artifact in bold functional mri. *Magn Reson Med*, pages n/a–n/a, 2013. ISSN 1522-2594. doi: 10.1002/mrm.25050. URL <http://dx.doi.org/10.1002/mrm.25050>.
- [157] C. Yang, B. A. Poser, W. Deng, and V. A. Stenger. Spectral decomposition of susceptibility artifacts for spectral-spatial radiofrequency pulse design. *Magn Reson Med*, 68(6):1905–1910, 2012. ISSN 1522-2594. doi: 10.1002/mrm.24208. URL <http://dx.doi.org/10.1002/mrm.24208>.
- [158] K. J. Friston, A. P. Holmes, K. J. Worsley, J.-P. Poline, C. D. Frith, and R. S. J. Frackowiak. Statistical parametric maps in functional imaging: A general linear

- approach. *Hum Brain Mapp*, 2(4):189–210, 1994. ISSN 1097-0193. doi: 10.1002/hbm.460020402. URL <http://dx.doi.org/10.1002/hbm.460020402>.
- [159] J. A. de Zwart, P. van Gelderen, X. Golay, V. N. Ikonomidou, and J. H. Duyn. Accelerated parallel imaging for functional imaging of the human brain. *NMR Biomed*, 19(3):342–351, 2006.
  - [160] C. Triantafyllou, J. R. Polimeni, and L. L. Wald. Physiological noise and signal-to-noise ratio in fmri with multi-channel array coils. *Neuroimage*, 55(2):597–606, 2011.
  - [161] T. W. J. Scheenen, S. W. T. P. J. Heijmink, S. A. Roell, C. A. Hulsbergen-Van de Kaa, B. C. Knipscheer, J. A. Witjes, J. O. Barentsz, and A. Heerschap. Three-dimensional proton mr spectroscopy of human prostate at 3 t without endorectal coil: Feasibility1. *Radiology*, 245(2):507–516, 2007. doi: 10.1148/radiol.2451061444. URL <http://radiology.rsna.org/content/245/2/507.abstract>.
  - [162] M. Martinez-Ramon, A. Gallardo-Antolin, J. Cid-Sueiro, G. L. Heileman, K.-T. Yung, W. Zheng, C. Zhao, and S. Posse. Automatic placement of outer volume suppression slices in mr spectroscopic imaging of the human brain. *Magn Reson Med*, 63(3):592–600, 2010. ISSN 1522-2594. doi: 10.1002/mrm.22275. URL <http://dx.doi.org/10.1002/mrm.22275>.
  - [163] B. Gagoski, K. Makhoul, D. Ritter, K. Setsompop, J. Pfeuffer, H. Bhat, P. Hoecht, M. Hamm, U. Fontius, L. Kini, J. Lee, L. Wald, and E. Adalsteinsson. Flexibly shaped saturation band excitation using 7t parallel transmit system. In *Proceedings of the 19th Annual Meeting of the ISMRM, Montreal, Canada*, page 4437, 2011.
  - [164] T. Mareci and H. Brooker. Essential considerations for spectral localization using indirect gradient encoding of spatial information. *J. Magn. Reson.*, 92(2):229–246, 1991.
  - [165] T. Zhao, Y. Qian, Y.-K. Hue, T. Ibrahim, and F. Boada. An improved analytical solution for variable density spiral design. In *Proceedings of the 16th Annual Meeting of the ISMRM, Toronto, Canada*, page 1342, 2008.
  - [166] R. Gumbrecht, T. Benner, U. Fontius, H. Adolf, A. Bitz, and H. P. Fautz. Safe online local sar calculation for transmit arrays using asynchron data processing. In *Proceedings of the 21th Annual Meeting of the ISMRM, Salt Lake City, USA*, page 4423, 2013.
  - [167] R. Gumbrecht, U. Fontius, H. Adolf, T. Benner, E. Adalsteinsson, L. L. Wald, and H. P. Fautz. Online local sar supervision for transmit arrays at 7t. In *Proceedings of the 21th Annual Meeting of the ISMRM, Salt Lake City, USA*, page 4420, 2013.
  - [168] R. Schneider, B. Guerin, M. Hamm, J. Haueisen, E. Adalsteinsson, L. Wald, and J. Pfeuffer. Spatial selective excitation performance of parallel transmission using a 3x8 z-stacked rf coil array at 3t. In *Proceedings of the 21st Annual Meeting of the ISMRM, Salt Lake City, USA*, page 4252, 2013.
  - [169] B. Guerin, M. Gebhardt, P. Serano, E. Adalsteinsson, M. Hamm, J. Pfeuffer, J. Nistler, and L. L. Wald. Comparison of simulated parallel transmit body arrays at 3 t using excitation uniformity, global sar, local sar, and power efficiency metrics. *Magn Reson Med*, pages n/a–n/a, 2014. ISSN 1522-2594. doi: 10.1002/mrm.25243. URL <http://dx.doi.org/10.1002/mrm.25243>.





## Erklärung

Ich versichere, dass ich die vorliegende Arbeit ohne unzulässige Hilfe Dritter und ohne Benutzung anderer als der angegebenen Hilfsmittel angefertigt habe. Die aus anderen Quellen direkt oder indirekt übernommenen Daten und Konzepte sind unter Angabe der Quelle gekennzeichnet.

Bei der Auswahl und Auswertung folgenden Materials haben mir die nachstehend aufgeführten Personen in der jeweils beschriebenen Weise unentgeltlich geholfen:

1. *Unterstützung bei der numerischen Implementierung von Methoden zur SAR-Berechnung und unentgeltliche Bereitstellung der Simulationsdaten der elektrischen und magnetischen Feldverteilungen im Abschnitt 5.1.*

Dipl.-Phys. Matthias Gebhardt  
MR Physik  
Siemens Healthcare AG, Erlangen, Deutschland

2. *Unterstützung bei der Interpretation von Ergebnissen in der gesamten Arbeit.*

Dr. rer. nat. Josef Pfeuffer  
MR Neuro-Applikationsentwicklung  
Siemens Healthcare AG, Erlangen, Deutschland

Prof. Dr.-Ing. habil. Jens Haueisen  
Institut für Biomedizinische Technik und Informatik  
Technische Universität Ilmenau, Ilmenau, Deutschland

Weitere Personen waren an der inhaltlich-materiellen Erstellung der vorliegenden Arbeit nicht beteiligt. Insbesondere habe ich hierfür nicht die entgeltliche Hilfe von Vermittlungs- bzw. Beratungsdiensten (Promotionsberater oder anderer Personen) in Anspruch genommen. Niemand hat von mir unmittelbar oder mittelbar geldwerte Leistungen für Arbeiten erhalten, die im Zusammenhang mit dem Inhalt der vorgelegten Dissertation stehen.

Die Arbeit wurde bisher weder im In- noch im Ausland in gleicher oder ähnlicher Form einer Prüfungsbehörde vorgelegt.

Ich bin darauf hingewiesen worden, dass die Unrichtigkeit der vorstehenden Erklärung als Täuschungsversuch bewertet wird und gemäß §7 Abs. 10 der Promotionsordnung den Abbruch des Promotionsverfahrens zur Folge hat.

Erlangen, den 24.09.2014

